AIRTRAC v2.0: a Lagrangian aerosol tagging submodel for the analysis of aviation SO₄ transport patterns

Jin Maruhashi[1,a], Mattia Righi[2], Monica Sharma[1,2], Johannes Hendricks[2], Patrick Jöckel[2], Volker Grewe[1,2], Irene C. Dedoussi[1,3]

5   [1]Delft University of Technology, Faculty of Aerospace Engineering, Operations and Environment, Delft, The Netherlands
[a]now at: Department of Civil and Environmental Engineering, Imperial College London, London, United Kingdom
[2]Deutsches Zentrum für Luft- und Raumfahrt (DLR), Institut für Physik der Atmosphäre, Oberpfaffenhofen, Germany
[3]Department of Engineering, University of Cambridge, Cambridge, United Kingdom

Correspondence to: Irene C. Dedoussi (icd23@cam.ac.uk)

10   **Abstract.** Aviation-induced aerosols, particularly composed of sulfate (SO_4), can interact with liquid clouds by enhancing their reflectivity and lifetime, thereby exerting a cooling effect. The magnitude of these interactions, however, remains highly uncertain and may even offset the combined warming from aviation's other climate forcers depending on spatiotemporal factors such as emission altitude and season. Here, we introduce AIRTRAC v2.0, the latest advancement of the Lagrangian tagging submodel within the Modular Earth Submodel System (MESSy), and the first submodel to provide aviation-specific

15   sulfate tagging in this framework. AIRTRAC contributes to lowering uncertainty by tracking global contributions of aviation-emitted sulfur dioxide (SO_2) and sulfuric acid (H_2SO_4) to SO_4 formation. Using a sulfur-species tagging approach for SO_2, H_2SO_4 and SO_4, it enables the characterization of transport patterns and highlights atmospheric regions with enhanced potential for aerosol–cloud interactions. In contrast to some of the existing sulfate tagging models, AIRTRAC considers a full range of microphysical processes along trajectories. To investigate sulfate transport from aviation, two global simulations were

20   performed for January–March and July–September 2015, using pulse emissions of SO_2 and H_2SO_4 distributed across a cruise altitude of 240 hPa (~10.6 km) based on the aviation SO_2 inventory of the Coupled Model Intercomparison Project Phase 6 (CMIP6). Comparisons of AIRTRAC-derived SO_4 distributions with perturbation-based simulations under analogous conditions show reasonable agreement. Using AIRTRAC v2.0, we estimate median SO_2 and SO_4 lifetimes of 22 d and 2.1 months, respectively, in northern winter, and 14 d and 2.2 months in summer, consistent with volcanic eruption modeling and

25   observational benchmarks involving high-altitude SO_2 injection. The median SO_4 production efficiency during summer was found to be statistically significantly larger by 144% compared to winter, due to a more efficient oxidation of SO_2. Large-scale circulation patterns may contribute to enhancing SO_4 lifetimes, especially when injected in the Tropics, where emissions could ascend into the stratosphere, past 100 hPa (~16 km). AIRTRAC v2.0 currently excludes SO_2 oxidation from aviation nitrogen oxides (NO_x) and does not tag other species such as black carbon. Owing to its flexible design, however, the approach can be

30   readily extended to additional aerosols. Overall, AIRTRAC v2.0 offers the novel capability to track the atmospheric transport of aviation-emitted SO_2, H_2SO_4 and SO_4, providing critical insights into one of aviation's most uncertain climate impacts.

1 Introduction

Recent estimates suggest that in 2018, aviation accounted for approximately 2% of the total anthropogenic radiative forcing (RF) from carbon dioxide (CO_2; Klower et al., 2021) emissions and about 3.5% or ~150 mWm^{-2} (70-229 mWm^{-2} for a 90% confidence interval) of all anthropogenic warming when additional non-CO_2 effects (Lee et al., 2021) are also contemplated. The latter estimate, however, carries significant uncertainties due to the intricate interactions and trade-offs between various climate forcers, including nitrogen oxides (NO_x), water vapor (H_2O) and persistent contrails. Additionally, this estimate includes warming and cooling from direct absorption and scattering effects of soot (black carbon (BC) and organic carbon (OC)) and sulfate (SO_4) aerosols, respectively. However, it does not consider any indirect RF contributions from their interactions with clouds. Furthermore, Lee et al. (2021) do not include the potential influence of aviation NO_x on SO_4 and nitrate (NO_3) aerosol formation, both of which may contribute with substantial cooling (Terrenoire et al., 2022).

Notably, the indirect cooling effect of SO_4 aerosols alone could reduce aviation's net radiative forcing considerably. Some estimates indicate that the absolute value of this cooling effect may range from 17 to 160 mWm^{-2} (Gettelman and Chen, 2013; Kapadia et al., 2016; Fig. 5 in Lee et al., 2021), a magnitude comparable to aviation's largest global mean warming contribution from aircraft-induced contrail cirrus—estimated at 111 [33, 189] mW m^{-2} for 2018 (Lee et al., 2021) and 62 mW m^{-2} for 2019 (Teoh et al., 2019). Another study broadens this analysis by including both direct and indirect aerosol-induced SO_4 forcings, suggesting that their combined cooling effect could again surpass the warming from aviation-induced contrail cirrus, although indirect aerosol effects are typically more dominant (Righi et al., 2013). These combined aerosol forcings raise the possibility of a near-zero or even net negative radiative forcing (RF) from kerosene-powered aircraft. However, this outcome remains highly uncertain due to inherent complexities in quantifying indirect aerosol effects. More robust estimates from independent modeling efforts, supported by a better understanding of critical processes such as pollutant transport patterns, are essential. Without clearer insights into these climate forcers, the effective development and comprehensive evaluation of mitigation strategies will remain challenging.

Aerosols are collections of solid or liquid particles suspended in the atmosphere, with sizes ranging from 0.001 µm to 100 µm (Petzold and Kärcher, 2012; Brasseur and Jacob, 2017). Among the aerosols resulting from aviation are soot and sulfate. Soot is produced from the incomplete combustion of aromatic compounds in the jet fuel (Kärcher et al., 2007; Lee et al., 2021), while SO_4 forms indirectly from the emissions of sulfur dioxide (SO_2) and sulfuric acid (H_2SO_4). Experimental studies indicate that aircraft convert approximately 97% of the sulfur content in fuel into SO_2, with SO_2 emissions nearly directly proportional to fuel sulfur levels. The remaining 2-3% is emitted as H_2SO_4 (Petzold et al., 2005; Jurkat et al., 2011; Owen et al., 2022). The gaseous conversion of SO_2 to H_2SO_4 involves a series of reactions (R1 – R3), where the oxidation of SO_2 by hydroxyl (OH) radicals ultimately results in the production of H_2SO_4 (Mikkonen et al., 2011):

$$SO_2 + OH \rightarrow HSO_3 \tag{R1}$$

$$HSO_3 + O_2 \rightarrow SO_3 + HO_2 \qquad\qquad (R2)$$

$$SO_3 + 2H_2O \rightarrow H_2SO_4 + H_2O. \qquad\qquad (R3)$$

65   The formation of SO_4 aerosols can proceed through multiple mechanisms. One pathway involves the condensation of H_2SO_4 vapor onto pre-existing particles, followed by particle growth through coagulation and further condensation (Whitby and McMurry, 1997; Laaksonen et al., 2000; Aquila et al., 2011). Sulfate aerosols may also form via the binary homogeneous nucleation between H_2SO_4 and H_2O, a process influenced by factors such as atmospheric relative humidity and temperature (Vehkamäki et al., 2002; Kaiser et al., 2014). Additionally, SO_4 production can occur through the reaction of H_2SO_4 with

70   gaseous ammonia (NH_3), resulting in the formation of ammonium sulfate ((NH_4)$_2SO_4$) or ammonium bisulfate (NH_4HSO_4), which subsequently dissociate to yield SO_4, ammonium (NH_4) and hydrogen (Khoder, 2002). An alternative pathway involves the liquid-phase oxidation of sulfurous acid (H_2SO_3) by hydrogen peroxide (H_2O_2) and ozone (O_3; Martin and Damschen, 1981; Yang et al., 2017). Figure 1 illustrates the primary reaction mechanisms leading to SO_4 formation via SO_2 and H_2SO_4.
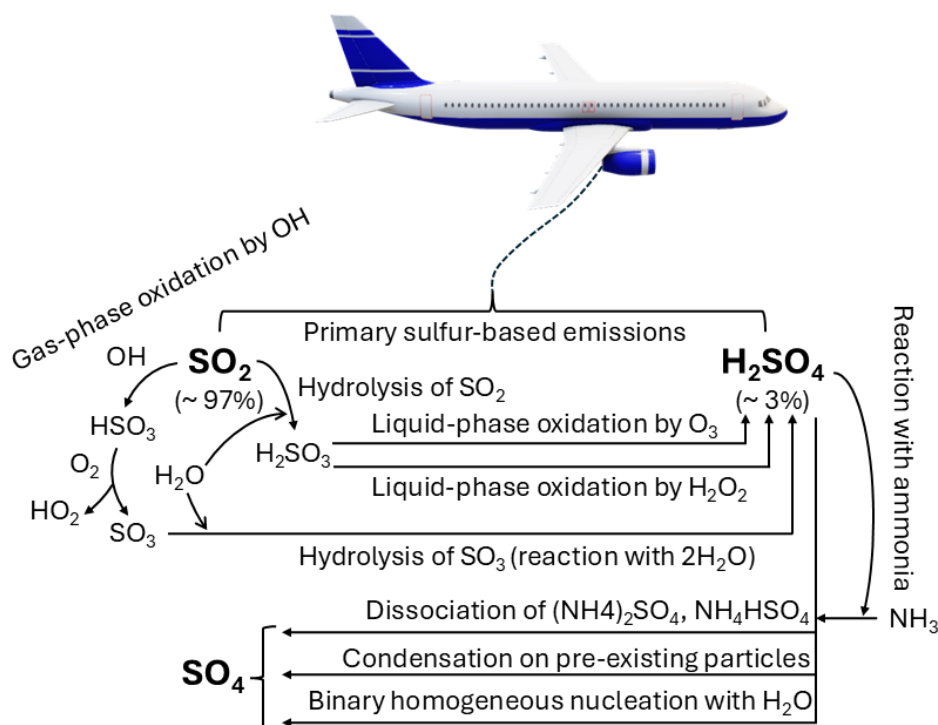

Figure 1 – Production mechanisms of sulfate (SO_4) from aviation emissions of sulfur dioxide (SO_2) and sulfuric acid (H_2SO_4).

75   Aerosol direct effects alter Earth's energy balance by scattering and absorbing solar and thermal infrared radiation depending on a particle's optical properties. Sulfate aerosols primarily scatter incoming shortwave solar radiation, resulting in a cooling

effect, whereas soot particles predominantly absorb this radiation, leading to a warming effect (Haywood and Shine, 1995; Kirkevåg et al., 1999; Lee et al., 2021). In addition to these direct effects, aerosols also have indirect effects through their influence on cloud properties, such as albedo and lifetime. These effects are known as the Twomey and Albrecht effects, respectively. As aerosols can often act as cloud condensation nuclei (CCN), an increase in their number can also increase the cloud droplet number concentration (CDNC) within liquid-phase clouds. Assuming the liquid water content within a cloud is constant, adding more CCNs will lead to more numerous cloud droplets, but with smaller radii. Given that cloud droplets mainly scatter solar radiation, an increase in CCNs therefore results in an overall enhancement in a cloud's reflective ability or albedo, an effect referred to as the Twomey effect (Twomey, 1977; Lohmann and Feichter, 1997; Sausen et al., 2012). Another consequence of having additional, smaller cloud droplets is the decrease of a cloud's precipitating ability, which prolongs its lifetime and therefore also the amount of solar radiation that it can reflect back into space (Albrecht, 1989; Lohmann and Feichter, 2005).

The considerably larger uncertainties in estimating indirect SO_4 effects compared to direct effects stem, among others, from the challenge in accurately describing the complex cloud microphysical processes occurring in the sub-grid scale that often need to be parameterized in global climate models (Lohmann and Feichter, 1997; Lohmann and Feichter, 2005). Additionally, limited understanding of aerosol transport pathways, including vertical transport and large-scale horizontal advection, as well as of the variations in microphysical and removal processes along these paths contribute to this uncertainty (Barrie et al., 2001; Weinzierl et al., 2017). These transport dynamics are particularly relevant in the context of aviation emissions, which occur at higher altitudes than ground-level sources such as shipping, as the emission location significantly influences both the production efficiency and atmospheric lifetime of pollutants, as has been shown for NO_x emissions by Maruhashi et al. (2022). Model intercomparison studies, such as the Comparison of Large Scale Sulfate Aerosol Models (COSAM), have demonstrated that the conversion of SO_2 to SO_4 is challenging to predict, resulting in a spread of model results of $10-50\%$ and discrepancies of up to a factor of two compared to observational data from aircraft campaigns. This spread lead to uncertainties not only in the vertical distribution profiles of SO_4, but also in the resulting number of CCN produced, both of which directly influence estimates of SO_4 indirect forcing (Barrie et al., 2001; Penner et al., 2001). Such knowledge gaps therefore prevent a comprehensive assessment of aviation's net climate impact (Lee et al., 2021).

Haywood and Boucher (2000) provide estimates for anthropogenic SO_4 direct and indirect effects, with the latter spanning from -30 mWm^{-2} to -178 mWm^{-2}. However, few studies have isolated these effects for aviation. Righi et al. (2013) assessed both, direct and indirect SO_4 effects, across the transport sector (land, shipping and aviation) and estimated aviation's contribution to lie within the range -69.5 mWm^{-2} to 2.4 mWm^{-2}, noting that larger SO_4 particle sizes led to weaker cooling. Similarly, Gettelman and Chen (2013) found that smaller emitted particles (8 nm diameter) produced the strongest cooling effect at -160 mW·m^{-2}. Most existing studies assume instantaneous dilution and neglect plume-scale processes, likely overestimating particle number concentrations by at least 15% (Sharma et al., 2025).

110 Kapadia et al. (2016) demonstrated a linear relationship between aircraft fuel sulfur content (FSC) and the magnitude of the Twomey effect, reporting RF values from -82.1 mWm^{-2} (6000 ppm FSC) to -16.6 mWm^{-2} (sulfur-free fuel). They also highlighted the policy trade-off between reduced cooling and improved air quality from low-sulfur fuels (see also Fuglestvedt et al., 2009).

Matthes et al. (2021) extended this analysis by examining the sensitivity of aviation-induced aerosol RF to cruise altitude, estimating a forcing of -15.1 mW·m^{-2} at a reference altitude using the same simulation setup as Righi et al. (2013), but with

115 the REACT4C emissions inventory (Søvde et al., 2014) for 2006. They found that the cooling effect increased at lower altitudes. More recently, Righi et al. (2023) updated these estimates using the CMIP6 emissions inventory (Feng et al., 2020) for 2015 and calculated aviation's combined SO_4 direct and indirect effect to be -64 mWm^{-2}. Under the shared socioeconomic pathway (SSP) SSP2-4.5 scenario (Fricko et al., 2017) for 2050, this value increased to -126 mWm^{-2}. Table 1 summarizes these past findings on aviation-related SO_4 aerosol effects.

120 Table 1: An overview of studies that have estimated RF from aviation-induced SO_4 direct and indirect effects. The * indicates the amount of emitted SO_2 as referred in the comprehensive study of Lee et al. (2021). **Emitted SO_2 in Tg estimated assuming an emission index of 0.8 g/kg of fuel (Lee et al., 2010). FSC denotes fuel sulfur content.

Study	Emission details	Calculation method	RF estimate [mWm^{-2}]
Righi et al., 2013	CMIP5 emissions (Lamarque et al., (2010)) for the year 2000. Emission varies from 0.0008 to 0.1216 Tg(SO_2)*.	Perturbation approach	Includes direct and indirect effects: RF = [-69.5, 2.4]
Gettelman and Chen, 2013	Emission of 0.2257 Tg(SO_2)* for the year 2006.	Perturbation approach	Sensitivity of indirect effect to SO_4 particle diameters: RF (8 nm) = -160 RF (14 nm) = -44 RF (21 nm) = -22
Kapadia et al., 2016	Range of emission cases for the year 2000 (FSC levels): Large = 2.358 Tg(SO_2) Normal = 0.236 Tg(SO_2) Low = 0.006 Tg(SO_2) No sulfur = 0 Tg(SO_2).	Perturbation approach	Only Twomey effect: $RF_{Large\ FSC}$ = -82.1 $RF_{Normal\ FSC}$ = -23.6 $RF_{Low\ FSC}$ = -16.8 $RF_{No\ FSC}$ = -16.6
Matthes et al., 2021	Simulation setup identical to Righi et al. (2013), but with the REACT4C emissions inventory for 2006 (Søvde et al., 2014). Emission ≈0.284 Tg(SO_2)**.	Perturbation approach	Includes direct and indirect effects: -15.1 (reference case of aircraft flying at their optimal altitude)
Righi et al., 2023	CMIP6 emissions (Feng et al., 2020) for 2015 and other SSP scenarios (e.g. SSP2-4.5).	Perturbation approach	Includes direct and indirect effects: RF_{2015} = -64 $RF_{SSP2-4.5\ 2050}$ = -126

Within the context of climate-chemistry modeling, aviation's climate impacts are generally estimated using one of two main approaches: source apportionment or perturbation. The former is also referred to as tagging, as it involves labelling chemical

125　species and reactions of interest and accompanying their fate throughout a simulation (Wang et al., 2009). It is normally applied to quantify the contribution of a sector to the total concentration of a pollutant. The perturbation method, on the other hand, involves evaluating the marginal impact of a change in emissions typically by subtracting two simulations: one with all emissions and another with changed emissions (Blanchard, 1999; Hoor et al., 2009; Clappier et al., 2017). Based on Table 1 and to the authors' best knowledge, aviation-specific indirect effects of SO_4 have thus far only been estimated using the

130　perturbation method. While useful, it is insufficient on its own for formulating robust mitigation policies. Tagging techniques enable precise attribution of emissions to specific sectors, helping to identify those with the highest mitigation potential. The perturbation method can then complement this by quantifying the effects of targeted reduction measures (Mertens et al., 2018). Righi et al. (2023) highlight the difficulty of applying a tagging method for aerosols due to the challenges of tracking their complex liquid- and gas-phase transformations and interactions with clouds.

135　Only a handful of Eulerian and Lagrangian sulfate tagging schemes exist. Eulerian model studies include those by Yang et al. (2017), who used the Community Atmosphere Model (CAM) within the Community Earth System Model (CESM) framework to quantify global SO_4 contributions from 16 sources and assess both direct and indirect radiative forcing effects, between 2010 – 2014. Other Eulerian approaches target regional impacts in China. For example, Wu et al. (2017) utilized an online tagging method within the Nested Air Quality Prediction Model System (NAQPMS) to reveal that SO_4 levels in Shanghai

140　were significantly influenced by non-local sources. Similarly, Itahashi et al. (2017), employing the Particulate Source Apportionment Technology (PSAT) algorithm (Wagstrom et al., 2008) with the sixth version of the Comprehensive Air quality Model (CAMx), assessed SO_4 contributions from 31 Chinese provinces and found that emissions from the central and northern regions notably affected sulfate levels in Taiwan, Korea and Japan. Lagrangian approaches include the study by Riccio et al. (2014), which used the Hybrid Single-Particle Lagrangian Integrated Trajectory (HYSPLIT) model to show that $PM_{2.5}$ levels

145　in Naples were substantially impacted by emissions from other parts of Europe and dust transport from the Sahara. Despite their methodological differences, these studies highlight the influence of cross-territorial emissions on regional SO_4 levels as a result of long-range transport. There are also Lagrangian particle dispersion models like FLEXible PARTicle (FLEXPART) and LAGRANTO that have been applied to study sulfate transport and lifetime of SO_2 from volcanic emissions (Sun et al., 2023; Sun et al., 2024; Toohey et al., 2025). These studies are somewhat comparable to the scenario of aircraft cruise emissions,

150　as both emit SO_2 above sea level and may inject SO_4 into the upper troposphere and lower stratosphere. None of these studies, however, have characterized the aviation-specific global transport patterns of SO_4 originating from the primary emissions of SO_2 and H_2SO_4 introduced at subsonic cruise altitudes.

　　Here, we address this fundamental knowledge gap by introducing the first Lagrangian aerosol tagging submodel for SO_4 within the fifth-generation European Centre for Medium-Range Weather Forecasts – Hamburg (ECHAM)/Modular Earth Submodel

155　System (MESSy) Atmospheric Chemistry (EMAC) modeling framework, enabling a detailed, parcel-by-parcel analysis of aviation SO_4 transport patterns. AIRTRAC v2.0 represents an important advancement, extending the original Lagrangian

AIRTRAC submodel (Supplement of Grewe et al., 2014a) by incorporating aerosol processes along air parcel trajectories – capabilities unique to this updated version. Specifically, aerosol mixing ratios are computed using the extensively validated third-generation Modal Aerosol Dynamics model for Europe (MADE3; Kaiser et al., 2014; Kaiser et al., 2019) submodel, while aviation-specific contributions are quantified by AIRTRAC. Previously, AIRTRAC was limited to the study of gas-phase emissions such as NO_x and H_2O (Frömming et al., 2021; Maruhashi et al., 2022), primarily aimed at quantifying their contributions to atmospheric concentrations of reactive nitrogen species (NO_y), including nitric acid (HNO_3), O_3, the hydroperoxyl radical (HO_2), hydroxide (OH) and methane (CH_4). This Lagrangian approach offers a substantial computational advantage over more resource-intensive Eulerian simulations by enabling the simultaneous analysis of multiple emission scenarios (Maruhashi et al., 2024), while also providing clearer insight into the transport patterns of emitted pollutants (Frömming et al., 2021; Maruhashi et al., 2022).

In the present assessment, we focus on the SO_4 aerosol as it has been shown to be a highly efficient CCN for liquid clouds. In contrast, soot is hydrophobic and therefore generally becomes a CCN only when mixed internally with other more hygroscopic aerosols like SO_4 (Kristjánsson, 2002; Lee et al., 2021). This study has three primary objectives. First, it describes a novel Lagrangian aerosol-tagging submodel and the assumptions underlying its formulation. Second, the study demonstrates the usefulness of the new AIRTRAC v2.0 submodel in improving our understanding of the transport patterns of aviation-induced SO_2 and H_2SO_4 emissions, particularly in identifying where these lead to the largest SO_4 enhancements—especially over regions with abundant low-level liquid clouds. The analysis considers 28 globally distributed emission points along major present-day flight routes at a typical cruise altitude (240 hPa ≈ 10.6 km) for both winter and summer seasons. Using ESA satellite data to locate regions of significant liquid cloud cover, AIRTRAC v2.0 is applied to trace trajectories most likely to interact with these clouds, highlighting its potential to inform assessments of aerosol-cloud interactions. Third, the study compares the spatial distributions of SO_4 generated by this tagging approach against those derived using a perturbation method using a similar simulation setup. As part of our evaluation, we compare our SO_2 and SO_4 lifetime estimates with those reported in other Lagrangian modeling and observational studies of volcanic eruptions. The paper is structured into six sections: Section 1 provides an introduction; Section 2 describes the overall EMAC modeling setup, including the MADE3 aerosol submodel with which AIRTRAC v2.0 has been coupled within the MESSy framework, and presents the general formulation of the SO_4 mass transport equations. Section 3 outlines the AIRTRAC v2.0 infrastructure and details the tagging formulation of the SO_4 transport equations. Section 4 presents results of simulations from AIRTRAC v2.0 and integrates satellite cloud data to illustrate the submodel's capability to predict interactions with low-level liquid clouds. Section 5 compares AIRTRAC's output with the results of a perturbation approach and with prior studies. Finally, Section 6 summarizes key findings, considers limitations of the AIRTRAC v2.0 submodel and offers directions for future research.

2 Modeling framework

This section summarizes the most relevant characteristics of EMAC along with the main submodels applied in our base modeling setup (Section 2.1). Section 2.2 describes the SO_2 and H_2SO_4 pulse emission locations and inventory used in our simulations. In Section 2.3, the submodel responsible for computing aerosol microphysics (MADE3), the most relevant aerosol microphysical processes and the general formulation of the SO_4 mass transport equations are presented. The submodels governing the removal processes and transport of aerosol species are then presented in Section 2.4.

2.1 The EMAC model setup

Chemistry-climate simulations in this assessment are performed with the EMAC model. It is a flexible, global model that simulates a plethora of atmospheric processes along with interactions between land, ocean and anthropogenic activity by means of a coupling interface called MESSy (Jöckel et al., 2010) that can connect more than 100 different submodels to ECHAM5, EMAC's base general circulation model (Roeckner et al., 2006). Apart from AIRTRAC, which is responsible for calculating the contribution of aviation-related pollutants along air parcel trajectories and MADE3, which calculates aerosol dynamics and microphysical processes, there are other submodels that are also relevant in our modeling setup. Some of these are described in Section 2.4. The full list of applied submodels is included in Table A1 in Appendix A.

Simulations are performed with version 5.3.02 of the base model ECHAM5 and with version 2.55.2 of the MESSy integrated framework. The EMAC model resolution is T42L41DLR, which corresponds to a quadratic Gaussian grid of size ~2.8° × 2.8° (with 128 longitude and 64 latitude grid cells) with 41 discrete, vertical hybrid sigma-pressure levels ranging from the surface to the uppermost layer of the atmosphere centered at 5 hPa. For comparability purposes with Righi et al. (2023), our model output is characterized by a temporal resolution of 11 h with a model calculation time-step length of 15 min. The meteorology (the temperature, the wind divergence, the vorticity and the logarithm of the sea-level pressure) in our simulations has been nudged by Newtonian relaxation towards ERA-Interim reanalysis data (Dee et al., 2011) for the simulated year. Sea surface temperature and sea ice concentration have been prescribed from the ERA-Interim reanalysis data as well. Two simulations (starting on January 1, 2015 for Northern winter and on July 1, 2015 for Northern summer) were performed to accompany the chemical transport of aviation SO_2 and H_2SO_4 and their conversion into SO_4 for three months across 28 emission points (see Fig. 2) at an altitude of 240 hPa. To ensure background meteorological conditions are in quasi-equilibrium, each simulation was preceded by a four-month spin-up period. Each emission point releases varying amounts of SO_2 and H_2SO_4 in the form of 15-minute pulse emissions. These are initially advected by 50 air parcels originating from the grid box of each emission point, consistent with the recommendation of Grewe et al. (2014a). These 50 air parcels are pseudo-randomly initialized around the coordinates of an emission point according to a uniform distribution between 0 and 1. A simplified background chemistry mechanism is applied with the MECCA submodel (Sander et al., 2019) for the troposphere that involves the most relevant gaseous species like NO_x, HO_x, CH_4 and O_3. Aqueous-phase chemistry is handled by the SCAV submodel (Tost et al., 2006). These chemistry mechanisms are solved automatically by the Kinetic Pre-Processor (KPP) software using Fortran 90 code

(Sander et al., 2005). The overall Lagrangian setup is similar to the one used by Maruhashi et al. (2022) and Maruhashi et al.
220 (2024), while the applied aerosol chemistry and scavenging mechanisms are the same as those applied by Righi et al. (2023).

2.2 SO_2 and H_2SO_4 emission points

The 28 emission locations at which SO_2 and H_2SO_4 pulses are introduced (Fig. 2) are selected to reflect a realistic modern-day spatial distribution of aviation emissions. This distribution was determined according to the 2015 CMIP6 aviation emissions inventory that includes the correction for the latitudinal bias found by Thor et al. (2023). The exact coordinates of the 28 points
225 in Fig. 2 are included in Table B1 from Appendix B. Each coordinate has three dimensions – latitude, longitude and altitude – which are found by identifying the locations at which the aviation SO_2 mass flux (kg m^{-3} s^{-1}) is maximum. The emission altitude is determined by establishing the pressure level at which the zonally averaged aviation SO_2 mass flux is the largest (see Fig. B1 in Appendix B): ~240 hPa. We have developed an accompanying tool in Python (see EP_selector in Appendix B and the data repository of Maruhashi et al. (2025a) for the complete code) that approximates continuous emissions as a set of
230 distributed pulse emissions by automatically identifying the top 28 points whose grid cells have the largest SO_2 mass flux contributions (defined as a grid cell's area-weighted mean mass flux, see Eq. B1) within a user-defined mesh. The total mass of emitted SO_2 and H_2SO_4 across these points was scaled to yield the approximate global aviation SO_2 produced in a day from aviation in 2015 (Righi et al., 2023). The emitted amount of H_2SO_4 at any given emission point is determined by assuming that it constitutes 2% of the total SO_2 mass emitted by aviation, which is consistent with measurements of aircraft exhaust
235 plumes at cruise altitudes (Jurkat et al., 2011). Based on this assumption, the amount of H_2SO_4 emitted per simulation is found according to Eq. B3 in Appendix B.
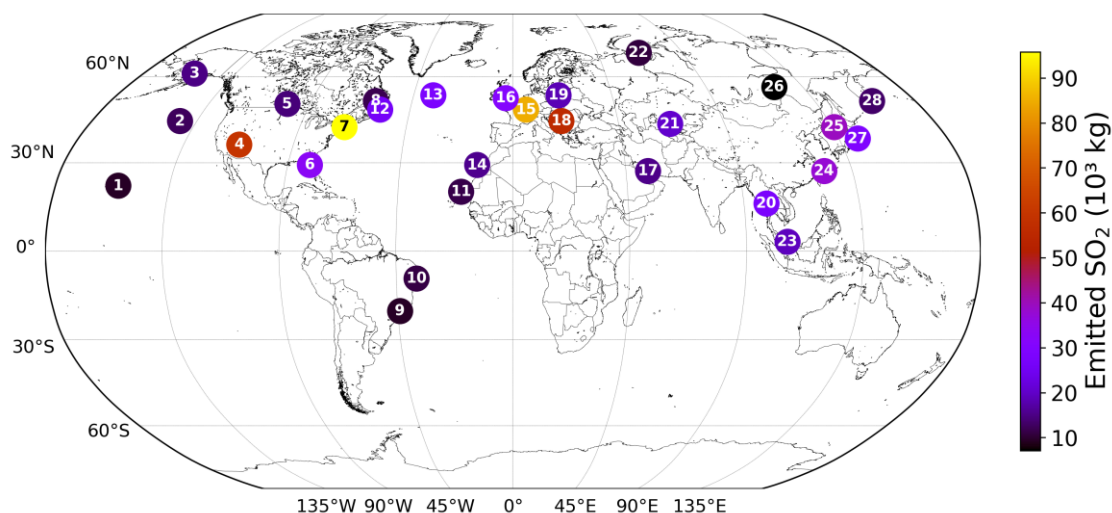

Figure 2 – The 28 emission points at which SO_2 and H_2SO_4 are emitted are represented as numbered circles. This horizontal distribution of points is shown for a pressure altitude of 240 hPa (~10.6 km). The amounts emitted at each point vary according

to the CMIP6 aviation emissions inventory and are distinguished by the color bar. The exact coordinates and emitted amounts
240 for SO$_2$ and H$_2$SO$_4$ are specified in Table B1 of Appendix B.

2.3 The MADE3 submodel and the SO$_4$ mass transport equations

Aerosol microphysical processes and dynamics are simulated using the MADE3 (Kaiser et al., 2014 and 2019) submodel, a
successor of the MADE (Ackermann et al., 1998; Lauer et al., 2005) and MADE-in (Aquila et al., 2011) submodels. The
performance of MADE3 has been extensively evaluated. Its ground-level aerosol mass concentrations have been compared to
245 data from a network of measurement stations and satellite observations. Its simulated vertical profiles of the mass mixing ratios
and particle number distributions have been evaluated against aircraft campaign data. Overall, the model has demonstrated
satisfactory alignment with observational data, although MADE3 tends to produce larger average sulfate concentrations near
the surface, with biases ranging from 13% to 92% when compared to observations from measurement stations (Kaiser et al.,
2019).

250 The MADE3 submodel considers nine types of aerosols: SO$_4$, BC, sea spray (Na), H$_2$O, chloride (Cl), mineral dust (DU), NH$_4$,
NO$_3$ and particulate organic matter (POM). Each aerosol type is further classified into nine modes, which result from the
combination of three size categories (Aitken (subscript 'k'), accumulation (subscript 'a') and coarse (subscript 'c')) and three
mixing states (soluble (subscript 's'), insoluble (subscript 'i') and mixed (subscript 'm')). MADE3 therefore adopts a modal
approach, where the total particle number distribution $n(\ln D)$ of an aerosol is obtained by the superposition of its nine
255 lognormal distributions (one for each mode M) according to Eq. 1a (Aquila et al., 2011; Kaiser et al., 2014; Boucher, 2015):

$$n(\ln D) = \sum_{M=1}^{9} \frac{N_M}{\sqrt{2\pi}\ln\sigma_M} \exp\left[-\frac{\left(\ln D - \ln D_{g,M}\right)^2}{2\ln^2\sigma_{g,M}}\right], \qquad \text{(Eq. 1a)}$$

where N_M is the total number concentration for mode M, $D_{g,M}$ is the median diameter and $\sigma_{g,M}$ is the geometric standard
deviation. Assuming spherical particles, the mass distribution $m(\ln D)$ is obtained by multiplying Eq. 1a by the particle density
ρ_M and cubic diameter D^3 according to Eq. 1b:

$$m(\ln D) = \sum_{M=1}^{9} \frac{\pi}{6}\rho_M D^3 \frac{N_M}{\sqrt{2\pi}\ln\sigma_M} \exp\left[-\frac{\left(\ln D - \ln D_{g,M}\right)^2}{2\ln^2\sigma_{g,M}}\right]. \qquad \text{(Eq. 1b)}$$

The Aitken mode is the smallest size range resolved by MADE3 and consists of particles around 10 nm, the accumulation
mode includes aerosols roughly 100 nm in diameter, and the coarse mode is the largest, with particle sizes of ~1 μm (Kaiser
et al., 2014). Figure 3 describes the differences across the three mixing states for SO$_4$. The soluble state (Fig. 3a) consists
entirely of soluble species like SO$_4$, NO$_3$ or others. Externally mixed or insoluble (Fig. 3b) aerosols contain a non-volatile core

265 (e.g. black carbon or mineral dust) with a total soluble mass fraction θ below 10% while internally mixed or mixed (Fig. 3c) aerosols have the same structure, but θ is larger than 10%.

$\theta = 100\%$ $\theta \leq 10\%$ $\theta > 10\%$

(a) Soluble   (b) Externally mixed or insoluble   (c) Internally mixed or mixed
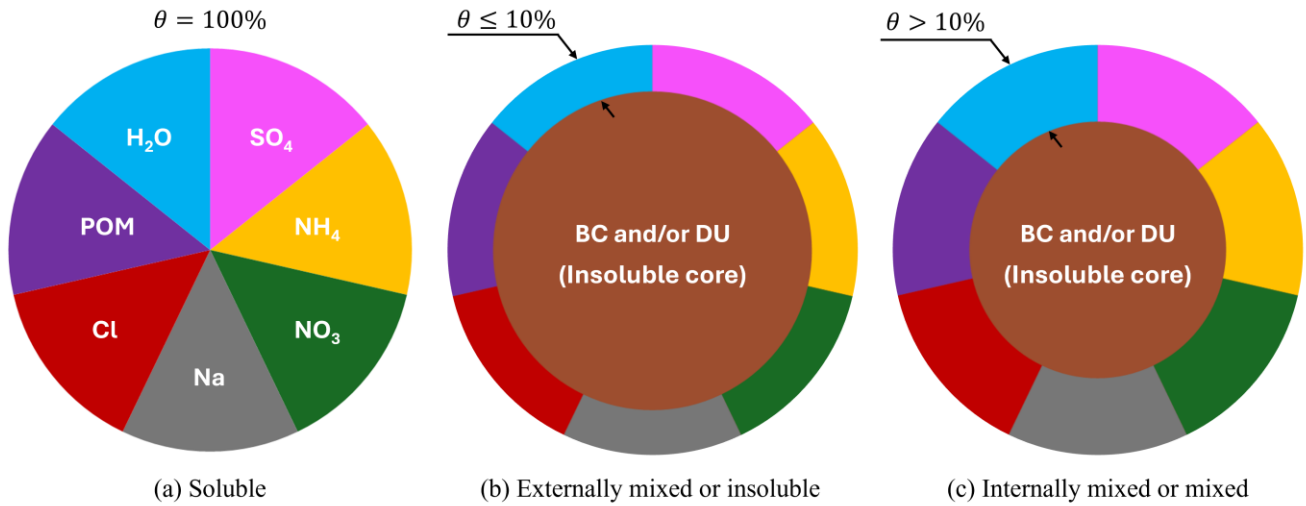
Figure 3 – The three aerosol mixing states according to MADE3. (a) Soluble state, where each of the seven colors represents a soluble species, (b) externally mixed or "insoluble" state where the total soluble mass fraction θ is at most 10% and (c) internally mixed or simply "mixed" state where the total soluble mass fraction θ is above 10%. BC and DU denote the insoluble

270 black carbon or mineral dust core, respectively. Figure is inspired by Kaiser et al. (2014).

The MADE3 submodel calculates tracer tendencies for both mass and particle number mixing ratios across these nine modes and nine species. These tendencies encompass several microphysical processes: gas-particle partitioning (subscript "gtp"), condensation (subscript "cond"), nucleation (subscript "nucl"), coagulation (subscript "coag"), particle growth (subscript "gr") and aging (subscript "ag"). The general form of the governing differential equations for the mass mixing ratios $C_{I,M}$ of an

275 aerosol species I in mode M is therefore given by Eq. 2 (Aquila et al., 2011):

$$\frac{\partial C_{I,M}}{\partial t} = R\left(C_{I,M}\right) + \frac{\partial C_{I,M}}{\partial t}\Big|_{gtp} + \frac{\partial C_{I,M}}{\partial t}\Big|_{cond} + \frac{\partial C_{I,M}}{\partial t}\Big|_{nucl} + \frac{\partial C_{I,M}}{\partial t}\Big|_{coag} + \frac{\partial C_{I,M}}{\partial t}\Big|_{gr} + \frac{\partial C_{I,M}}{\partial t}\Big|_{ag}. \qquad \text{(Eq. 2)}$$

The term $R\left(C_{I,M}\right)$ indicates the variation of aerosol mass concentrations as a result of removal (e.g. dry and wet deposition) and transport phenomena like convection, advection or turbulent mixing processes that are all handled outside of MADE3 by other submodels. These include sedimentation (handled by the SEDI submodel), dry deposition (handled by the DDEP

280 submodel), wet deposition (handled by the SCAV submodel) as well as mixing from atmospheric turbulence (handled in Eulerian representation by the submodel E5VDIFF (Supplement of Emmerichs et al., 2021) and in Lagrangian representation by the submodel LGTMIX (Brinkop and Jöckel, 2019)).

11

The focus of this study is on aerosols containing SO_4 (I = SO_4) and their nine modes, for which the following simplifications may be applied to Eq. 2:

285

1. $\left.\dfrac{\partial C_{SO_4,M}}{\partial t}\right|_{gtp} = 0$. The gas-particle partitioning term is neglected for SO_4, as it is assumed that H_2SO_4 has an equilibrium vapor pressure that is low enough so that it is fully transferred from the gas to the aerosol phase at each time step. The reverse conversion is also not possible, i.e., H_2SO_4 cannot re-evaporate (Kaiser et al., 2014). For this reason, this process in MADE3 is handled by the coagulation routine and hence accounted for in the "coag" term.

2. $\left.\dfrac{\partial C_{SO_4,M \neq ks}}{\partial t}\right|_{nucl} = 0$. The nucleation term for SO_4 applies exclusively to the mass mixing ratio of the soluble Aitken

290

mode (M = ks) as freshly formed particles via the binary homogeneous nucleation between H_2SO_4 and H_2O are assumed to instantaneously produce soluble SO_4 aerosols in the Aitken mode size range (Aquila et al., 2011; Kaiser et al., 2014; Kaiser et al., 2019).

3. $\left.\dfrac{\partial C_{SO_4,M=\{ks,as,cs\}}}{\partial t}\right|_{ag} = 0$. The aging process changes aerosols from the insoluble to the mixed modes when their soluble mass fractions exceed a critical threshold of 10%. Experimental studies (Weingartner et al., 1997; Khalizov et al.,

295

2009) have shown that aerosols with soluble mass fractions above this threshold will exhibit hygroscopic growth and expand by H_2O uptake (Aquila et al., 2011). Consequently, the aging tendency only influences the insoluble and mixed modes.

By applying these three assumptions to Eq. 2, we derive the nine differential equations for the mass mixing ratio of each SO_4 aerosol mode (Eq. 3). Each term is explained in greater detail in the coming sections.

300

$$\frac{\partial C_{SO_4,M}}{\partial t} = \begin{cases} R\left(C_{SO_4,M}\right) + \left.\dfrac{\partial C_{SO_4,M}}{\partial t}\right|_{cond} + \left.\dfrac{\partial C_{SO_4,M}}{\partial t}\right|_{nucl} + \left.\dfrac{\partial C_{SO_4,M}}{\partial t}\right|_{coag} + \left.\dfrac{\partial C_{SO_4,M}}{\partial t}\right|_{gr} & ; M \equiv ks \\[2ex] R\left(C_{SO_4,M}\right) + \left.\dfrac{\partial C_{SO_4,M}}{\partial t}\right|_{cond} + \left.\dfrac{\partial C_{SO_4,M}}{\partial t}\right|_{coag} + \left.\dfrac{\partial C_{SO_4,M}}{\partial t}\right|_{gr} + \left.\dfrac{\partial C_{SO_4,M}}{\partial t}\right|_{ag} & ; M \equiv ki, km, ai, am, ci, cm \\[2ex] R\left(C_{SO_4,M}\right) + \left.\dfrac{\partial C_{SO_4,M}}{\partial t}\right|_{cond} + \left.\dfrac{\partial C_{SO_4,M}}{\partial t}\right|_{coag} + \left.\dfrac{\partial C_{SO_4,M}}{\partial t}\right|_{gr} & ; M \equiv as, cs \end{cases}$$ (Eq. 3)

2.3.1 The nucleation tendency

Homogeneous nucleation between H_2SO_4 and H_2O is a critical process behind the formation of SO_4 aerosols in the atmosphere and is calculated in MADE3 by means of a parameterization by Vehkamäki et al. (2002) for the nucleation rate J. The parameterization of J is applicable for atmospheric temperatures T between 230.15 K and 305.15 K (typical of the troposphere

305

and stratosphere), relative humidities (RH) from 0.01% and 100% and sulfuric acid concentrations ($C_{H_2SO_4}$) between 10^4 and 10^{11} molecules per cm^3. In an earlier version of MADE3 (version 2.0b; Kaiser et al., 2014), it was assumed that the newly

nucleated sulfate particles were all characterized by a representative wet diameter of 3.5 nm, although in reality they are likely to be smaller and grow to more comparable sizes via other processes like coagulation and condensation, as is acknowledged by Binkowski and Roselle (2003). In the more recent MADE3 release (version 3.0; Kaiser et al., 2019), freshly formed particles are considered to have a dry diameter of 10 nm to implicitly account for the rapid growth to larger sizes within a few hours, a phenomenon that cannot yet be resolved by global models. Compared to tropospheric observations of nucleated particles gathered by other studies (Modini et al., 2009; Ueda et al., 2016), such a modification appears to yield more accurate simulation results for the size distribution of aerosol particles and their particle number concentrations. The calculation of the SO_4 nucleation tendency follows Eq. 4:

$$\frac{\partial C_{SO_4,ks}}{\partial t}\bigg|_{nucl} = J(T, RH, C_{H_2SO_4}) \times m_{10nm}(RH) \times \exp\left[\frac{9}{2}\ln^2 \sigma_{ks}\right]. \qquad (Eq.\,4)$$

The term $m_{10nm}(RH)$ denotes the mass of a freshly nucleated spherical SO_4 particle with a dry diameter of 10 nm, which depends on the ambient RH. The factor $\exp\left[\frac{9}{2}\ln^2 \sigma_{ks}\right]$ relates to the geometric standard deviation of the soluble Aitken mode (σ_{ks}) for a lognormal distribution (see explanation of Eq. 1a). It is worth highlighting that nucleation involves only the amount of H_2SO_4 that has not yet been consumed by condensation. In reality, both processes simultaneously compete for H_2SO_4, but within the MADE3 code, the condensation process has been set to occur before nucleation, being the slower one. This consequently amplifies the influence of SO_4 nucleation at locations where condensational sinks for H_2SO_4 are low (Kaiser et al., 2014).

2.3.2 The condensation tendency

The condensation of H_2SO_4 onto pre-existing particles leads to an overall gain in the mass concentration of SO_4. As was mentioned, it is assumed that all of the sulfuric acid is converted entirely from the gas to the aerosol phase and that no re-evaporation occurs in the opposite direction (Kaiser et al., 2014). This SO_4 gain ($\frac{\partial C_{SO_4,M}}{\partial t}\big|_{cond}$) is quantified by Eq. 5 and may be expressed in terms of the dimensionless coefficients $\Omega_{SO_4,M}$ and the amount of condensed H_2SO_4, represented by $\Delta H_2SO_4|_{cond}$, for each aerosol mode M (Whitby et al., 1991; Aquila et al., 2011):

$$\frac{\partial C_{SO_4,M}}{\partial t}\bigg|_{cond} = \Omega_{SO_4,M} \times \frac{\Delta H_2SO_4|_{cond}}{\Delta t}. \qquad (Eq.\,5)$$

The coefficients $\Omega_{SO_4,M}$ measure the modal contribution of the SO_4 growth term for mode M ($G_{SO_4,M}^{(3)}$), which is proportional to the time rate of change of the total volume of aerosol particles in a specific mode M, relative to the sum of all nine modal growth terms, as expressed by Eq. 5a. The variable $\Delta H_2SO_4|_{cond}$ is calculated by solving a first-order linear differential

equation (Eq. 5b) that describes the difference between the gas-phase production rate of sulfuric acid (P) and its condensational loss rate L (Aquila et al., 2011; Kaiser et al., 2014):

$$\Omega_{SO_4,M} = \frac{G_{SO_4,M}^{(3)}}{\sum_{j=1}^{9} G_{SO_4,j}^{(3)}}, \tag{Eq. 5a}$$

$$\frac{dC_{H_2SO_4}(t)}{dt} = P - L \cdot C_{H_2SO_4}(t). \tag{Eq. 5b}$$

The growth rates G featured in Eq. 5a may be computed by finding the harmonic mean of the growth rates for the SO$_4$ aerosol in mode M for two regimes: the free-molecular regime in which collisions between gas molecules are not as frequent and the near-continuum regime in which collisions are frequent enough for the gas to be considered a continuous fluid. Other variables like the saturation vapor pressure and diffusion coefficients of sulfuric acid are also necessary to calculate $\Omega_{SO_4,M}$. Further details on the calculation of the terms in Eq. 5 are provided by Aquila et al. (2011) and Kaiser et al. (2014).

2.3.3 The coagulation tendency

Two types of coagulation processes are distinguished: intra- and intermodal. The former occurs between particles of the same mode and produces aerosols that belong to the same mode as the original ones. The latter occurs between particles from different size and mixing states and results in particles with diameters comparable to the larger of the colliding aerosols. Only intermodal coagulation is therefore relevant for the spatio-temporal evolution of aerosol mass mixing ratios. The contribution to mode M of SO$_4$ resulting from the coagulation of an aerosol in mode p and another in mode q is given by Eq. 6 (Kaiser et al., 2014):

$$\left.\frac{\partial C_{SO_4,M}}{\partial t}\right|_{coag} = \frac{\pi}{6}\sum_{p=1}^{9}\sum_{q=1}^{9}[\left(\delta_{M,\tau_{pq}} - \delta_{M,p}\right)\cdot\frac{C_{SO_4,p}}{\sum_{s=1}^{A}C_{s,p}}\cdot\rho_p\int_0^{\infty}\int_0^{\infty}(D_1)^3\beta(D_1,D_2)n_p(D_1)n_q(D_2)dD_1dD_2 + \cdots$$

$$\cdots + \left(\delta_{M,\tau_{pq}} - \delta_{M,q}\right)\cdot\frac{C_{SO_4,q}}{\sum_{s=1}^{A}C_{s,q}}\cdot\rho_q\int_0^{\infty}\int_0^{\infty}(D_2)^3\beta(D_1,D_2)n_p(D_1)n_q(D_2)dD_1dD_2]. \tag{Eq. 6}$$

The resulting mode for each type of collision in MADE3 is governed by a categorical variable τ_{pq} where p and q are the colliding modes. The possible values of τ_{pq} are detailed in Table 2 from Kaiser et al. (2014), having also a dependency on the particle's soluble mass fraction θ relative to water. The symbol $\delta_{x,y}$ denotes the Kronecker delta, which by definition, assumes a unit value only when both subscripts x and y refer to the same aerosol mode and being zero otherwise. The mass mixing ratios of SO$_4$ corresponding to modes p and q are indicated by $C_{SO_4,p}$ and $C_{SO_4,q}$ and their densities by ρ_p and ρ_q respectively.

The upper bound A of the summations indicates the total number of tracer species s in MADE3, i.e., SO$_4$, NH$_4$, NO$_3$, Na, Cl,

355 POM, BC, DU and H$_2$O. The particle number distribution for modes p and q with particle diameters D_1 and D_2, are written as $n_p(D_1)$ and $n_q(D_2)$, respectively. Lastly, the Brownian coagulation kernels for particles with diameters D_1 and D_2 are expressed as $\beta(D_1, D_2)$, which vary according to the flow regime, i.e., free-molecular or near-continuum. From a more intuitive perspective, they describe the probability of collision between particles of diameters D_1 and D_2 according to Brownian motion. Their complete mathematical formulations may be consulted from Aquila et al. (2011) and from Kaiser et al. (2014).

2.3.4 The growth and aging tendency

360

Although in theory the growth and aging processes are distinct, as in Eq. 2, they are coupled and therefore not given each their own tendency in MADE3. The collective tendency in MADE3 that describes growth and aging is called "rename" and is impacted by both, the condensation and the coagulation processes. The growth process, for instance, refers to the possibility of aerosols growing as they either coagulate or condense onto other pre-existing particles. This may lead to a redistribution in

365 the aerosol modes as particles grow and are reclassified from the Aitken to the accumulation mode. The aging process, in turn, relates to the transformation of insoluble particles via the acquisition of a soluble coating that alters their mixing state from hydrophobic to hydrophilic. By default, if the soluble mass fraction of an insoluble mode reaches a threshold of 10%, the mode is turned to a mixed mode. Aging therefore only impacts the insoluble and mixed modes of SO$_4$ (Aquila et al., 2011; Kaiser et al., 2014).

2.4 The aerosol removal processes and transport

370

The removal processes included in the transport term $R(C_{SO_4,M})$ of Eq. 3 are dry deposition, sedimentation and scavenging of aerosols. Dry deposition refers to the removal of atmospheric aerosols through various interactions with surfaces, such as land or sea, and includes mechanisms such as impaction, interception and diffusion (Farmer et al., 2021). Although sedimentation is a subset of dry deposition, there are two notable differences between them in the coding of each process.

375 Firstly, sedimentation is handled by the SEDI submodel (Kerkweg et al., 2006a) and applies to the entirety of the simulation's vertical domain, whereas dry deposition, handled by the DDEP submodel (Kerkweg et al., 2006a), only applies to the lowermost layer of the model. Secondly, sedimentation solely affects the removal of aerosols and not of gaseous species due to mass considerations.

The dry deposition flux for aerosols is proportional to the dry deposition velocity v_d, which can vary according to the surface

380 type: vegetation (subscript "veg"), soil and snow (subscript "slsn") and water (subscript "wat"). The dry deposition tendency for the SO$_4$ aerosol is represented according to Eq. 7, where parameters β_1, β_2 and β_3 depend on the surface type:

$$\left.\frac{\partial C_{SO_4,M}}{\partial t}\right|_{DDEP} \propto \underbrace{\beta_1 \times v_{d,\text{veg}}(SO_4) + \beta_2 \times v_{d,\text{slsn}}(SO_4) + \beta_3 \times v_{d,\text{wat}}(SO_4)}_{v_d}. \tag{Eq. 7}$$

The sedimentation tendency (Eq. 8) is in turn proportional to the terminal sedimentation velocity v_t, which depends on the Stokes velocity v_{Stokes}, the Cunningham slip flow correction factor (f_{csf}) and the Slinn factor (f_s). The lattter is used to correct

385 for the larger average sedimentation velocity of the lognormal population of aerosols when compared to the sedimentation velocity of a particle with an average particle diameter:

$$\left.\frac{\partial C_{SO_4,M}}{\partial t}\right|_{SEDI} \propto \underbrace{v_{\text{Stokes}}(M) \times f_{\text{csf}}(M) \times f_s(M)}_{v_t}. \tag{Eq. 8}$$

The expressions for the terms needed to compute both dry deposition and sedimentation velocities in Eqs. 7 and 8, are documented by Kerkweg et al. (2006a).

390 Wet deposition of SO_4 refers to scavenging as a result of the precipitation of either ice or liquid water. Aerosol lifetimes are therefore strongly influenced by the interaction between wet and dry deposition processes. Global studies have shown that wet deposition is more important for removing aerosols, but dry deposition is naturally dominant in cloud-free regions where precipitation is unlikely (Farmer et al., 2021). Wet deposition is calculated by the SCAV submodel (Tost et al., 2006) and considers two mechanisms: nucleation scavenging (rainout) and impaction scavenging (washout). The former involves the

395 removal of chemical species from the atmosphere by means of nucleation and subsequent growth of cloud droplets that dissolve them and are then rained out. The latter process refers to the removal of aerosols and gases via their direct collision with raindrops. In a cloud-free region, nucleation scavenging is disregarded and only impaction scavenging is considered. Both mechanisms are contemplated via parameterizations that depend on, e.g., the Brownian motion of aerosols. These are described in further detail by Tost et al. (2006).

400 The transport of SO_4 in a Lagrangian framework is made possible primarily by three submodels: ATTILA, LGTMIX and TREXP. The Atmospheric Tracer Transport in a LAgrangian (ATTILA; Reithmeier and Sausen, 2002; Brinkop and Jöckel, 2019) submodel is the transport scheme for the Lagrangian air parcels and it resolves their advection according to the EMAC wind field and their convective motion. The LaGrangian Tracer MIXing (LGTMIX; Brinkop and Jöckel, 2019) submodel estimates the mass exchange of different chemical species from the isotropic mixing that occurs from atmospheric turbulence.

405 Lastly, although the Tracer Release Experiments from Point sources (TREXP; Jöckel et al., 2010) submodel is not directly involved in the transport of tracers, it assists ATTILA and LGTMIX by defining the initial emission conditions (i.e. position and time of amount emitted) for point sources.

3 The new AIRTRAC v2.0 submodel

The AIRTRAC submodel (Supplement of Grewe et al., 2014a) was originally developed to improve our understanding of
410 some of aviation's gas-phase emissions, more specifically that of NO_x and H_2O. The new AIRTRAC v2.0 submodel now has
expanded capabilities to calculate the contributions of aircraft H_2SO_4 and SO_2 emissions to the nine aerosol modes of SO_4. As
in the gas-phase scheme, source contributions are computed using the tagging approach of Grewe (2013), which is shown in
Eq. 9, and on the method applied by Itahashi et al. (2017) and Wu et al. (2017) (hereafter IW17). In IW17, SO_4 microphysical
processes (e.g. coagulation and condensation) are scaled according to precursor emissions such as SO_2, while removal
415 processes (dry and wet deposition) are scaled relative to the remaining aviation-attributable SO_4. State variables, like the
different aerosol modes of SO_4, are denoted by x_M, where x specifies the chemical species and M the mode. The index j refers
to the number of tagging categories that together add up to the quantity x_M. The term $P_M^j(t)$ indicates the time-dependent
contribution of tagging category j to mode M and F_M is the state-dependent forcing for mode M, which could represent
production and/or loss terms associated with a state variable x_M.

$$420 \quad \frac{\partial}{\partial t} x_M^j = P_M^j(t) + F_M(\mathbf{x}) \frac{\mathbf{x}^{j^T} \nabla F_M(\mathbf{x})}{\mathbf{x}^T \cdot \nabla F_M(\mathbf{x})} \qquad (Eq.\,9)$$

This approach entails the calculation of a fractional weight, $\frac{\mathbf{x}^{j^T} \nabla F_M(\mathbf{x})}{\mathbf{x}^T \cdot \nabla F_M(\mathbf{x})}$, that scales the total forcing term $F_M(\mathbf{x})$ to isolate the
forcing component attributable to tagging category j for mode M. The numerator represents the weighted influence of tagging
category j on the total forcing F_M while the denominator is the total forcing from all categories. This approach ensures that the
sum of the tagged contributions x_M^j from all categories equals the solution of the original ordinary differential equation (ODE)
425 for the untagged total x_M (Grewe, 2013). In the context of this study, two tagging categories are distinguished: aviation (index
"avi") and the remaining sources (index "rem"), which include anthropogenic activity, other transport sectors like shipping
and biogenic emissions. This fraction is applied to the MADE3 tendencies, allowing the model to calculate aviation-attributable
contributions to SO_4 enhancement. By construction, this guarantees a closed budget for the total amount of SO_4 in the
atmosphere, as the sum of the individual sources mathematically equates to the total (Eq. 10).

$$430 \quad \frac{\partial C_{SO_4,M}}{\partial t} = \frac{\partial C_{SO_4,M}}{\partial t}\bigg|^{avi} + \frac{\partial C_{SO_4,M}}{\partial t}\bigg|^{rem} \qquad (Eq.\,10)$$

3.1 Submodel infrastructure

AIRTRAC v2.0 leverages the same technical infrastructure of its predecessor, introducing new Lagrangian tracers dedicated
to SO_4, SO_2 and H_2SO_4 chemistry. Some of these include tracers specific to individual aerosol microphysical processes such
as coagulation, enabling the estimation of each process's influence on an aerosol mode. A new subroutine called

435 "airtrac_aerosol_integrate" was created to handle the calculation of aerosol chemistry along the Lagrangian air parcel trajectories. The AIRTRAC control (CTRL) and coupling (CPL) namelists have also been adapted to now allow the user to select the value of "airtrac_mode", which should be set to "1" when studying SO_4 aerosols and to "2" for the gas-phase analysis mode.

3.2 Tracking aviation SO_2 and H_2SO_4 emissions

440 As SO_2 and H_2SO_4 are both precursors of SO_4 and are directly emitted by aircraft, their evolution throughout the course of a simulation must be tracked to properly account for aviation's impact on sulfate. The key gas-phase, tropospheric reaction involving SO_2 that leads to the production of H_2SO_4 in the chemistry mechanism adopted in this study is represented by the net Reaction R4:

$$SO_2 + OH \rightarrow H_2SO_4 + HO_2. \tag{R4}$$

445 The evolution of aviation SO_2 is simplified and described in AIRTRAC as a pure loss process, where it is oxidized to form H_2SO_4 according to Reaction R4. While processes such as scavenging contribute to SO_2 removal, these are excluded from the analysis due to the computational constraints arising from the difficulty of storing all of the liquid-phase tracers associated with the production of SO_4 from SO_2 (Tost et al., 2006). These removal processes primarily affect liquid-phase species anyway and thus have a smaller impact on the simulated gas-phase SO_2. Consequently, the mixing ratio of aviation-attributable SO_2

450 $(C_{SO_2}|^{avi})$, is based on the initial amount emitted into the atmosphere $(C_{SO_2}(t = 0))$ and the production rate of H_2SO_4 from SO_2 that is provided by the MECCA submodel $(P_{H_2SO_4})$, as is illustrated by Eq. 11. Unlike in Eq. 3, the term $R(C_{SO_2})$ only contemplates the effects of isotropic turbulent mixing:

$$C_{SO_2}\Big|^{avi} = \underbrace{C_{SO_2}(t = 0)}_{\text{Emission}} - \underbrace{\frac{C_{SO_2}\big|^{avi}}{C_{SO_2}\big|^{avi} + C_{SO_2}\big|^{rem}}}_{\text{Tagging ratio}} \times \underbrace{\frac{M_{SO_2}}{M_{H_2SO_4}}}_{\text{Molar masses}} \times \underbrace{P_{H_2SO_4}}_{\text{Production rate}} \times \Delta t + \underbrace{R(C_{SO_2})}_{\text{Turbulence}}. \tag{Eq. 11}$$

In theory, the tagging ratio that scales the aviation-attributable SO_2 in Eq. 11 should consider the amount of OH emanating

455 from both, aviation and other sources, and therefore be expressed as $\frac{1}{2} \times \left(\frac{C_{SO_2}|^{avi}}{C_{SO_2}|^{avi} + C_{SO_2}|^{rem}} + \frac{C_{OH}|^{avi}}{C_{OH}|^{avi} + C_{OH}|^{rem}} \right)$, corresponding to the case of bimolecular reactions by Grewe et al. (2010) and Grewe (2013). However, this contribution is omitted in Eq. 11, as this study focuses exclusively on the influence of aviation SO_2 and H_2SO_4 emissions on SO_4. Since OH is not directly emitted by aircraft, fully tracking it would at least require other gas-phase aircraft emissions like NO_x and CO and their chemical cycling in the atmosphere with other compounds like HO_2 and O_3 to be completely followed, which is beyond the

460   scope of this assessment. The production rate $P_{H_2SO_4}$ is the amount of H_2SO_4 produced from the oxidation of SO_2, so it must

be converted into the equivalent amount of SO_2 loss by multiplying it by the ratio of molar masses $\left(\frac{M_{SO_2}}{M_{H_2SO_4}}\right)$.

To track the evolution of gas-phase, aviation-attributable H_2SO_4, the amount produced from the conversion of SO_2 described

in Eq. 11 must be considered along with two primary sinks: the binary nucleation of H_2SO_4 with H_2O and the condensation of

H_2SO_4 onto pre-existing particles, as is represented in Eq. 12. As a limitation to the approach represented by Eq. 11 and Eq.

465   12, only the gas-phase formation of H_2SO_4 (produced from the hydrolysis of SO_3 via Reactions R1 – R3) is considered in our

analysis. The liquid-phase production that involves the oxidation by O_3 and hydrogen peroxide (H_2O_2) of H_2SO_3, which in turn

is formed by the hydrolysis of SO_2 (Sheng et al., 2018; Shostak et al., 2019), is excluded. While this pathway is the dominant

source of sulfuric acid (Textor et al., 2006), incorporating it is challenging, due to the cloud evaporation assumption described

by Tost et al. (2006), which considers that clouds and aqueous-phase species are fully evaporated at the end of each time step.

470   This assumption is used to avoid the high computation and memory costs that would otherwise be required to advect both gas-

and aqueous-phase tracer species. The term $R\left(C_{H_2SO_4}\right)$ therefore again only represents isotropic turbulent mixing.

$$
C_{H_2SO_4}\Big|^{avi} = \underbrace{C_{H_2SO_4}(t=0)}_{\text{Emission}} + \underbrace{\frac{C_{SO_2}\Big|^{avi}}{C_{SO_2}\Big|^{avi} + C_{SO_2}\Big|^{rem}} \times P_{H_2SO_4} \times \Delta t}_{\text{Oxidation of } SO_2} + \cdots
$$

$$
\cdots - \underbrace{\frac{C_{H_2SO_4}\Big|^{avi}}{C_{H_2SO_4}\Big|^{avi} + C_{H_2SO_4}\Big|^{rem}} \times \frac{\partial C_{H_2SO_4}}{\partial t}\Big|^{avi}_{nucl} \times \Delta t}_{\text{Nucleation of } H_2SO_4} + \cdots \qquad \text{(Eq. 12)}
$$

$$
\cdots - \underbrace{\frac{C_{H_2SO_4}\Big|^{avi}}{C_{H_2SO_4}\Big|^{avi} + C_{H_2SO_4}\Big|^{rem}} \times \frac{\partial C_{H_2SO_4}}{\partial t}\Big|^{avi}_{cond} \times \Delta t}_{\text{Condensation of } H_2SO_4} + \underbrace{R\left(C_{H_2SO_4}\right)}_{\text{Turbulence}}
$$

3.3 Aviation's contribution to SO_4 via nucleation and condensation of H_2SO_4

The contribution from aviation to the formation of the soluble Aitken mode of SO_4 via the binary nucleation of H_2SO_4-H_2O is

estimated by applying a tagging ratio to the MADE3 nucleation tendency (Eq. 4). This tagging ratio in Eq. 13 naturally involves

475   H_2SO_4, given that sulfuric acid from aviation ($C_{H_2SO_4}\Big|^{avi}$) drives the nucleation process.

$$
\frac{\partial C_{SO_4,ks}}{\partial t}\Big|^{avi}_{nucl} = \frac{C_{H_2SO_4}\Big|^{avi}}{C_{H_2SO_4}\Big|^{avi} + C_{H_2SO_4}\Big|^{rem}} \times \frac{\partial C_{SO_4,ks}}{\partial t}\Big|_{nucl} \qquad \text{(Eq. 13)}
$$

Aviation's contribution to SO_4 via the condensation of H_2SO_4 is estimated in a fashion similar to Eq. 13, as the tagging ratio is exactly the same (Eq. 14) due to the central role of H_2SO_4 also in this process. The main difference is that the condensation process may contribute to increasing any one of the nine SO_4 aerosol modes.

480
$$\left.\frac{\partial C_{SO_4,M}}{\partial t}\right|_{cond}^{avi} = \frac{\left.C_{H_2SO_4}\right|^{avi}}{\left.C_{H_2SO_4}\right|^{avi} + \left.C_{H_2SO_4}\right|^{rem}} \times \left.\frac{\partial C_{SO_4,M}}{\partial t}\right|_{cond} \tag{Eq. 14}$$

3.4 Aviation's contribution to SO_4 via particle coagulation, growth and aging

We first derive an expression for aviation's contribution to the soluble Aitken mode (M = ks) of SO_4 via coagulation by applying the tagging formulation in Eq. 9. For clarity and conciseness in representing the full coagulation equation (Eq. 6), vector notation is introduced for the state variables $\mathbf{x}$ according to Eq. 15 for all nine aerosol modes, where x_1, for instance, is

485 the mass concentration of mode "ks", i.e., $x_1 \equiv C_{SO_4,ks}$. Each state variable x_i represents the sum of contributions from all sources, in this study the sources are $j = \{avi, rem\}$.

$$\mathbf{x} = \begin{bmatrix} x_1 \\ x_2 \\ x_3 \\ x_4 \\ x_5 \\ x_6 \\ x_7 \\ x_8 \\ x_9 \end{bmatrix} = \begin{bmatrix} x_1^{avi} + x_1^{rem} \\ x_2^{avi} + x_2^{rem} \\ x_3^{avi} + x_3^{rem} \\ x_4^{avi} + x_4^{rem} \\ x_5^{avi} + x_5^{rem} \\ x_6^{avi} + x_6^{rem} \\ x_7^{avi} + x_7^{rem} \\ x_8^{avi} + x_8^{rem} \\ x_9^{avi} + x_9^{rem} \end{bmatrix} = \begin{bmatrix} C_{SO_4,ks} \\ C_{SO_4,km} \\ C_{SO_4,ki} \\ C_{SO_4,as} \\ C_{SO_4,am} \\ C_{SO_4,ai} \\ C_{SO_4,cs} \\ C_{SO_4,cm} \\ C_{SO_4,ci} \end{bmatrix} \tag{Eq. 15}$$

The coagulation kernels are also more compactly rewritten (Eqs. 16a and 16b), where p and q are the modes of the colliding particles. Additionally, the summation in the denominator of Eq. 6 for an aerosol in mode p with a diameter D_1 will be

490 reformulated more succinctly as $\sum_{s=1}^{A=9} C_{s,p} = x_1 + C_p$, where $C_p = C_{NH_4,p} + C_{NO_3,p} + C_{Na,p} + C_{Cl,p} + C_{POM,p} + C_{BC,p} + C_{DU,p} + C_{H_2O,p}$. We also note that $f_{p,q} = f'_{q,p}$.

$$f_{p,q} = \int_0^\infty \int_0^\infty (D_1)^3 \beta(D_1, D_2) n_p(D_1) n_q(D_2) dD_1 dD_2 \tag{Eq. 16a}$$

$$f'_{p,q} = \int_0^\infty \int_0^\infty (D_2)^3 \beta(D_1, D_2) n_p(D_1) n_q(D_2) dD_1 dD_2 \tag{Eq. 16b}$$

When evaluating the double summations of Eq. 6 for the case M = ks, it is worth noting that for intermodal coagulation, i.e., $p \neq q$, the value of $\tau_{pq} \neq$ ks. In other words, when two particles from different modes collide, the destination mode will never be the soluble Aitken mode (Table 2 from Kaiser et al., 2014). It follows that since $\tau_{pq} \neq$ ks, the Kronecker deltas depending on τ_{pq} will be zero: $\delta_{ks,\tau_{pq}} = 0$. In contrast, the Kronecker deltas $\delta_{ks,p}$ and $\delta_{ks,q}$ evaluate to "1" whenever either mode p or q is also ks. We note that if $p = q$, the coagulation tendency is zero, as intramodal collisions do not affect mass concentrations. It is also essential to recall that the destination mode of the coagulated particle depends on the soluble mass fraction θ of the final particle. This dependency implies that the coagulation tendency for each of the nine modes will be a piecewise function (F_1) in terms of θ. Combining Eqs. 6 and 16 leads to the more compact formulation of the coagulation tendency for mode ks (Eq. 17).

$$\frac{\partial x_1}{\partial t}\bigg|_{\text{coag}} = F_1(\mathbf{x}) = \begin{cases} -A \dfrac{x_1}{x_1 + C_1}; \; \theta = 1 \text{ (Soluble)} \\[2mm] -A' \dfrac{x_1}{x_1 + C_1}; \; 0.1 \leq \theta < 1 \text{ (Mixed)} \\[2mm] -A'' \dfrac{x_1}{x_1 + C_1}; \; 0 \leq \theta < 0.1 \text{ (Insoluble)} \end{cases} \qquad (\text{Eq. 17})$$

The coefficients A, A' and A'' are defined as follows, where the subscripts refer to the colliding modes (see Eq. 15 for details):

$$A = \rho_1 \frac{\pi}{6} [f_{1,4} + f_{1,7}],$$

$$A' = \rho_1 \frac{\pi}{6} [f_{1,3} + f_{1,5} + f_{1,6} + f_{1,8} + f'_{2,1}],$$

$$A'' = \rho_1 \frac{\pi}{6} [f_{1,3} + f_{1,6} + f_{1,9}].$$

The negative sign present across all cases of θ in Eq. 17 reflects that any intermodal coagulation event involving a particle in the ks mode will always result in its conversion to other aerosol modes. Applying Eq. 9 to Eq. 17 results in the following expression for the contribution of aviation to mode ks via coagulation:

$$\frac{\partial x_1^{\text{avi}}}{\partial t}\bigg|_{\text{coag}} = F_1(\mathbf{x}) \frac{\mathbf{x}^{j^T} \nabla F_1(\mathbf{x})}{\mathbf{x}^T \nabla F_1(\mathbf{x})}.$$

Evaluating the sensitivity fraction leads to the final expression for $\frac{\partial x_1^{\text{avi}}}{\partial t}\big|_{\text{coag}}$, where K = {A, A', A''}:

$$\frac{\partial x_1^{\text{avi}}}{\partial t}\bigg|_{\text{coag}} = F_1(\mathbf{x}) \frac{\left(x_1^{\text{avi}}, x_2^{\text{avi}}, x_3^{\text{avi}}, \dots, x_9^{\text{avi}}\right) \left(\dfrac{-KC_1}{(x_1 + C_1)^2}, 0, 0, \dots, 0\right)^{\text{T}}}{\left(x_1, x_2, x_3, \dots, x_9\right) \left(\dfrac{-KC_1}{(x_1 + C_1)^2}, 0, 0, \dots, 0\right)^{\text{T}}} = F_1(\mathbf{x}) \frac{x_1^{\text{avi}}}{x_1}. \qquad (\text{Eq. 18})$$

Based on the result from Eq. 18, the tagging ratio $\frac{x_1^{avi}}{x_1}$ for the coagulation tendency of SO_4 in mode ks according to Grewe

515 (2013) is the ratio of soluble Aitken mode sulfate, $C_{SO_4,ks}\big|^{avi}$, to the total amount of this aerosol across all other sources, i.e.,

$\frac{x_1^{avi}}{x_1} = \frac{C_{SO_4,ks}\big|^{avi}}{C_{SO_4,ks}\big|^{avi} + C_{SO_4,ks}\big|^{rem}}$. Typically, the form of this ratio varies with θ, but for mode ks, the same structure is obtained

(only K varies). This result is verified analytically as Eq. 10 is upheld. The derivation for the remaining eight aerosol modes is

included in Appendix C.

We highlight that this derivation considers the following simplifying assumptions:

520   1.   Coagulation kernels β and terms C_p are independent of the state variables x_i.

     2.   Coagulation between modes p and q leads to the same outcome as the coagulation between modes q and p.

Given the complexity of the tagging ratios for the remaining modes resulting from the extra computational effort of storing
and passing all of the coagulation kernels across submodels and the added difficulty in implementing θ-dependent piecewise
functions (e.g. Eq. C2 in Appendix C), we consider the method applied by IW17 in which secondary particulate sulfate (SO_4

525 that is indirectly produced from the oxidation of SO_2) production from source j is tagged as a function of the emitted SO_2 (i.e.,

tagging ratio is $\frac{SO_2|^j}{\sum SO_2}$). In this study, both SO_2 and H_2SO_4 are precursors of particulate sulfate that are directly emitted and

tracked by AIRTRAC. Since SO_2 must first be oxidized to H_2SO_4 before being converted to SO_4, our tagging ratio involves

the latter:

$$\frac{\partial C_{SO_4,M}}{\partial t}\bigg|^{avi}_{coag} = \frac{C_{H_2SO_4}\big|^{avi}}{C_{H_2SO_4}\big|^{avi} + C_{H_2SO_4}\big|^{rem}} \times \frac{\partial C_{SO_4,M}}{\partial t}\bigg|_{coag}. \tag{Eq. 19}$$

530 Lastly, the growth and aging processes, represented by the "rename" tendency, are formulated analogously to the coagulation
(Eq. 18) and condensation (Eq. 14) tendencies, as these processes similarly depend on coagulation and condensation
mechanisms. The aviation-attributable growth and aging contribution is therefore written as:

$$\frac{\partial C_{SO_4,M}}{\partial t}\bigg|^{avi}_{gr} + \frac{\partial C_{SO_4,M}}{\partial t}\bigg|^{avi}_{ag} = \frac{\partial C_{SO_4,M}}{\partial t}\bigg|^{avi}_{rename} = \frac{C_{H_2SO_4}\big|^{avi}}{C_{H_2SO_4}\big|^{avi} + C_{H_2SO_4}\big|^{rem}} \times \frac{\partial C_{SO_4,M}}{\partial t}\bigg|_{rename}. \tag{Eq. 20}$$

3.5 Aviation-attributable SO_4 removal processes

535 The removal of aviation-produced SO_4 through the three processes described in Section 2.4 (dry deposition, sedimentation,
and scavenging) is scaled by the aviation-attributable SO_4 tagging ratio. This reflects the fact that removal processes are directly

proportional to the pollutant to be removed and is consistent with the method of IW17. In other words, the removal rate should be linearly proportional to the amount of the aerosol present in the atmosphere as the removal tendency should be approximately zero once the aviation-induced aerosols are nearly depleted. The dry deposition (DDEP), sedimentation (SEDI) and scavenging (SCAV) tendencies for aviation aerosols are therefore defined by Eq. 21:

$$\left.\frac{\partial C_{SO_4,M}}{\partial t}\right|_i^{avi} = \frac{\left.C_{SO_4}\right|^{avi}}{\left.C_{SO_4}\right|^{avi} + \left.C_{SO_4}\right|^{rem}} \times \left.\frac{\partial C_{SO_4,M}}{\partial t}\right|_i \; ; i = \{DDEP, SEDI, SCAV\}. \tag{Eq. 21}$$

3.6 An overview of the tagging equations for aviation SO_4

By combining the tagging formulations for all aerosol microphysical and removal processes, we provide a consolidated overview of the non-linear tagging differential equations as a function of process tendencies to track the transport of aviation SO_4 across all nine modes. Equation 22 applies only to mode ks, while Eq. 23 to the remaining modes. The isotropic turbulent mixing parameterization from LGTMIX is represented by $R(C_{SO_4,M})$.

$$\left.\frac{\partial C_{SO_4,ks}}{\partial t}\right|^{avi} = \frac{\left.C_{H_2SO_4}\right|^{avi}}{\left.C_{H_2SO_4}\right|^{avi} + \left.C_{H_2SO_4}\right|^{rem}} \times \left(\underbrace{\left.\frac{\partial C_{SO_4,ks}}{\partial t}\right|_{nucl}}_{\text{Nucleation}} + \underbrace{\left.\frac{\partial C_{SO_4,ks}}{\partial t}\right|_{cond}}_{\text{Condensation}} + \underbrace{\left.\frac{\partial C_{SO_4,ks}}{\partial t}\right|_{coag}}_{\text{Coagulation}} + \cdots \right.$$

$$\left. \cdots + \underbrace{\left.\frac{\partial C_{SO_4,ks}}{\partial t}\right|_{rename}}_{\text{Growth \& Aging}} \right) - \frac{\left.C_{SO_4}\right|^{avi}}{\left.C_{SO_4}\right|^{avi} + \left.C_{SO_4}\right|^{rem}} \times \left(\underbrace{\left.\frac{\partial C_{SO_4,ks}}{\partial t}\right|_{DDEP}}_{\text{Dry Deposition}} + \underbrace{\left.\frac{\partial C_{SO_4,ks}}{\partial t}\right|_{SEDI}}_{\text{Sedimentation}} + \underbrace{\left.\frac{\partial C_{SO_4,ks}}{\partial t}\right|_{SCAV}}_{\text{Scavenging}} \right) \cdots \tag{Eq. 22}$$

$$\cdots + \underbrace{R(C_{SO_4,ks})}_{\text{Turbulence}}$$

Lastly, for the remaining modes $M = \{km, ki, as, am, ai, cs, cm, ci\}$:

$$\left.\frac{\partial C_{SO_4,M}}{\partial t}\right|^{avi} = \frac{\left.C_{H_2SO_4}\right|^{avi}}{\left.C_{H_2SO_4}\right|^{avi} + \left.C_{H_2SO_4}\right|^{rem}} \times \left(\underbrace{\left.\frac{\partial C_{SO_4,M}}{\partial t}\right|_{cond}}_{\text{Condensation}} + \underbrace{\left.\frac{\partial C_{SO_4,ks}}{\partial t}\right|_{coag}}_{\text{Coagulation}} + \underbrace{\left.\frac{\partial C_{SO_4,ks}}{\partial t}\right|_{rename}}_{\text{Growth \& Aging}} \right) + \cdots \tag{Eq. 23}$$

23

$$\ldots - \frac{C_{SO_4}\big|^{avi}}{C_{SO_4}\big|^{avi} + C_{SO_4}\big|^{rem}} \times \left(\underbrace{\frac{\partial C_{SO_4,M}}{\partial t}\bigg|_{DDEP}}_{\text{Dry Deposition}} + \underbrace{\frac{\partial C_{SO_4,M}}{\partial t}\bigg|_{SEDI}}_{\text{Sedimentation}} + \underbrace{\frac{\partial C_{SO_4,M}}{\partial t}\bigg|_{SCAV}}_{\text{Scavenging}} \right) + \underbrace{R\big(C_{SO_4,M}\big)}_{\text{Turbulence}}.$$

As it would be much more computationally demanding to develop a complete chemistry mechanism within every air parcel defined in a simulation, AIRTRAC leverages the background chemistry from the EMAC model by linearly scaling these non-linear background responses with the emission amount. Although this approach introduces simplifications like discarding

550   feedback effects between the emission and background, the computational requirements are decreased by at least one to two

orders of magnitude (Maruhashi et al., 2024). To linearize Eqs. 22 and 23, the tagging ratios $\frac{C_{H_2SO_4}\big|^{avi}}{C_{H_2SO_4}\big|^{avi} + C_{H_2SO_4}\big|^{rem}}$ and

$\frac{C_{SO_4}\big|^{avi}}{C_{SO_4}\big|^{avi} + C_{SO_4}\big|^{rem}}$ must be linearized. As it is comparable to the rational function $f(x) = \frac{x}{x+k}$, where k is a real number, the

tagging ratios may be approximated with a first-order McLaurin polynomial: $\frac{x}{x+k} \approx \frac{x}{k} \implies \frac{C_{H_2SO_4}\big|^{avi}}{C_{H_2SO_4}\big|^{avi} + C_{H_2SO_4}\big|^{rem}} \approx \frac{C_{H_2SO_4}\big|^{avi}}{C_{H_2SO_4}\big|^{rem}}$

and $\frac{C_{SO_4}\big|^{avi}}{C_{SO_4}\big|^{avi} + C_{SO_4}\big|^{rem}} \approx \frac{C_{SO_4}\big|^{avi}}{C_{SO_4}\big|^{rem}}$. The set of linearized tagging equations implemented in AIRTRAC v2.0 is therefore

555   represented by Eqs. 24 and 25:

$$\frac{\partial C_{SO_4,ks}}{\partial t}\bigg|^{avi} = \frac{C_{H_2SO_4}\big|^{avi}}{C_{H_2SO_4}\big|^{rem}} \times \left(\underbrace{\frac{\partial C_{SO_4,ks}}{\partial t}\bigg|_{nucl}}_{\text{Nucleation}} + \underbrace{\frac{\partial C_{SO_4,ks}}{\partial t}\bigg|_{cond}}_{\text{Condensation}} + \underbrace{\frac{\partial C_{SO_4,ks}}{\partial t}\bigg|_{coag}}_{\text{Coagulation}} + \underbrace{\frac{\partial C_{SO_4,ks}}{\partial t}\bigg|_{rename}}_{\text{Growth \& Aging}} \right) + \ldots$$

(Eq. 24)

$$\ldots - \frac{C_{SO_4}\big|^{avi}}{C_{SO_4}\big|^{rem}} \times \left(\underbrace{\frac{\partial C_{SO_4,ks}}{\partial t}\bigg|_{DDEP}}_{\text{Dry Deposition}} + \underbrace{\frac{\partial C_{SO_4,ks}}{\partial t}\bigg|_{SEDI}}_{\text{Sedimentation}} + \underbrace{\frac{\partial C_{SO_4,ks}}{\partial t}\bigg|_{SCAV}}_{\text{Scavenging}} \right) + \underbrace{R\big(C_{SO_4,ks}\big)}_{\text{Turbulence}}.$$

For the remaining modes $M = \{km, ki, as, am, ai, cs, cm, ci\}$:

$$\frac{\partial C_{SO_4,M}}{\partial t}\bigg|^{avi} = \frac{C_{H_2SO_4}\big|^{avi}}{C_{H_2SO_4}\big|^{rem}} \times \left(\underbrace{\frac{\partial C_{SO_4,M}}{\partial t}\bigg|_{cond}}_{\text{Condensation}} + \underbrace{\frac{\partial C_{SO_4,ks}}{\partial t}\bigg|_{coag}}_{\text{Coagulation}} + \underbrace{\frac{\partial C_{SO_4,ks}}{\partial t}\bigg|_{rename}}_{\text{Growth \& Aging}} \right) + \ldots$$

(Eq. 25)

$$\ldots - \frac{C_{SO_4}\big|^{avi}}{C_{SO_4}\big|^{rem}} \times \left(\underbrace{\frac{\partial C_{SO_4,M}}{\partial t}\bigg|_{DDEP}}_{\text{Dry Deposition}} + \underbrace{\frac{\partial C_{SO_4,M}}{\partial t}\bigg|_{SEDI}}_{\text{Sedimentation}} + \underbrace{\frac{\partial C_{SO_4,M}}{\partial t}\bigg|_{SCAV}}_{\text{Scavenging}} \right) + \underbrace{R\big(C_{SO_4,M}\big)}_{\text{Turbulence}}.$$

4 Application and evaluation of AIRTRAC v2.0

This section presents the application of AIRTRAC v2.0 in examining the transport patterns of aviation-emitted SO_2 and H_2SO_4 and their role in secondary SO_4 formation by comparing two emission points for the July – September 2015 emission scenario. The impact of seasonal shifts to the lifetimes of SO_2, SO_4 and to the mean productive efficiency of SO_4 is also considered. To

560   identify which of these emission points is most likely to lead to interactions with liquid clouds, ESA satellite cloud data (Stengel et al., 2019) is integrated into the analysis. Lastly the spatial distributions of SO_4 volume mixing ratios (VMRs) are compared to output from MADE3 using a perturbation approach and to results from Righi et al. (2023). While the absolute magnitudes obtained from the tagging and perturbation methods are not directly comparable—since they address fundamentally different research questions (Clappier et al., 2017)—their spatial distribution patterns are expected to be more comparable.

565   ### 4.1 Analysis of directly emitted species: SO_2 and H_2SO_4

Figure 4 illustrates the differing transport pathways and impacts of SO_2 emissions originating from emission points 8 and 10, situated in the North and South Atlantic regions, respectively (see Fig. 2). Analogously, Fig. 5 presents the same analysis for H_2SO_4 for the same emission points. Both figures pertain to a 90 d period during the northern winter (July – September, 2015).

4.1.1 SO_2

570   In AIRTRAC v2.0, SO_2 is a tracer that undergoes a pure loss process, as was described by Eq. 11. Figures 4a and b depict the temporal evolution of SO_2 production efficiency and its e-folding time for two emission points, calculated by solving for τ using the exponential decay law: $C(t) = C_0 \cdot e^{-\frac{t}{\tau}}$, where C_0 is the initial concentration and t is the time elapsed since emission. The mean e-folding time at point 8, approximately 27 d, is about 60% larger than the 17 d estimate for emission point 10. This disparity is likely due to the faster downward transport witnessed at point 10 (Fig. 4d), which accelerates SO_2 depletion from

575   larger background OH concentrations in the lower troposphere as a result of increased water vapor levels (Riedel and Lassey, 2008). The magnitudes of these SO_2 e-folding lifetimes (τ) are in reasonable agreement with past studies that estimated e-folding lifetimes ranging from a few days (Beirle et al., 2014) to two weeks in the troposphere (von Glasow et al., 2009). We find that the median SO_2 lifetime between July – September is 14 d (Fig. 7a). SO_2 lifetimes will ultimately vary according to the drastically different depletion rates in the atmosphere (Oppenheimer et al., 1998; Beirle et al., 2014). In contrast, SO_2

580   emitted at point 8 remains at higher altitudes for longer, where the stability and reduced HO_x (OH+HO$_2$) species in the upper

atmosphere leads to slower depletion rates (Fig. 4c). Similar conclusions have been reported in previous studies for other chemical species, particularly in the context of NO_x emissions affecting atmospheric O_3 concentrations, which are likewise oxidized by OH (Frömming et al., 2012; Rosanka et al., 2020; Frömming et al., 2021; Maruhashi et al., 2022).

585 The horizontal distribution associated with emission point 8 (Fig. 4e) shows that air parcels predominantly remain within the Northern Hemisphere, which agrees with previous findings noting that transhemispheric transport is limited (Grewe et al., 2002; Maruhashi et al., 2022). SO_2 emitted at point 10 mainly travels along the southern tropical region, with the largest scaled volume mixing ratios found along lower altitudes near the Equator. The tropical easterlies or trade winds typically acting between 0° and 30° S are the driving force behind the horizontal transport of SO_2 and carry emissions far to the West. The SO_2 production efficiency time series for all 28 emission points for January – March and July – September in 2015 are shown in 590 Figs. S1 and S2 in the Supplement (Maruhashi et al., 2025b) respectively.

4.1.2 H_2SO_4

H_2SO_4 volume mixing ratios along air parcel trajectories are calculated by AIRTRAC v2.0 using Eq. 12, whereby the conversion of SO_2 directly contributes to the formation of H_2SO_4. Consequently, the longer e-folding time for SO_2 at emission point 8 (Fig. 4a) also translates to a prolonged perturbation lifetime for H_2SO_4. Figure 5a indicates that H_2SO_4 persists beyond 595 the 80 d mark, whereas emissions from point 10 are fully depleted around 60 d after emission (Fig. 5b). As was observed by Rosanka et al. (2020) and Frömming et al. (2021) in the context of NO_x-O_3 chemistry, the air parcels that have an early initial descent to more chemically active regions in the lower troposphere tend to produce the largest maximum production efficiencies. This phenomenon is also present in Fig. 5b, where the largest H_2SO_4 production efficiency occurs for the air parcels from emission point 10 that exhibit an early descent.

600 The dependence on SO_2 means that H_2SO_4 production can continue to increase and even peak several days after the initial SO_2 emission, often occurring at locations far from the original source. Figures 5c and d exemplify this pattern as the maximum H_2SO_4 production efficiencies occur at much lower altitudes compared to the emission altitude. In terms of the horizontal distributions, Fig. 5e suggests that SO_2 emitted in the North Atlantic will lead to maximum H_2SO_4 production in parts of Africa and Asia. For an SO_2 emission in the South Atlantic (Fig. 5f), H_2SO_4 production is at a maximum in Central Africa and in 605 South America, resulting from the trade winds transporting the SO_2 to the West. The H_2SO_4 production efficiency time series for all 28 emission points for January – March and July – September in 2015 are shown in Figs. S3 and S4 in the Supplement (Maruhashi et al., 2025b) respectively.
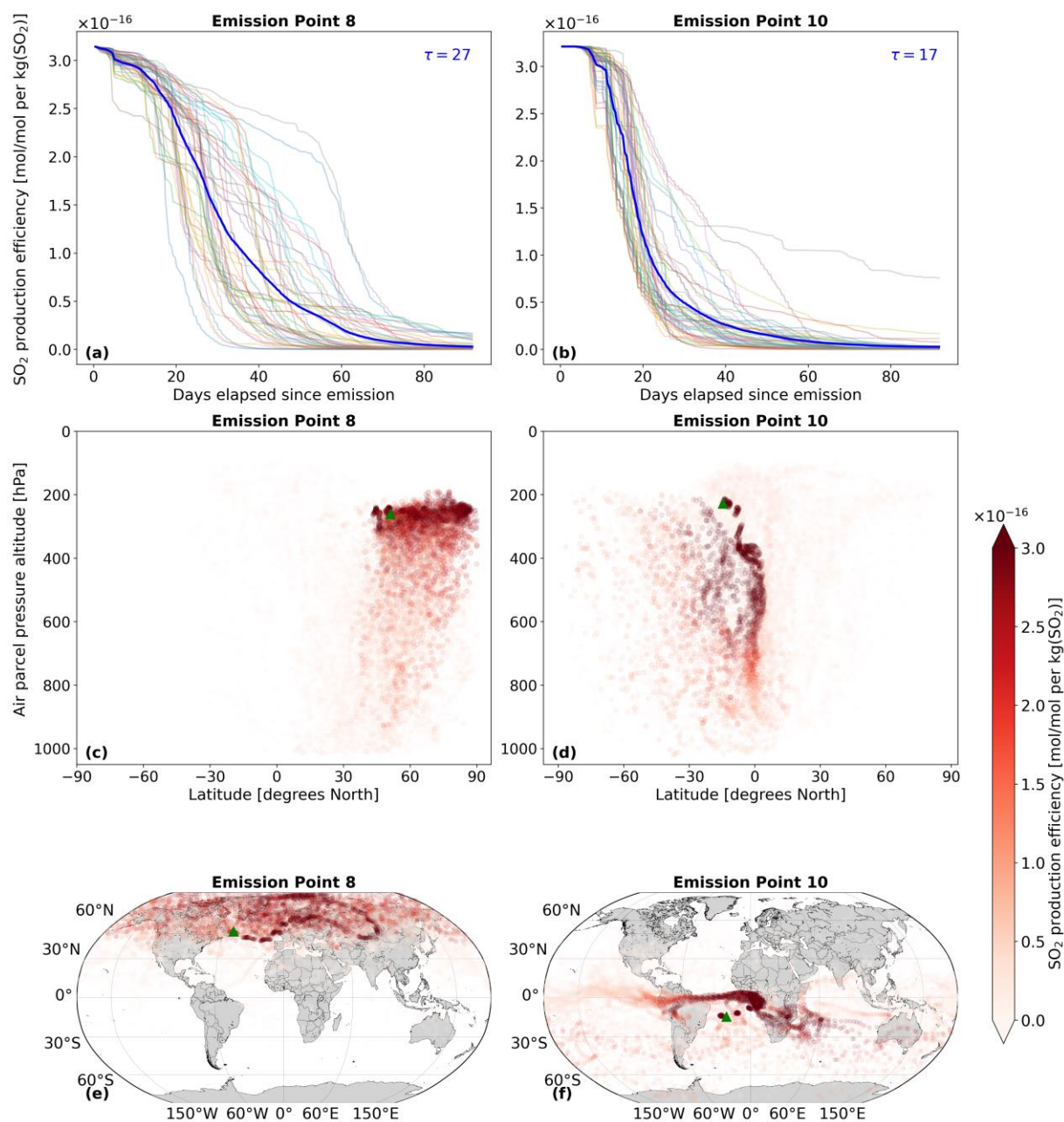
Figure 4 – The spatio-temporal variation of aviation-emitted sulfur dioxide (SO$_2$) scaled by the emission mass for emission points 8 and 10 (see Fig. 2). Panels (a) – (b) display the temporal evolution of the SO$_2$ production efficiency throughout the 90 d simulation period (July – September, 2015). The multi-colored lines denote the production efficiencies across 50 air parcel trajectories initialized at the selected emission points. The thicker dark blue curve is the mean of these 50 trajectories. The values of τ represent the e-folding times in days for this mean curve. Panels (c) – (d) present the spatial variation of the production efficiency as a function of the pressure altitude and latitude. Panels (e) – (f) illustrate the spatial variation of the

production efficiency as a function of latitude and longitude. The green triangles indicate the approximate location of emission points 8 and 10, respectively.
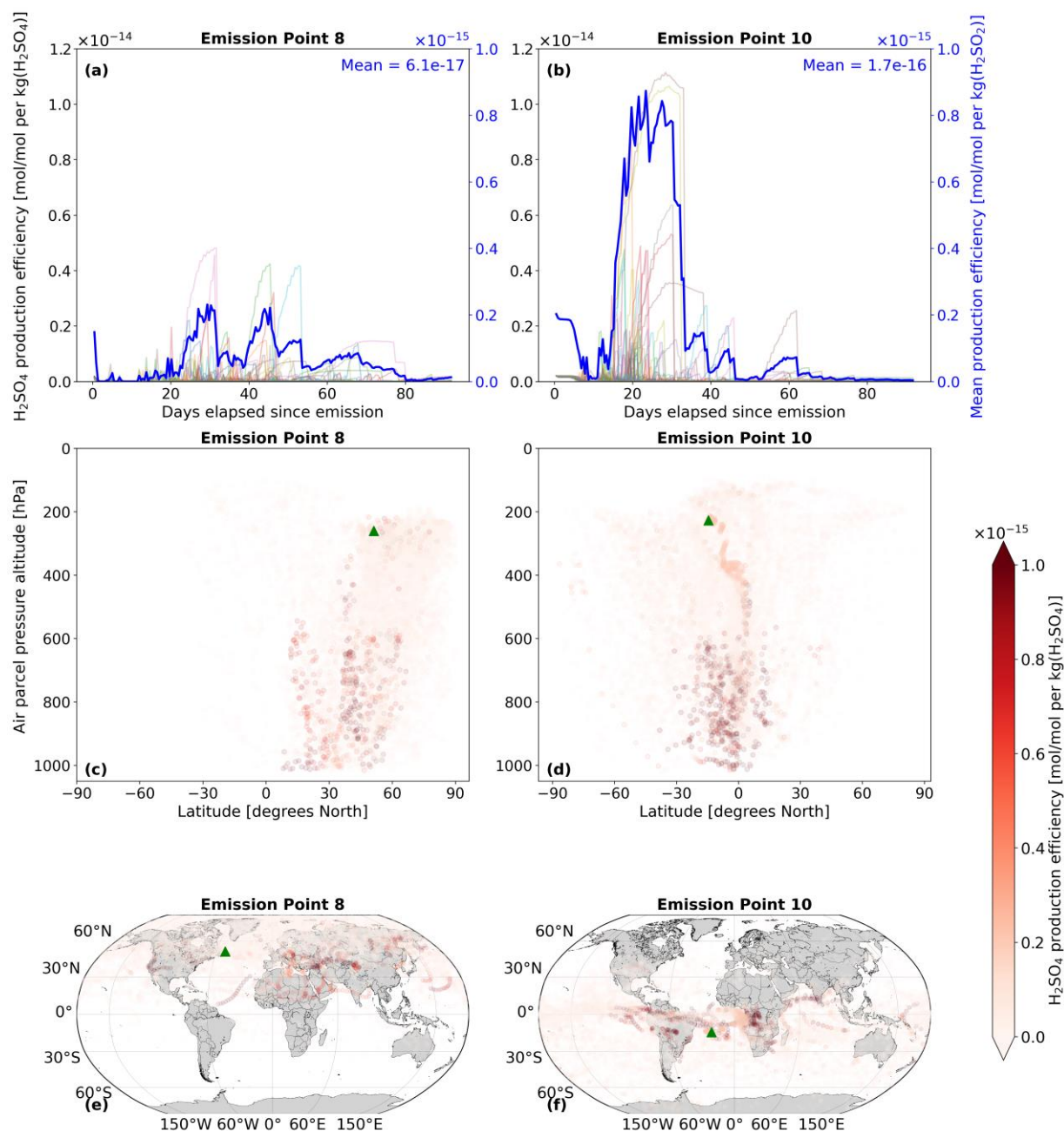

Figure 5 – The spatio-temporal variation of aviation-emitted sulfuric acid (H$_2$SO$_4$) scaled by the emission mass for emission points 8 and 10 (see Fig. 2). Panels (a) – (b) display the temporal evolution of the H$_2$SO$_4$ production efficiency throughout the 90 d simulation period (July – September, 2015). The multi-colored lines denote the production efficiencies across 50 air parcel trajectories initialized at the selected emission points. The thicker dark blue curve is the mean of these 50 trajectories. The

values of τ represent the e-folding times in days for this mean curve. Panels (c) – (d) present the spatial variation of the production efficiency as a function of the pressure altitude and latitude. Panels (e) – (f) present the spatial variation of the production efficiency as a function of latitude and longitude. The green triangles show the approximate location of emission points 8 and 10, respectively.

4.2 Analysis of secondary SO₄

The amount of sulfate attributable to aviation emissions of SO_2 and H_2SO_4 is calculated according to Eqs. 24 and 25. Figure 6 displays the spatio-temporal evolution of total sulfate, which is defined as the sum of SO_4 across the nine aerosol modes mentioned in Section 2.3: $SO_4 = \sum_{i=1}^{9} SO_{4,i}$. On average, SO_4 production at emission point 10 (Fig. 6b) is nearly three times larger than at emission point 8 (Fig. 6a). This large discrepancy is owed to the significantly larger amount of H_2SO_4 that results from point 10, which is converted to SO_4 via processes like nucleation and condensation. Both Figs. 6a and b further exemplify this, as SO_4 production is initiated when H_2SO_4 production is maximal, which occurs approximately at the 30 d mark for point 8 (Fig. 5a) and at the 2 d mark for point 10 (Fig. 5b). As there is an approximate 20 d delay from the emission of SO_2 and H_2SO_4 until the point during which SO_4 production occurs, sulfate aerosols can form in regions far from the initial emission points, as was seen with H_2SO_4 in Fig. 5. The sulfate lifetimes approximate to 67 d and 64 d for points 8 and 10, respectively. Unlike precursor species such as SO_2, secondary sulfate exhibits significantly longer atmospheric lifetimes—ranging from several days to weeks in the troposphere (Textor et al., 2006; Boucher, 2015; Toohey et al., 2025), and extending to several months or even years in the stratosphere (Myhre et al., 2013; Sun et al., 2024; Toohey et al., 2025). The lifetimes estimated in this study are comparable to the upper end of the tropospheric range, likely due to the consideration of pulse emissions in the upper troposphere–lower stratosphere (UTLS), and fall well within the expected stratospheric range. A more detailed discussion of these calculations is provided in Section 4.3.

Regarding the spatial distribution of SO_4, flying at point 8 on that specific day is likely to lead to the strongest sulfate production in the Northern Hemisphere, between the latitudes of 30° and 60° N (Fig. 6c). According to the corresponding horizontal distribution panel (Fig. 6e), several regions beyond the local North Atlantic emission area are affected, including parts of Europe and Asia. For point 10, a wider latitudinal band is impacted, with the largest impacts noted between 0° and 60° S (Fig. 6d). The Pacific region close to the Equator is likely to experience the largest SO_4 production (Fig. 6f). The Brewer-Dobson Circulation (BCD) patterns also impact the vertical transport of sulfate. As has been noted by Sun et al. (2023), particles injected in the Tropics at around the upper troposphere and lower stratosphere closer to the Equator will generally experience upwelling and may be transported higher into the stratosphere via the deep branch of the BCD. This phenomenon is clearly observed in Figs. 6c and d, where air parcels rise above the emission point (green triangle) and reach the highest altitudes near 0º N. The highest point reached for an emission starting at point 8 is 103 hPa (~16.1 km) and for point 10 is 94 hPa (~16.7 km). Additionally, as emission point 10 is closer to the Equator, more sulfate aerosols are lofted into the stratosphere, which enhances sulfate VMRs at higher altitudes and may even prolong the overall lifetime of aerosols if they remain in the stratosphere.
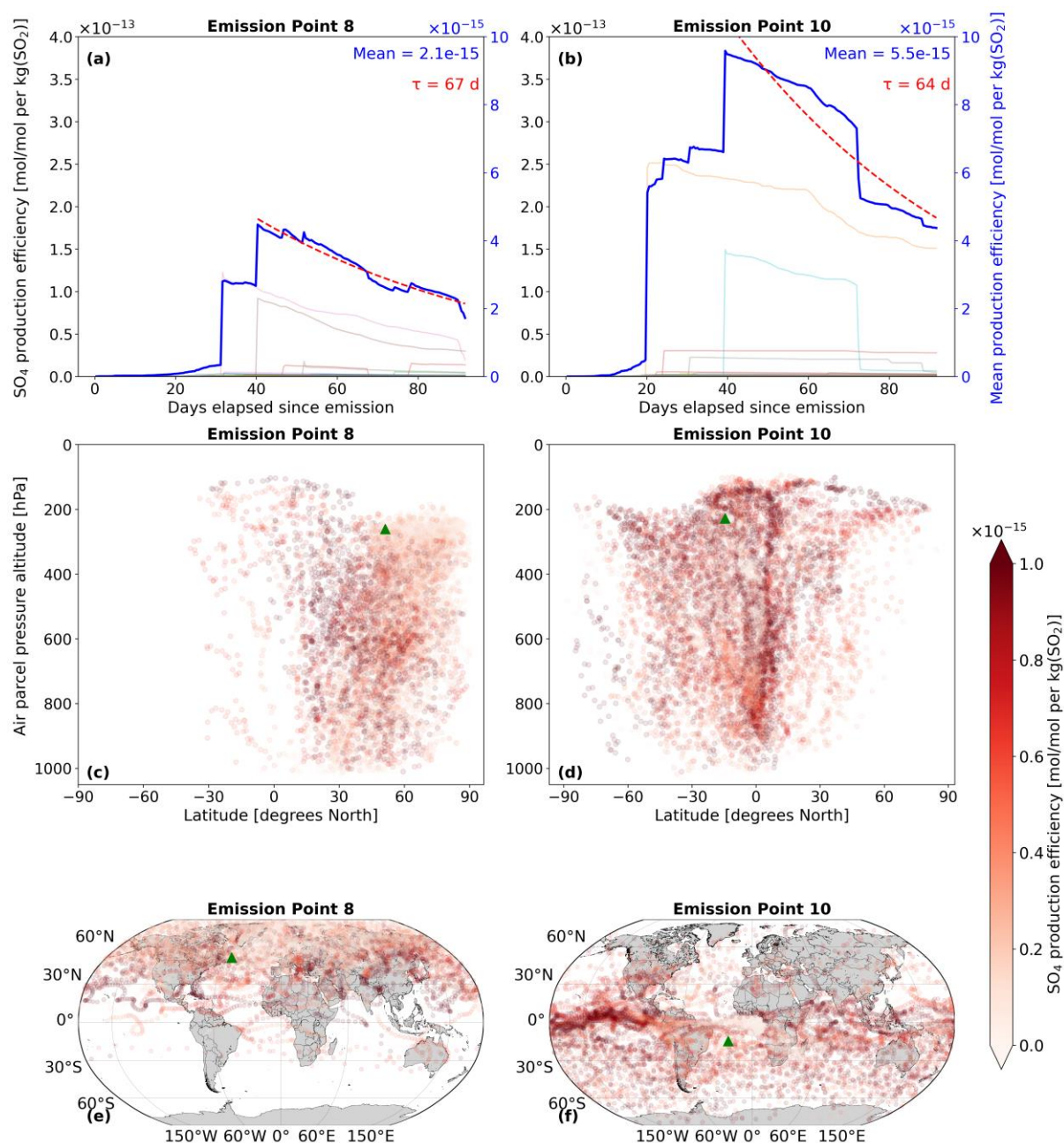
655

Figure 6 – The spatio-temporal variation of aviation-emitted total sulfate (sum of nine modes of SO$_4$) scaled by the emission mass for emission points 8 and 10 (see Fig. 2). Panels (a) – (b) display the temporal evolution of the SO$_4$ production efficiency throughout the 90 d simulation (July – September, 2015). The multi-colored lines denote the production efficiencies across 50 air parcel trajectories initialized at the selected emission points. The thicker dark blue curve is shown at the top right corner. 660 The e-folding time (τ) in days is shown in red and corresponding exponential lifetime fits are shown by the dashed red curves.

30

Panels (c) – (d) present the spatial variation of the production efficiency as a function of the pressure altitude and latitude. Panels (e) – (f) illustrates the spatial variation of the production efficiency as a function of latitude and longitude. The green triangles indicate the approximate location of emission points 8 and 10, respectively.

4.3 Seasonal effects

665   The production of sulfate aerosols from aviation exhibits a strong seasonal dependence as a result of variations in background chemistry and available solar radiation. Seasonal changes in the background water vapor and HO_x levels significantly influence the oxidation pathways that eventually convert SO_2 into SO_4. As with most tropospheric compounds, the SO_2 lifetime depends on the OH radical, which drives its gas-phase oxidation. OH is prevalent in warm and humid locations as its formation relies on the photodissociation of O_3 and subsequent reaction with H_2O (Riedel and Lassey, 2008). Figure 7a depicts the range of

670   SO_2 e-folding times for both seasons. The median e-folding time of 22 d in January (winter) is nearly 60% larger than the median of 14 d in July (summer), which is expected, given the increased solar radiation during summer that contributes to increased OH and faster SO_2 depletion rates. Consequently, this enhanced oxidation of SO_2 results in larger SO_4 production, as shown in Fig. 7b, where its median production efficiency is 144% larger in July compared to January. The summertime SO_2 median lifetime of 14 d is within the upper limit from past studies (von Glasow et al., 2009), indicating that our wintertime

675   estimate of 22 d is slightly overestimated. However, our range of SO_2 e-folding estimates agrees with results of the modeling study by Zhu et al. (2022) and with the observations from the 2022 Hunga Eruption from the Infrared Atmospheric Sounding Interferometer (IASI) satellite instrument that also estimated a similar upper limit lifetime of 21.4 d (Sellitto et al., 2024). This may be explained by our simplification of not accounting for the rapid aqueous-phase oxidation in the troposphere and scavenging processes, which act as significant SO_2 sinks. This explains the longer lifetimes of SO_2 in the stratosphere as wet

680   removal is less frequent, and HO_x species are much less abundant (Brodowsky et al., 2021). Due to the skewed nature of the distributions shown in Figure 7, a non-parametric statistical approach is more appropriate than parametric alternatives that assume normality. Therefore, the Mann-Whitney U test (Mann and Whitney, 1947) was applied to assess the statistical significance of seasonal differences. Based on this test, both the SO_2 lifetime (p-value $= 3.57 \times 10^{-4}$) and the SO_4 mean production efficiencies (p-value $= 6.83 \times 10^{-3}$) are found to be statistically significantly larger at the 95% confidence level

685   during the winter and summer seasons, respectively.

The lifetime of sulfate (Fig. 7c) has a median close to 2 months, with a value of around 62 d in January and 65 d in July. Unlike SO_2, the median SO_4 lifetimes are not statistically significantly different across summer and winter according to the same test statistic and confidence interval mentioned earlier (p-value $= 0.55$). It is worth noting, however, that the maximum SO_4 lifetime during winter of 123.5 d is almost 30% larger than the maximum in summer (96.7 d). This causes the mean SO_4 lifetime to be

690   larger in January (69 d) than in July (67 d). The sulfate time series plots for all 28 emissions points for the periods January – March, 2015 and July – September, 2015 from which the e-folding times in Fig. 7 were calculated are shown in Figs. S5 and S6 in the Supplement (Maruhashi et al., 2025b).
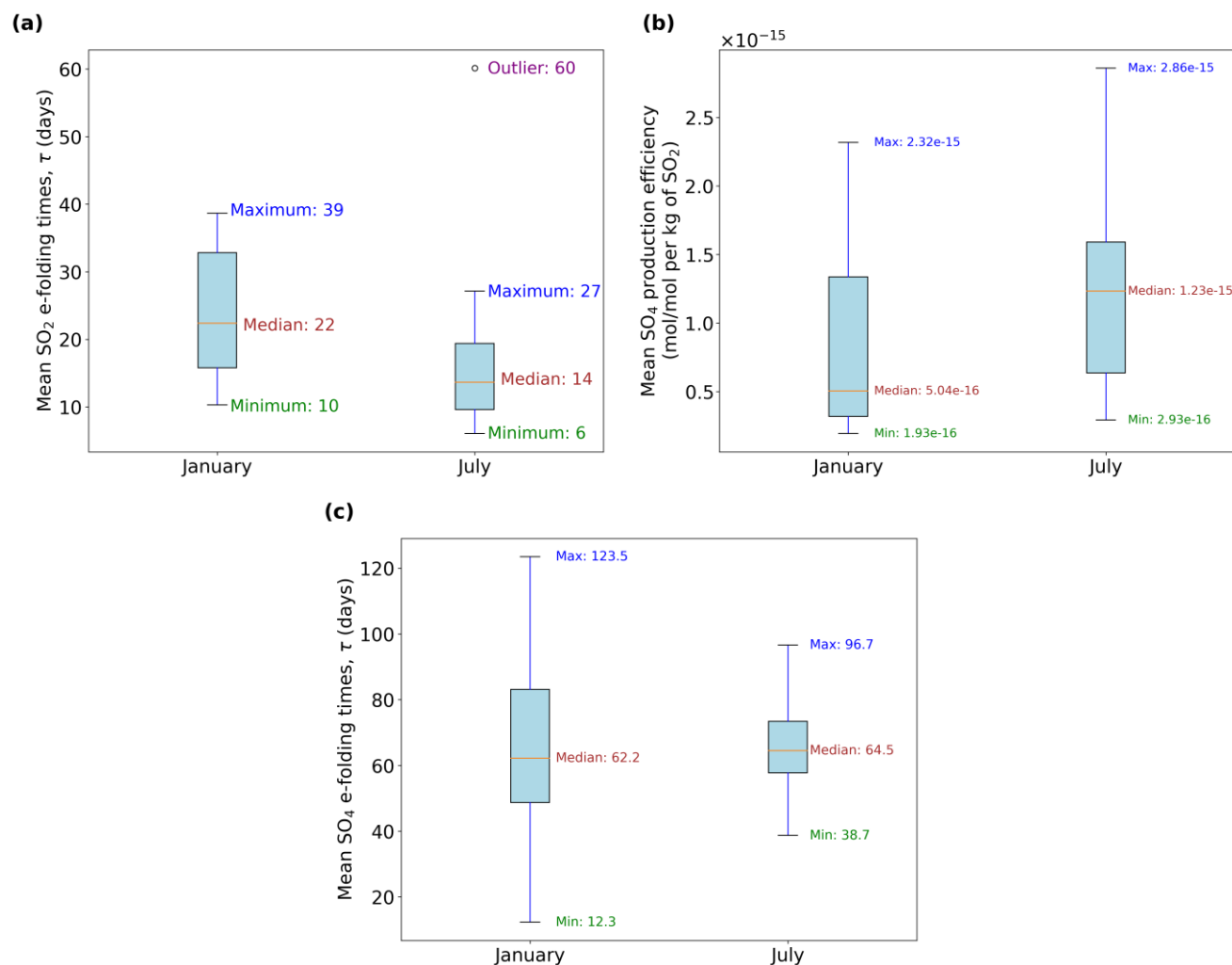
Figure 7 – Seasonal comparison of (a) sulfur dioxide (SO_2) e-folding times (e.g. same τ values in Fig. 4), (b) the three-month mean sulfate (SO_4) production efficiencies and (c) the sulfate e-folding times. Outliers in (b) are not shown for clarity. The horizontal axes describe the month of emission where January denotes the period January – March, 2015 and July denotes July – September, 2015.

Our range of calculated SO_4 lifetimes is consistent with output from another Lagrangian passive tracer pulse experiment from Toohey et al. (2025) that employs the FLEXPART model. In their analysis, stratospheric sulfate aerosol transport and lifetimes were analyzed in the context of volcanic SO_2 eruptions in the Northern Hemisphere. The altitudinal range of tracer injections in December and June that they considered varies from 13 – 25 km, where SO_4 aerosol lifetimes increased sharply with altitude. Since we emit SO_2 pulses at the UTLS that lead to sulfate maxima reaching around 100 hPa (~16 km) according to Figs. 6c and d, our results will also be comparable to theirs. According to their Fig. 4, sulfate aerosols at an altitude of 13 km between 40° and 60° N exhibit lifetimes ranging from 1.9 to 3.9 months during June (summer) and from 3.4 to 4 months during December (winter). Our Fig. 7c displays a median value of 62 d or ~2.1 months for January and ~2.2 months for July. Our

32

705 estimates are expectedly lower than their estimated range given our lower emission altitude. Furthermore, seeing as there is a portion of sulfate that reaches the stratosphere at around 16 km in altitude (e.g. Fig. 6), upper bound values in Fig. 7c such as 96.7 d (~3.2 months) in July and 123.5 d (~4.1 months) in January are also justified bearing in mind that, Sun et al. (2023), for instance, for an injection height of 16 km, found particle lifetimes throughout the year that range from 2.4 to 9.6 months, which are similar to both of our seasonal estimates from Fig. 7c. The lower stratospheric aerosol lifetime estimate by Sun et al. (2024)

710 estimated a smaller stratospheric aerosol lifetime of 4.8 months for a 65 hPa pressure altitude (~18.5 km). By contrast, particle lifetimes according to Toohey et al. (2025) for an injection height of 15 km were larger, ranging from 6.1 – 7.5 months. Differences between estimates from AIRTRAC and other models like LAGRANTO are, however, naturally expected as the latter does not consider aerosol microphysical processes like particle growth along trajectories.

4.4 Application to aerosol-cloud interactions

715 To demonstrate the capability of AIRTRAC v2.0 in predicting when aviation-attributable sulfate aerosols will likely interact with low-level liquid clouds, we incorporate satellite data from ESA's Climate Change Initiative (CCI) to identify the approximate locations of these clouds. More specifically, version 3 of the Advanced Very High Resolution Radiometer ante meridiem dataset (AVHRR-AMv3; Stengel et al., 2019) at monthly means is used, which covers the period from 1982 to 2016. This comprehensive dataset comprises 174 variables with a latitude-longitude grid resolution of 0.5°×0.5°. To pinpoint the

720 location of liquid clouds during the simulated periods in summer and winter, the liquid cloud fraction (LCF) and cloud top pressure (CTP) variables were analyzed.

Based on Fig. D1 from Appendix D, liquid clouds are predominantly found at CTPs below 800 hPa and are primarily concentrated in the Northern Atlantic and Southern Tropics, with a notably larger mean LCF observed during the summer months (July – September, 2015). During this period, liquid clouds are predominantly found between 0° - 30° S across all

725 longitudes. These horizontal liquid cloud distributions align with those reported by Stengel et al. (2020) for June 2014. Similarly, Lauer et al. (2007), using annual mean satellite data from the International Satellite Cloud Climatology Project (ISCCP) for the period 1983 – 2004, confirm a significant presence of low-level liquid clouds in the North Atlantic, North Pacific and South Atlantic regions.

Based on observations from this cloud satellite dataset, the region most likely to form low-level liquid clouds between July –

730 September, 2015 is marked with a blue rectangle in Fig. 8. When emissions occur near the Northern Mid-latitudes during summer (Fig. 8a), SO_4 may have an extended residence time near the cruise altitude, resulting in a slower downward transport to lower altitudes. The green median trajectory shows that air parcels following this path remain close to the emission pressure altitude of approximately 240 hPa for around 8 d before descending towards the surface, eventually reaching latitudes between 30° - 60° N. Although it is unlikely that SO_4 will reach the primary region with liquid clouds indicated in blue, it could still

735 interact with some clouds present in the North Atlantic (see Fig. D1). In contrast, emissions in the Southern Tropics (Fig. 8b) present an increased likelihood for interactions between aviation sulfate and liquid clouds in the Southern region.
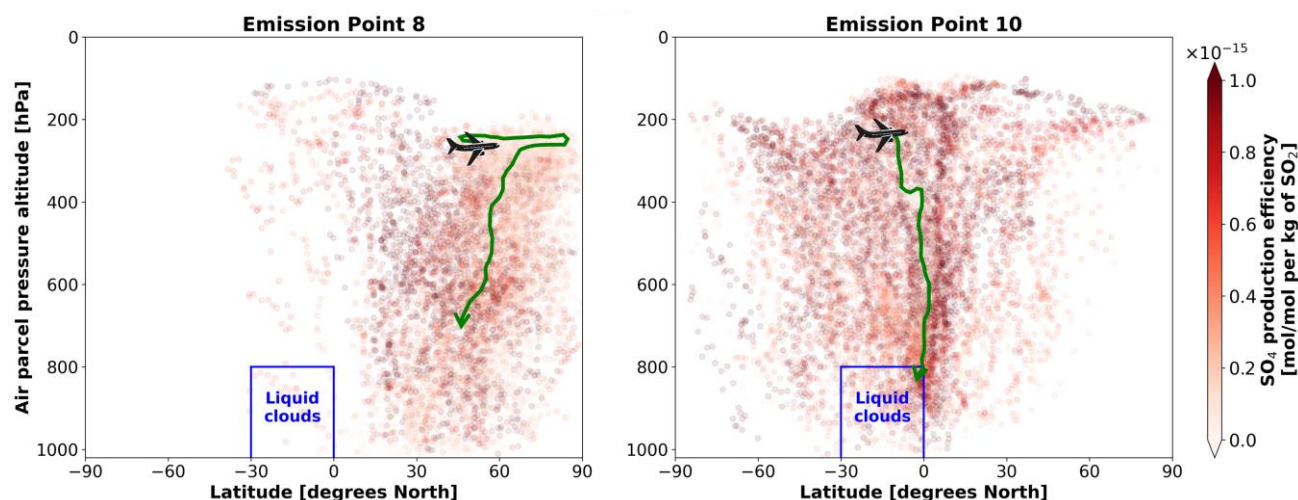

Figure 8 – Transport patterns for aviation-induced sulfate aerosols when SO_2 and H_2SO_4 are jointly emitted during July 2015 at (a) emission point 8 and at (b) emission point 9. The green curves represent the approximate median trajectories in each case. The aircraft icon indicates the approximate emission point. The blue region denotes the most probable location of lower-
740 level liquid clouds between July – September of 2015 according to the AVHRR-AMv3 dataset.

5 Evaluation of AIRTRAC v2.0

The conservation of sulfur species (closed mass budget) across the microphysical aerosol tendencies from MADE3 (growth, aging, coagulation, condensation and nucleation) that AIRTRAC v2.0 scales has been validated by Sharma et al. (2025). In general, the direct evaluation of tagging models using observational data is difficult, since observed concentrations of chemical
745 species are total quantities that emanate from various sources, both biogenic and anthropogenic, and disentangling these categories is challenging. Direct observational data for benchmarking are therefore unavailable. From a modeling perspective, evaluation is also challenging as many Lagrangian models are geared towards the stratospheric analysis of sulfate, as has been referred in earlier sections. However, the underlying components and submodels of AIRTRAC, like MADE3, have been extensively evaluated against a variety of experimental data (Kaiser et al., 2019). The lifetimes calculated by AIRTRAC v2.0
750 of precursor species like SO_2 and secondary SO_4 have also been shown to agree reasonably well in Sections 4.1 and 4.3 respectively with the output from other Lagrangian models applied to the study of stratospheric SO_4 from volcanic pulse emissions of SO_2 (Sun et al., 2023; Sun et al., 2024; Toohey et al., 2025). To evaluate the spatial distribution patterns of SO_4, a perturbation approach using a modeling setup similar to Righi et al. (2023) was applied to generate comparable simulation output. This simulation setup provides the most suitable basis for comparison due to its use of the same EMAC submodels and
755 emissions inventories (i.e. the same aviation SO_2 mass fluxes from CMIP6 for the year 2015), ensuring consistent background conditions. Additionally, for increased comparability, the CMIP6 aviation SO_2 emissions inventory applied in the perturbation

method has been modified to only consider mass fluxes at the same pressure level of 240 hPa as is shown in Fig. 2. It is important to reiterate that while the spatial patterns of SO$_4$ can be meaningfully compared, the magnitudes from the tagging and perturbation approaches are not expected to match, as each method addresses fundamentally different research questions (Clappier et al., 2017).

Figure 9 presents a comparison of the VMRs for SO$_4$ according to AIRTRAC v2.0 (Figs. 9a and c) and the perturbation approach (Figs. 9b and d) for both simulation periods. In AIRTRAC simulations, each of the 28 points (Fig. 2) is treated as an independent emission scenario, with no chemical interaction between any of the emissions considered (Maruhashi et al., 2024). Consequently, the values in Figs. 9a and c represent the total sulfate VMR across all 28 points and nine aerosol modes. However, a direct comparison of magnitudes is still challenging, as the perturbation approach inherently accounts for background feedbacks (i.e. local saturation effects and depletion of oxidizing species like OH) and non-linear interactions across emissions. Furthermore, the nature of emissions is also different: 15-minute pulses are applied for AIRTRAC, and sustained emissions across three months are assumed for the perturbation method. Although a direct comparison of magnitudes is difficult, both methods yield estimates of the same order of magnitude, i.e., 10^{-12} mol·mol^{-1}.

Both methods reveal fairly similar transport patterns, highlighting a production lag of sulfate relative to SO$_2$ emissions. This is evident in the larger VMRs that appear at altitudes below the original emission level of 240 hPa. Both approaches also agree that the tropical latitudinal band between 0° and 20° N near the surface is most strongly affected, in line with the results of Righi et al. (2023) for total aviation SO$_4$ in 2015 (see their Fig. S15b). While both methods capture enhanced VMRs near the emission altitude (~200 hPa), the perturbation approach predicts stronger sulfate concentrations in the upper northern latitudes (above 40° N; Figs. 9b,d) during both seasons, which is again consistent with Righi et al. (2023). AIRTRAC, by contrast, produces larger VMRs at this altitude closer to the northern tropics and mid-latitudes (Figs. 9a,c). This discrepancy may arise because the perturbation approach assumes a more widespread distribution of SO$_2$ given the sustained nature of its emissions, whereas AIRTRAC transports 15-min pulse emissions that are largest in magnitude over the mid-latitudes between 30° N and 40° N (e.g. emission points 4, 7, 15, and 18 in Fig. 2).

During winter, both approaches predict an enhancement of sulfate near the surface in the tropics (Fig. 9a and b). Close to a pressure altitude of 400 hPa, the perturbation approach estimates considerably smaller VMRs at the tropics. This could arise from feedbacks that mask effects (similar to chemical applications, see Grewe et al., 2012) or from the consideration that 10 out of 28 emission points are located below 30º N, even if individually they represent smaller emissions compared to, for instance, points 7 and 15 in Fig. 2. During summer, discrepancies between the approaches are larger, both near the surface and close to altitudes between 400 and 500 hPa (Figs. 9c and d). However, the region with the largest VMRs occurs below 600 hPa for both models and in the latitudinal band between 0º – 40º N. At the lowermost layers, AIRTRAC estimates negligible SO$_4$ VMRs, which could be due to the inherent limitations from the Lagrangian advection scheme itself, performed by the ATTILA submodel (Reithmeier and Sausen, 2002; Brinkop and Jöckel, 2019). As the grid-point equivalent VMRs are

calculated based on the average VMRs across all air parcels in a grid box, and the distribution of air parcels is not strictly
790 always representative of the pressure and air density distribution in the grid space, the mapping between Lagrangian space and
Eulerian frames will lead to differences in the calculation of VMRs of the air parcels (Grewe et al., 2014b). Additionally,
AIRTRAC estimates are also conditioned by the number of air parcels per grid box. According to Reithmeier and Sausen
(2002), the average number of air parcels near the surface for a T30 resolution is between 0.25 and 0.5 (see their Fig. 1). This
could also explain the much smaller VMRs near the surface in Figs. 9a and c.

795 Another source for the discrepancies between the spatial patterns in Fig. 9 could be the linear parameterization for the mixing
between air parcels by the LGTMIX submodel. The mixing intensity is controlled by two constants ($d_{trop} = 10^{-3}$; $d_{strat} = 10^{-6}$), one for each layer of the atmosphere. These were initially proposed by Collins et al. (1997) for gases and d_{strat} was
later changed to 5×10^{-4} by Reithmeier and Sausen (2002). Although short-lived species have been shown to be less sensitive
to these parameters (Reithmeier and Sausen, 2002), the suitability of these constants to model aerosol mixing within air parcels
800 has not been assessed. Further on the topic of linearization, AIRTRAC's linearly independent SO_4 contribution estimates for
each emission point are added to yield the total SO_4 (includes all nine modes) field in Fig. 9. In contrast to the perturbation
approach, this total neglects non-linear interaction effects between pulse emissions. For aviation NO_x–O_3 interactions, such
non-linearities have the capability to alter production efficiencies by up to 30 % (Maruhashi et al., 2024). Ultimately, however,
the sulfate spatial distributions between AIRTRAC and the perturbation approach largely agree that the lower altitudes between
805 the tropical to mid-latitudinal bands are the most affected. Despite methodological (tagging vs. perturbation) and emission
type (pulse vs. sustained) discrepancies, both approaches still yield estimates within the same order of magnitude.

(a) Tagging: January – March, 2015

(b) Perturbation: January – March, 2015

(c) Tagging: July – September, 2015
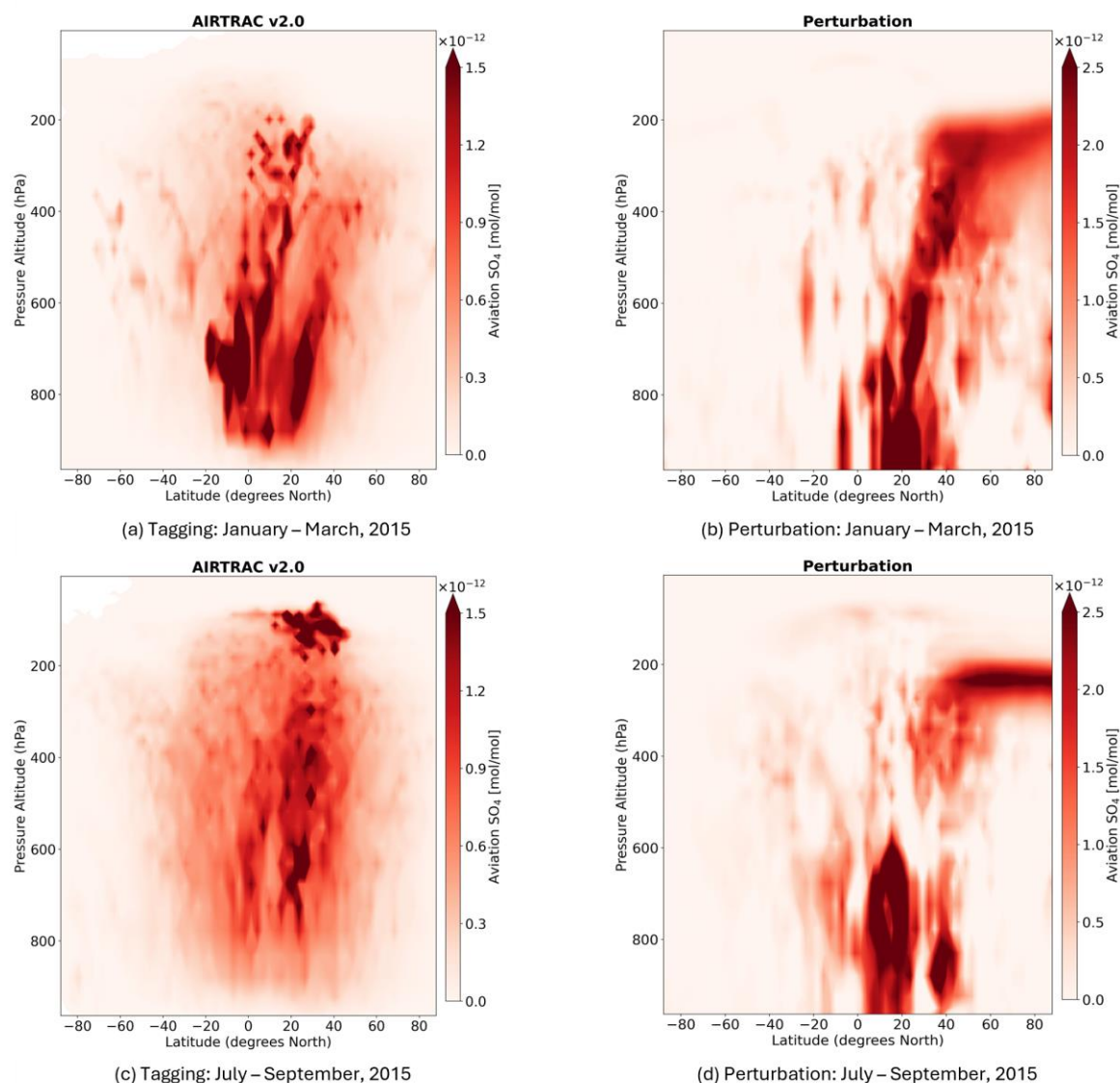
(d) Perturbation: July – September, 2015

Figure 9 – Comparison of AIRTRAC's tagging estimates with the MADE3-based perturbation approach using a modeling setup similar to Righi et al. (2023) for total SO_4 (sum of nine aerosol modes) during the period July – September, 2015. Estimates from AIRTRAC v2.0 (panels (a) and (c)) represent the sum across all 28 emission points of the total SO_4 at each of these points.

6 Discussion and conclusion

6.1 Model advances, limitations and future research

AIRTRAC v2.0 is the first Lagrangian sulfate tagging scheme within EMAC, providing the unique capability to track the long-range atmospheric evolution of aviation-emitted sulfur compounds. Starting from the emission of SO_2 and H_2SO_4 at subsonic cruise altitudes, the scheme follows their chemical transformation into SO_4 followed by the subsequent descent of these

37

aerosols into the lower troposphere, where interactions with liquid clouds may occur. By considering aerosol microphysical processes like nucleation, condensation, coagulation, aging and particle growth, AIRTRAC v2.0 can calculate the VMRs across nine sulfate aerosol modes. It is therefore a useful computational tool that may help predict which flight regions are most likely to lead to aerosol-cloud interactions. The quantification of these interactions and how they impact the Earth's

820   radiative budget (i.e. in terms of radiative forcing) is a key next step.

In terms of limitations, the linearization of the production and loss tendencies from MADE3 in AIRTRAC discards climate feedback effects that could be introduced by the SO_2 and H_2SO_4 emissions. This means that locally, for instance, the atmosphere's oxidative capacity will not vary with the magnitude of the pulse emissions, meaning that background OH levels will remain unaffected by the amount of SO_2 introduced by AIRTRAC. The implications of this linearization have been

825   analyzed in greater detail in the context of aviation NO_x-O_3 interactions by Maruhashi et al. (2024). As has been introduced in Section 5, the suitability of air parcel mixing parameters that were originally formulated mostly for gas-phase species still needs to be better understood. As smaller aerosols in the Aitken mode are likely to behave more closely to gaseous species when mixing and larger particles in the coarse mode will not mix as rapidly given their much larger momenta, the introduction of size-dependent mixing parameters should be considered.

830   Another limitation of AIRTRAC v2.0 is that it cannot track sulfate particles that have been scavenged and later re-evaporated back into the atmosphere, which may lead to underestimations of aerosol mixing ratios. Another factor potentially contributing again to the underestimation of sulfate is the exclusion of its aqueous-phase production pathway via SO_2 oxidation by H_2O_2, due to the computational limitation discussed by Tost et al. (2006). This not only has implications for the amount of sulfate produced, but will also tend to overestimate SO_2 estimated lifetimes (Brodowsky et al., 2021). Longer SO_2 lifetimes may then

835   also lead to longer sulfate lifetimes. Excluding plume-scale processes can lead to an overestimation of around 15% of the aviation-induced sulfate particle number concentration, but has a negligible impact on sulfate mass when compared to an instant dispersion approach, which is adopted in AIRTRAC v2.0 (Sharma et al., 2025).

A few final considerations to further extend the capabilities of AIRTRAC v2.0 would be to firstly include the indirect impact of aviation NO_x emissions on sulfate via the production of OH by connecting its gas-phase capabilities (version 1.0) to its new

840   aerosol capabilities. AIRTRAC could then provide a more comprehensive assessment of climate effects from aviation NO_x effects, which will remain relevant even for drop-in sustainable aviation fuels and emerging hydrogen-powered aircraft (Tiwari et al., 2024). This could be contemplated by updating the tagging ratio of Eq. 11 based on the biomolecular reaction formulation of the tagging ratio, as was described earlier in Section 3.2:

$$\left. C_{SO_2} \right|^{avi} = \underbrace{C_{SO_2}(t=0)}_{\text{Emission}} - \underbrace{\frac{1}{2} \times \left(\frac{\left. C_{SO_2} \right|^{avi}}{\left. C_{SO_2} \right|^{avi} + \left. C_{SO_2} \right|^{rem}} + \frac{\left. C_{OH} \right|^{avi}}{\left. C_{OH} \right|^{avi} + \left. C_{OH} \right|^{rem}} \right)}_{\text{Revised tagging ratio}} \times \underbrace{\frac{M_{SO_2}}{M_{H_2SO_4}}}_{\text{Molar masses}} \times \underbrace{P_{H_2SO_4}}_{\text{Production rate}} \times \Delta t + \underbrace{R(C_{SO_2})}_{\text{Turbulence}} . \quad (Eq. 26)$$

845   Secondly, to model the influence of aviation-induced sulfate on the microphysical properties of liquid clouds (e.g. by estimating the aerosol activation into cloud condensation nuclei), it would be necessary to extend the tagging from AIRTRAC v2.0 to also include the aerosol particle number concentration, as this is a key quantity driving aerosol-cloud interactions.

Lastly, AIRTRAC has been previously used as the computational foundation for the climate change functions (CCFs), which associate a change in temperature resulting from a local emission (Grewe et al., 2014a). Thus far, only CCFs for the net NO_x

850   effect, H_2O and contrails have been formulated for a limited set of emission points in the Northern Trans-Atlantic (Frömming et al., 2021). By running AIRTRAC v2.0, we have generated a dataset to analyze the transport of aviation-induced SO_2, H_2SO_4 and nine aerosol modes containing SO_4. This dataset may later serve as the basis for the development of the first aerosol-cloud interaction CCFs, thereby furthering the possibility of applying them to climate-optimal routing (Sausen et al., 1994; Grewe et al., 2014a).

855   **6.2 Conclusion**

This paper presents the new functionalities and technical implementation of the AIRTRAC v2.0 submodel within the EMAC modeling framework. It applies a Lagrangian tagging approach to estimate the contributions of aviation-induced SO_2 and H_2SO_4 emissions to nine aerosol modes of atmospheric sulfate. To showcase AIRTRAC's capabilities in characterizing the transport patterns of aviation sulfur compounds, two three-month simulation scenarios (winter and summer) were performed

860   based on the CMIP6 emissions inventory. Furthermore, ESA satellite data were incorporated to demonstrate how AIRTRAC can predict where aviation-induced sulfate will reach lower-level liquid clouds.

The transport patterns of SO_2, H_2SO_4 and SO_4 are primarily driven by the atmospheric circulation, where trade winds and downdrafts from, e.g., subsidence events play a particularly important role. It was found, for instance, that SO_2 that is quickly transported to lower altitudes has a shorter atmospheric lifetime due to the locally larger background concentrations of OH,

865   which are responsible for oxidizing SO_2 as well as many other chemical species. For the same reason, SO_2 that is transported to lower altitudes early may lead to the largest sulfate production efficiency given the increased oxidative potential at lower tropospheric altitudes. This is consistent with past studies that have focused on NO_x (Rosanka et al., 2020). Additionally, the BCD is also influential in determining the amount of sulfate that is lofted into the stratosphere, where its lifetime is longer. For example, species emitted from points closer to the Equator may be transported higher through the upwelling of the BCD

870   in the tropical region, which according to our results can reach pressure altitudes above 100 hPa. This phenomenon was also observed in another Lagrangian modeling study (Sun et al., 2023).

Seasonal variations were also found to impact the lifetime of SO_2 and the production efficiency of SO_4. The median lifetime of SO_2 during winter (January – March, 2015) was approximately 22 d compared to 14 d during the summer (July – September, 2015). The production efficiencies of SO_4 also vary seasonally given the dependence of OH concentrations on solar radiation:

875   in summer, increased sunlight enhances OH production, thereby boosting SO_4 formation. Overall, there was a 40% reduction

of SO_2 lifetimes in summer relative to winter and the SO_4 production efficiency in summer was 144% larger, these differences were found to be statistically significant at a 95% confidence level. Although median sulfate lifetimes were found to be larger in summer by almost 4%, the maximum SO_4 lifetime during winter was approximately 30% larger than in summer. The differences in SO_4 lifetimes were not found to be statistically significant.

880 We have also provided a case study in which AIRTRAC v2.0 would be useful to predict if SO_2 emissions from cruise would be transported far enough to reach the lower levels of the atmosphere that are more prone to liquid cloud formation, as indicated by ESA satellite cloud data. A clear difference was found between two emission scenarios: emitting in the usual North Atlantic Flight Corridor is unlikely to lead to significant aerosol interactions with the predominant liquid cloud cover in the South Atlantic, whereas flying at typical subsonic cruise levels (~240 hPa) in the Tropics would lead to a greater likelihood of aerosol-
885 cloud interactions.

AIRTRAC v2.0 relies largely on the aerosol tendencies from the MADE3 submodel, which have been evaluated extensively against observations from satellites, in-situ aircraft measurement and ground-based station data. We have validated AIRTRAC v2.0 output itself, however, with a combination of other Lagrangian modeling studies and with our results from a perturbation-based modeling approach. For example, lifetime estimates of SO_2 and SO_4 have been compared with both modeling and
890 observational studies of sulfate formation from volcanic eruptions, which can likewise be represented as a pulse emission of SO_2 at an above-ground injection altitude, followed by the production of SO_4 and its transport into the stratosphere. Given that some of our sulfate emissions also reach the stratosphere at similar injection heights tested by these studies, we have used them as reference. Our median SO_2 lifetimes agree mostly well with these past estimates ranging between a couple of days to three weeks. Our median SO_4 lifetimes of 2.1 and 2.2 months in January and July, respectively, likewise agree with ranges provided
895 by available studies. To assess the spatial distribution patterns of SO_4 predicted by AIRTRAC v2.0, we performed additional perturbation simulations with a comparable setup. Results showed that both approaches are consistent in identifying a similar latitudinal band in which sulfate VMR maxima are found in the lower troposphere. The near-surface estimates differ the most, where such discrepancies are likely owed to the limitations of a Lagrangian approach in having fewer air parcels near the surface (~0.25 – 0.5 per grid box) compared to higher parts of the atmosphere, where around 12 – 24 times as many air parcels
900 can exist per grid box.

Overall, AIRTRAC v2.0 is a promising tool that estimates lifetimes of sulfur-based species that drive aerosol-cloud interactions. Additionally, it can map the spatial distribution patterns to predict the emission points that are more likely to lead to impacts on lower-level liquid clouds. It is also highly efficient, capable of calculating up to around 28 emission scenarios in a single simulation, depending on the characteristics of the high-performance cluster.

905

Appendix A – list of EMAC submodels applied

Table A1 – List of MESSy submodels that were used for the simulations in this study. A brief description of each one is provided along with a reference that can be consulted for further information.

Submodel	Function	Source
AEROPT	Calculates aerosol optical properties.	Dietmüller et al. (2016)
AIRSEA	Computes exchange of chemical species between atmosphere and ocean.	Pozzer et al. (2006)
AIRTRAC	Calculates the contribution of a NO_x or H_2O emission to the atmospheric composition along air parcel trajectories. With version 2.0, the influence of SO_2 and H_2SO_4 on SO_4 may be studied.	Supplement of Grewe et al. (2014a), This study
ATTILA	Transport scheme for Lagrangian tracers.	Brinkop and Jöckel (2019)
CLOUD	Calculates cloud microphysics.	Kuebbeler et al. (2014)
CLOUDOPT	Calculates cloud optical properties.	Dietmüller et al. (2016)
CONVECT	Calculates convection based on different parameterizations.	Tost et al. (2006)
CVTRANS	Calculates transport of tracers due to convection.	Tost (2019)
DDEP	Calculates the dry deposition of gases and aerosols.	Kerkweg et al. (2006a)
E5VDIFF	Vertical diffusion for the ECHAM5 GCM.	Supplement of Emmerichs et al. (2021)
JVAL	Calculation of photolysis rates.	Sander et al. (2014)
LGTMIX	Parameterization for Lagrangian air parcel mixing.	Brinkop and Jöckel (2019)
LNOX	Parameterization for lightning NO_x emissions.	Tost et al. (2007)
MADE3	Calculation of aerosol microphysical processes.	Kaiser et al. (2019), Beer et al. (2020)
MECCA	Calculates tropospheric and stratospheric chemistry.	Sander et al. (2019)
OFFEMIS	Converts offline prescribed gridded emission fluxes from inventories to grid-point and Lagrangian tracer tendencies.	Kerkweg et al. (2006b)
ONEMIS	Calculates parameterized emission fluxes online during the simulation, including mineral dust and sea salt for aerosol emissions, and dimethyl sulfide (DMS) and nitric oxide (NO) for gaseous emissions.	Kerkweg et al. (2006b)
ORBIT	Calculates parameters related to Earth's solar orbit.	Dietmüller et al. (2016)
OROGW	Parameterization for orographic wave drag.	Roeckner et al. (2003)
SCAV	Wet scavenging process for gases, aerosols and liquid-phase chemistry.	Tost et al. (2006)
SEDI	Calculates sedimentation of aerosols.	Kerkweg et al. (2006)
SURFACE	Calculates surface temperatures over land and ocean.	MESSy Submodels (2024)
TNUDGE	Newtonian relaxation of user-defined tracers towards prescribed fields.	Kerkweg et al. (2006)
TREXP	Defines emission point sources for tracers.	Jöckel et al. (2010)
TROPOP	Meteorological diagnostics, such as tropopause height and planetary boundary layer height.	MESSy Submodels (2024)

910

Appendix B – determination of SO₂ and H₂SO₄ emission locations

We provide, in Table B1, the coordinates of the 28 emission points in Fig. 2. These have been calculated by first identifying the pressure altitude for which the zonally averaged aviation SO_2 mass flux is the largest (Fig. B1). The distribution of latitude-longitude coordinates (Fig. B2) is obtained by selecting the maximum SO_2 fluxes from the 28 grid cells with the largest SO_2

915   flux contributions (Eq. B1). The EP_selector tool (see Maruhashi et al. (2025a) for the full code) has been coded in Python to systematically output the coordinates of these locations by computing flux contributions across all user-defined grid cells. For those with the largest SO_2 mass flux contributions, the coordinates of the maxima are recorded. As the EP_selector tool possesses several inputs like the latitudinal and longitudinal spacing for each grid cell, as well as the number of grid cells in which to search for the n largest values, it is necessary to select an appropriate combination for these parameters. Our chosen

920   combination is based on maximizing the total grid cells while ensuring that the total flux contribution is above 90%.

Table B1 – SO_2 and H_2SO_4 emission coordinates and amounts in kg. The contribution column is calculated according to Eq. B1 and represents the area-weighted mean mass flux of a grid cell. The altitude for all locations is 238.2 hPa.

| EP	Latitude [deg. North]	Longitude [deg. East]	Contribution	Emission [kg(SO₂)]	Emission [kg(H₂SO₄)]
1	22.25	-155.25	0.9%	9.48E+03	2.96E+02
2	44.25	-142.25	1.4%	1.26E+04	3.93E+02
3	61.25	-155.25	2.6%	1.50E+04	4.69E+02
4	36.25	-112.25	6.8%	5.92E+04	1.85E+03
5	50.25	-100.25	2.5%	1.41E+04	4.40E+02
6	29.25	-81.25	3.1%	3.33E+04	1.04E+03
7	42.25	-71.25	11.0%	9.58E+04	2.99E+03
8	51.25	-61.25	2.0%	1.17E+04	3.65E+02
9	-20.25	-44.25	0.9%	9.37E+03	2.93E+02
10	-9.25	-37.25	1.0%	1.10E+04	3.43E+02
11	20.25	-20.25	1.1%	1.15E+04	3.59E+02
12	48.25	-58.25	3.0%	2.59E+04	8.09E+02
13	53.25	-36.25	4.9%	2.80E+04	8.75E+02
14	29.25	-14.25	1.5%	1.57E+04	4.90E+02
15	48.25	5.75	9.7%	8.48E+04	2.65E+03
16	52.25	-3.25	5.5%	3.12E+04	9.76E+02
17	27.25	53.75	1.4%	1.53E+04	4.79E+02
18	44.25	20.75	6.4%	5.58E+04	1.74E+03
19	53.25	20.75	3.2%	1.82E+04	5.67E+02
20	16.25	98.75	2.6%	2.78E+04	8.67E+02
21	43.25	66.75	2.4%	2.06E+04	6.43E+02
22	69.25	66.75	1.9%	1.09E+04	3.42E+02
23	3.25	105.75	1.7%	1.89E+04	5.91E+02
24	27.25	123.75	3.5%	3.79E+04	1.18E+03
25	42.25	135.75	4.5%	3.94E+04	1.23E+03
26	56.25	121.75	1.2%	7.11E+03	2.22E+02
27	38.25	142.75	3.4%	2.96E+04	9.24E+02
28	51.25	160.75	2.3%	1.33E+04	4.14E+02
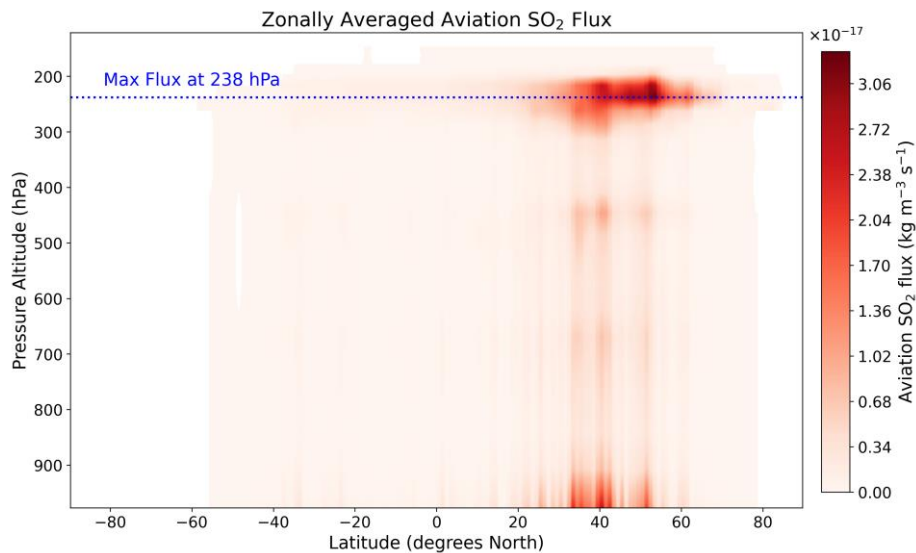
Figure B1 – Altitudinal variation of the zonally averaged aviation SO_2 mass flux [kg m^{-3} s^{-1}] from the CMIP6 aviation emissions inventory. The blue dotted line represents the pressure altitude of 238.2 hPa (~10.6 km) at which the maximum flux occurs.
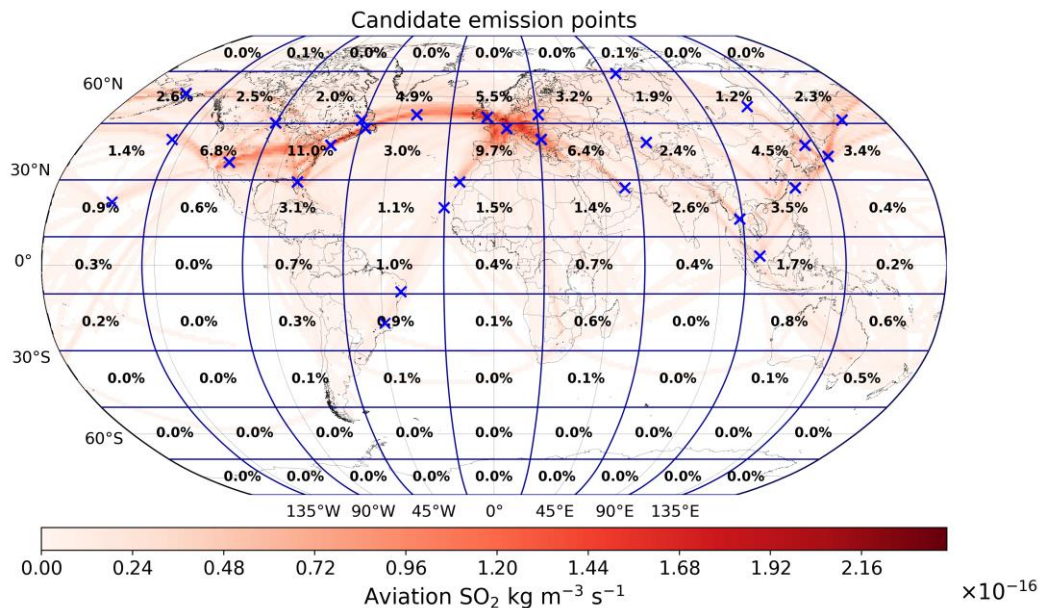
Figure B2 – Horizontal distribution of the 28 emission points (blue 'x' marks) determined by the EP_selector tool. The blue grid lines indicate the coarser user-defined mesh produced from spacings of 20º and 40º in the latitudinal and longitudinal directions respectively. The color bar depicts the spatial variation of aviation's SO_2 mass flux [kg m^{-3} s^{-1}] according to the CMIP6 emissions inventory. The percentages represent the contribution (Eq. B1) of a grid cell to the total SO_2 mass flux.

930 The SO$_2$ mass flux contribution of grid cell i, $\Gamma_i^{SO_2}$, is given by Eq. B1:

$$\Gamma_i^{SO_2} = \frac{A_i \times SO_{2,i}}{\sum_j^T A_j \times SO_{2,j}} \times 100\%. \tag{Eq. B1}$$

The total number of grid cells is given by $T = \frac{180°}{\Delta lat} \times \frac{360°}{\Delta lon}$, $SO_{2,i}$ is the total mass within a grid cell i and the area of a grid cell A_i is calculated according to Kelly and Šavrič (2021):

$$A_i = R_\oplus^2 \times \Delta lat \times \Delta lon \times \cos \overline{lat_i}. \tag{Eq. B2}$$

935 $\overline{lat_i}$ is the average between the bounding latitudes of grid cell i (i.e., its midpoint). The amount of SO$_2$ mass emitted in grid cell i, $SO_{2,i}$, is given by $SO_{2,i} = \Gamma_i^{SO_2} \times SO_{2,Total}$, where $SO_{2,Total}$ is approximately the total daily amount of SO$_2$ mass produced globally by aviation in 2015 according to CMIP6. The amount of H$_2$SO$_4$ is found by assuming that aviation's sulfur emissions are 98% SO$_2$ and 2% H$_2$SO$_4$. This means that the amount of H$_2$SO$_4$ mass emitted per grid cell, $H_2SO_{4,i}$, may be found in terms of $SO_{2,i}$, according to Eq. B3:

940
$$\frac{H_2SO_{4,i}}{H_2SO_{4,i} + \frac{M_{H_2SO_4}}{M_{SO_2}} \times SO_{2,i}} = 0.02 \Rightarrow H_2SO_{4,i} = \frac{0.02}{0.98} \times \frac{M_{H_2SO_4}}{M_{SO_2}} \times SO_{2,i}. \tag{Eq. B3}$$

The molecular masses of SO$_2$ and H$_2$SO$_4$ are denoted by M_{SO_2} and $M_{H_2SO_4}$ respectively.

Appendix C – tagging formulation (based on Grewe (2013)) of the coagulation process

We derive the tagging formulations for the remaining eight aerosol modes by applying Eq. 9 to Eq. 6. For each mode, we first rewrite Eq. 6 into a more compact form using the notations of Eqs. 16a and 16b and as a function of the soluble mass fraction
945 θ relative to water. Each derivation fulfils the tagging additivity requirement of Eq. 10. As a reminder, we note that $x_i = x_i^{avi} + x_i^{rem}$ and $C_p = C_{NH_4,p} + C_{NO_3,p} + C_{Na,p} + C_{Cl,p} + C_{POM,p} + C_{BC,p} + C_{DU,p} + C_{H_2O,p}$.

Aitken mixed (km) mode:

$$\left.\frac{\partial x_2}{\partial t}\right|_{coag} = F_2(\mathbf{x}) = \begin{cases} 0; \theta = 1 \text{ (Soluble)} \\ A\frac{x_1}{x_1 + C_1} - B\frac{x_2}{x_2 + C_2} + C\frac{x_3}{x_3 + C_3}; \theta \epsilon [0.1,1[\text{ (Mixed)} \\ -B'\frac{x_2}{x_2 + C_2}; \theta \epsilon [0,0.1[\text{ (Insoluble)} \end{cases} \tag{Eq. C1}$$

950 Here, the terms A, B, B′ and C are defined as:

$$A = \rho_1 \frac{\pi}{6} [f_{1,2} + f_{1,3}],$$

$$B = \rho_2 \frac{\pi}{6} [f_{2,4} + f_{2,5} + f_{2,6} + f_{2,7} + f_{2,8}],$$

$$B' = \rho_2 \frac{\pi}{6} [f_{2,3} + f_{2,6} + f_{2,9}],$$

$$C = \rho_3 \frac{\pi}{6} f'_{2,3}.$$

955 Aviation's contribution is then given by:

$$\left. \frac{\partial x_2^{avi}}{\partial t} \right|_{coag} = \begin{cases} 0; \theta = 1 \text{ (Soluble)} \\ F_2(\mathbf{x}) \dfrac{AC_1 \dfrac{x_1^{avi}}{(x_1 + C_1)^2} - BC_2 \dfrac{x_2^{avi}}{(x_2 + C_2)^2} + CC_3 \dfrac{x_3^{avi}}{(x_3 + C_3)^2}}{AC_1 \dfrac{x_1}{(x_1 + C_1)^2} - BC_2 \dfrac{x_2}{(x_2 + C_2)^2} + CC_3 \dfrac{x_3}{(x_3 + C_3)^2}}; \theta \epsilon [0.1,1[\text{ (Mixed)} \\ F_2(\mathbf{x}) \dfrac{x_2^{avi}}{x_2}; \theta \epsilon [0,0.1[\text{ (Insoluble)}. \end{cases} \quad \text{(Eq. C2)}$$

It is interesting to note that when $\theta = 1$ in Eq. C1, the coagulation tendency is zero as there is no collision event that produces a final particle in the soluble state when one of the colliding particles is in the km mode. This is consistent with Table 2 of Kaiser et al. (2014) in which all collision events are specified.

960 Aitken insoluble (ki) mode:

$$\left. \frac{\partial x_3}{\partial t} \right|_{coag} = F_3(\mathbf{x}) = \begin{cases} 0; \theta = 1 \text{ (Soluble)} \\ -C \dfrac{x_3}{x_3 + C_3}; \theta \epsilon [0.1,1[\text{ (Mixed)} \\ A' \dfrac{x_1}{x_1 + C_1} + B' \dfrac{x_2}{x_2 + C_2} - C' \dfrac{x_3}{x_3 + C_3} + D' \dfrac{x_4}{x_4 + C_4} + E' \dfrac{x_5}{x_5 + C_5}; \theta \epsilon [0,0.1[\text{ (Insoluble)}. \end{cases} \quad \text{(Eq. C3)}$$

Here, the terms A, A′, B′, C′, D′ and E′ are defined as:

$$C = \rho_3 \frac{\pi}{6} [f'_{1,3} + f'_{2,3} + f_{3,4} + f_{3,5} + f_{3,7} + f_{3,8}],$$

$$A' = \rho_1 \frac{\pi}{6} f_{1,3},$$

965

$$B' = \rho_2 \frac{\pi}{6} f_{2,3},$$

$$C' = \rho_3 \frac{\pi}{6} [f_{3,6} + f_{3,9}],$$

$$D' = \rho_4 \frac{\pi}{6} f'_{3,4},$$

$$E' = \rho_5 \frac{\pi}{6} f'_{3,5}.$$

Aviation's contribution is then given by:

970

$$\frac{\partial x_3^{avi}}{\partial t}\bigg|_{coag} = \begin{cases} 0; \theta = 1 \text{ (Soluble)} \\ F_3(\mathbf{x})\dfrac{x_3^{avi}}{x_3}; \theta\epsilon[0.1,1[\text{ (Mixing)} \\ F_3(\mathbf{x})\dfrac{A'C_1\frac{x_1^{avi}}{(x_1+C_1)^2} + B'C_2\frac{x_2^{avi}}{(x_2+C_2)^2} - C'C_3\frac{x_3^{avi}}{(x_3+C_3)^2} + D'C_4\frac{x_4^{avi}}{(x_4+C_4)^2} + E'C_5\frac{x_5^{avi}}{(x_5+C_5)^2}}{A'C_1\frac{x_1}{(x_1+C_1)^2} + B'C_2\frac{x_2}{(x_2+C_2)^2} - C'C_3\frac{x_3}{(x_3+C_3)^2} + D'C_4\frac{x_4}{(x_4+C_4)^2} + E'C_5\frac{x_5}{(x_5+C_5)^2}}; \theta\epsilon[0,0.1[\text{ (Insoluble)}. \end{cases}$$ (Eq. C4)

Accumulation soluble (as) mode:

$$\frac{\partial x_4}{\partial t}\bigg|_{coag} = F_4(\mathbf{x}) = \begin{cases} A\dfrac{x_1}{x_1+C_1} - D\dfrac{x_4}{x_4+C_4}; \theta = 1 \text{ (Soluble)} \\ -D'\dfrac{x_4}{x_4+C_4}; \theta\epsilon[0.1,1[\text{ (Mixed)} \\ -D''\dfrac{x_4}{x_4+C_4}; \theta\epsilon[0,0.1[\text{ (Insoluble)}. \end{cases}$$ (Eq. C5)

Here, the terms D' and D'' are defined as:

$$A = \rho_1 \frac{\pi}{6} f_{1,4},$$

975

$$D = \rho_4 \frac{\pi}{6} f_{4,7},$$

$$D' = \rho_4 \frac{\pi}{6} [f'_{2,4} + f'_{3,4} + f_{4,5} + f_{4,6} + f_{4,8} + f_{4,9}],$$

$$D'' = \rho_4 \frac{\pi}{6} [f'_{3,4} + f_{4,6} + f_{4,9}].$$

Aviation's contribution is given by:

$$\left.\frac{\partial x_4^{avi}}{\partial t}\right|_{coag} = \begin{cases} F_4(\mathbf{x}) \dfrac{AC_1 \dfrac{x_1^{avi}}{(x_1 + C_1)^2} - DC_4 \dfrac{x_4^{avi}}{(x_4 + C_4)^2}}{AC_1 \dfrac{x_1}{(x_1 + C_1)^2} - DC_4 \dfrac{x_4}{(x_4 + C_4)^2}}; \theta = 1 \text{ (Soluble)} \\[2em] F_4(\mathbf{x}) \dfrac{x_4^{avi}}{x_4}; \theta \epsilon [0.1,1[\text{ (Mixed)} \\[1.5em] F_4(\mathbf{x}) \dfrac{x_4^{avi}}{x_4}; \theta \epsilon [0,0.1[\text{ (Insoluble)}. \end{cases} \qquad (\text{Eq. C6})$$

980   Accumulation mixed (am) mode:

$$\left.\frac{\partial x_5}{\partial t}\right|_{coag} = F_5(\mathbf{x}) = \begin{cases} 0; \theta = 1 \text{ (Soluble)} \\[1em] A' \dfrac{x_1}{x_1 + C_1} + B' \dfrac{x_2}{x_2 + C_2} + C' \dfrac{x_3}{x_3 + C_3} + D' \dfrac{x_4}{x_4 + C_4} - E' \dfrac{x_5}{x_5 + C_5} + F' \dfrac{x_6}{x_6 + C_6}; \theta \epsilon [0.1,1[\text{ (Mixed)} \\[1em] -E'' \dfrac{x_5}{x_5 + C_5}; \theta \epsilon [0,0.1[\text{ (Insoluble)}. \end{cases} \text{(Eq. C7)}$$

Here, the terms A', B', C', D', E', F' and E'' are defined as:

$$A' = \rho_1 \frac{\pi}{6} [f_{1,5} + f_{1,6}],$$

$$B' = \rho_2 \frac{\pi}{6} [f_{2,4} + f_{2,5} + f_{2,6}],$$

985

$$C' = \rho_3 \frac{\pi}{6} [f_{3,4} + f_{3,5}],$$

$$D' = \rho_4 \frac{\pi}{6} [f'_{2,4} + f'_{3,4} + f_{4,5} + f_{4,6}],$$

$$E' = \rho_5 \frac{\pi}{6} [f_{5,7} + f_{5,8} + f_{5,9}],$$

$$E'' = \rho_5 \frac{\pi}{6} [f'_{3,5} + f_{5,6} + f_{5,9}],$$

$$F' = \rho_6 \frac{\pi}{6} [f'_{1,6} + f'_{2,6} + f'_{4,6} + f'_{5,6}].$$

990

Aviation's contribution is given by:

$$\left.\frac{\partial x_5^{avi}}{\partial t}\right|_{coag} = \begin{cases} 0; \theta = 1 \text{ (Soluble)} \\ F_5(\mathbf{x})\dfrac{n}{d}; \theta\epsilon[0.1,1[\text{ (Mixing)} \\ F_5(\mathbf{x})\dfrac{x_5^{avi}}{x_5}; \theta\epsilon[0,0.1[\text{ (Insoluble).} \end{cases} \qquad (\text{Eq. C8})$$

Here, n and d are abbreviations for the numerator and denominator:

$$n = A'C_1\frac{x_1^{avi}}{(x_1+C_1)^2} + B'C_2\frac{x_2^{avi}}{(x_2+C_2)^2} + C'C_3\frac{x_3^{avi}}{(x_3+C_3)^2} + D'C_4\frac{x_4^{avi}}{(x_4+C_4)^2} - E'C_5\frac{x_5^{avi}}{(x_5+C_5)^2} + F'C_6\frac{x_6^{avi}}{(x_6+C_6)^2},$$

995
$$d = A'C_1\frac{x_1}{(x_1+C_1)^2} + B'C_2\frac{x_2}{(x_2+C_2)^2} + C'C_3\frac{x_3}{(x_3+C_3)^2} + D'C_4\frac{x_4}{(x_4+C_4)^2} - E'C_5\frac{x_5}{(x_5+C_5)^2} + F'C_6\frac{x_6}{(x_6+C_6)^2}.$$

Accumulation insoluble (ai) mode:

$$\left.\frac{\partial x_6}{\partial t}\right|_{coag} = F_6(\mathbf{x}) = \begin{cases} 0; \theta = 1 \text{ (Soluble)} \\ -F\dfrac{x_6}{x_6+C_6}; \theta\epsilon[0.1,1[\text{ (Mixed)} \\ A'\dfrac{x_1}{x_1+C_1} + B'\dfrac{x_2}{x_2+C_2} + C'\dfrac{x_3}{x_3+C_3} + D'\dfrac{x_4}{x_4+C_4} + E'\dfrac{x_5}{x_5+C_5} + \cdots \\ \cdots - F'\dfrac{x_6}{x_6+C_6} + G'\dfrac{x_7}{x_7+C_7} + H'\dfrac{x_8}{x_8+C_8}; \theta\epsilon[0,0.1[\text{ (Insoluble).} \end{cases} \qquad (\text{Eq. C9})$$

Here, the terms A', B', C', D', E', F', F, G', and H':

$$A' = \rho_1\frac{\pi}{6}f_{1,6},$$

1000
$$B' = \rho_2\frac{\pi}{6}f_{2,6},$$

$$C' = \rho_3\frac{\pi}{6}f_{3,6},$$

$$D' = \rho_4\frac{\pi}{6}f_{4,6},$$

$$E' = \rho_5\frac{\pi}{6}f_{5,6},$$

48

$$F = \rho_6 \frac{\pi}{6}\left[f'_{1,6} + f_{2,6} + f'_{4,6} + f'_{5,6} + f_{6,7} + f_{6,8}\right],$$

$$F' = \rho_6 \frac{\pi}{6} f_{6,9},$$

$$G' = \rho_7 \frac{\pi}{6} f'_{6,7},$$

$$H' = \rho_8 \frac{\pi}{6} f'_{6,8}.$$

Aviation's contribution is given by:

$$\left.\frac{\partial x_6^{avi}}{\partial t}\right|_{coag} = \begin{cases} 0; \theta = 1 \text{ (Soluble)} \\ F_6(\mathbf{x}) \frac{x_6^{avi}}{x_6}; \theta \epsilon [0.1,1[\text{ (Mixing)} \\ F_6(\mathbf{x}) \frac{n}{d}; \theta \epsilon [0,0.1[\text{ (Insoluble)} \end{cases} \qquad \text{(Eq. C10)}$$

Here, n and d are abbreviations for the numerator and denominator:

$$n = A'C_1 \frac{x_1^{avi}}{(x_1 + C_1)^2} + B'C_2 \frac{x_2^{avi}}{(x_2 + C_2)^2} + C'C_3 \frac{x_3^{avi}}{(x_3 + C_3)^2} + D'C_4 \frac{x_4^{avi}}{(x_4 + C_4)^2} + E'C_5 \frac{x_5^{avi}}{(x_5 + C_5)^2} + \cdots$$

$$\cdots - F'C_6 \frac{x_6^{avi}}{(x_6 + C_6)^2} + G'C_7 \frac{x_7^{avi}}{(x_7 + C_7)^2} + H'C_8 \frac{x_8^{avi}}{(x_8 + C_8)^2}.$$

$$d = A'C_1 \frac{x_1}{(x_1 + C_1)^2} + B'C_2 \frac{x_2}{(x_2 + C_2)^2} + C'C_3 \frac{x_3}{(x_3 + C_3)^2} + D'C_4 \frac{x_4}{(x_4 + C_4)^2} + E'C_5 \frac{x_5}{(x_5 + C_5)^2} + \cdots$$

$$\cdots - F'C_6 \frac{x_6}{(x_6 + C_6)^2} + G'C_7 \frac{x_7}{(x_7 + C_7)^2} + H'C_8 \frac{x_8}{(x_8 + C_8)^2}.$$

Coarse soluble (cs) mode:

$$\left.\frac{\partial x_7}{\partial t}\right|_{coag} = F_7(\mathbf{x}) = \begin{cases} A \frac{x_1}{x_1 + C_1} + D \frac{x_4}{x_4 + C_4}; \theta = 1 \text{ (Soluble)} \\ -G' \frac{x_7}{x_7 + C_7}; \theta \epsilon [0.1,1[\text{ (Mixed)} \\ -G'' \frac{x_7}{x_7 + C_7}; \theta \epsilon [0,0.1[\text{ (Insoluble)}. \end{cases} \qquad \text{(Eq. C11)}$$

49

Here, the terms A, D, G′ and G″ are defined as:

$$A = \rho_1 \frac{\pi}{6} f_{1,7},$$

$$D = \rho_4 \frac{\pi}{6} f_{4,7},$$

$$G' = \rho_7 \frac{\pi}{6} \left[f'_{2,7} + f'_{3,7} + f'_{5,7} + f'_{6,7} + f_{7,8} + f_{7,9} \right],$$

$$G'' = \rho_7 \frac{\pi}{6} \left[f'_{6,7} + f_{7,9} \right].$$

Aviation's contribution is given by:

$$\left. \frac{\partial x_7^{avi}}{\partial t} \right|_{coag} = \begin{cases} F_7(\mathbf{x}) \dfrac{AC_1 \dfrac{x_1^{avi}}{(x_1 + C_1)^2} + DC_4 \dfrac{x_4^{avi}}{(x_4 + C_4)^2}}{AC_1 \dfrac{x_1}{(x_1 + C_1)^2} + DC_4 \dfrac{x_4}{(x_4 + C_4)^2}} ; \theta = 1 \text{ (Soluble)} \\ F_7(\mathbf{x}) \dfrac{x_7^{avi}}{x_7} ; \theta \epsilon [0.1,1[\text{ (Mixed)} \\ F_7(\mathbf{x}) \dfrac{x_7^{avi}}{x_7} ; \theta \epsilon [0,0.1[\text{ (Insoluble)}. \end{cases} \qquad \text{(Eq. C12)}$$

Coarse mixed (cm) mode:

$$\left. \frac{\partial x_8}{\partial t} \right|_{coag} = F_8(\mathbf{x}) = \begin{cases} 0 ; \theta = 1 \text{ (Soluble)} \\ A' \dfrac{x_1}{x_1 + C_1} + B' \dfrac{x_2}{x_2 + C_2} + C' \dfrac{x_3}{x_3 + C_3} + D' \dfrac{x_4}{x_4 + C_4} + E' \dfrac{x_5}{x_5 + C_5} + \cdots \\ \cdots + F' \dfrac{x_6}{x_6 + C_6} + G' \dfrac{x_7}{x_7 + C_7} + I' \dfrac{x_9}{x_9 + C_9} ; \theta \epsilon [0.1,1[\text{ (Mixed)} \\ -H'' \dfrac{x_8}{x_8 + C_8} ; \theta \epsilon [0,0.1[\text{ (Insoluble)}. \end{cases} \qquad \text{(Eq. C13)}$$

Here, the terms A′, B′, C′, D′, E′, F′, G′, H″ and I′ are defined as:

$$A' = \rho_1 \frac{\pi}{6} f_{1,8},$$

$$B' = \rho_2 \frac{\pi}{6} \left[f_{2,7} + f_{2,8} \right],$$

1030
$$C' = \rho_3 \frac{\pi}{6} \left[f_{3,7} + f_{3,8} \right],$$

$$D' = \rho_4 \frac{\pi}{6} \left[f_{4,8} + f_{4,9} \right],$$

$$E' = \rho_5 \frac{\pi}{6} \left[f_{5,7} + f_{5,8} + f_{5,9} \right],$$

$$F' = \rho_6 \frac{\pi}{6} \left[f_{6,7} + f_{6,8} \right],$$

$$G' = \rho_7 \frac{\pi}{6} \left[f'_{2,7} + f'_{3,7} + f'_{5,7} + f'_{6,7} + f_{7,8} + f_{7,9} \right],$$

1035
$$H'' = \rho_8 \frac{\pi}{6} \left[f'_{6,8} + f_{8,9} \right],$$

$$I' = \rho_9 \frac{\pi}{6} \left[f'_{4,9} + f'_{5,9} + f'_{7,9} + f'_{8,9} \right].$$

Aviation's contribution is given by:

$$\left. \frac{\partial x_8^{avi}}{\partial t} \right|_{coag} = \begin{cases} 0; \theta = 1 \text{ (Soluble)} \\ F_8(\mathbf{x}) \dfrac{n}{d}; \theta \epsilon [0.1,1[\text{ (Mixing)} \\ F_8(\mathbf{x}) \dfrac{x_8^{avi}}{x_8}; \theta \epsilon [0,0.1[\text{ (Insoluble)}. \end{cases} \qquad (\text{Eq. C14})$$

Here, n and d are abbreviations for the numerator and denominator:

1040
$$n = A'C_1 \frac{x_1^{avi}}{(x_1 + C_1)^2} + B'C_2 \frac{x_2^{avi}}{(x_2 + C_2)^2} + C'C_3 \frac{x_3^{avi}}{(x_3 + C_3)^2} + D'C_4 \frac{x_4^{avi}}{(x_4 + C_4)^2} + E'C_5 \frac{x_5^{avi}}{(x_5 + C_5)^2} + \cdots$$

$$\cdots + F'C_6 \frac{x_6^{avi}}{(x_6 + C_6)^2} + G'C_7 \frac{x_7^{avi}}{(x_7 + C_7)^2} + I'C_9 \frac{x_9^{avi}}{(x_9 + C_9)^2}.$$

$$d = A'C_1 \frac{x_1}{(x_1 + C_1)^2} + B'C_2 \frac{x_2}{(x_2 + C_2)^2} + C'C_3 \frac{x_3}{(x_3 + C_3)^2} + D'C_4 \frac{x_4}{(x_4 + C_4)^2} + E'C_5 \frac{x_5}{(x_5 + C_5)^2} + \cdots$$

$$\cdots + F'C_6 \frac{x_6}{(x_6 + C_6)^2} + G'C_7 \frac{x_7}{(x_7 + C_7)^2} + I'C_9 \frac{x_9}{(x_9 + C_9)^2}.$$

1045   Coarse insoluble (ci) mode:

$$\frac{\partial x_9}{\partial t}\Big|_{coag} = F_9(\mathbf{x}) = \begin{cases} 0; \theta = 1 \text{ (Soluble)} \\ -I' \dfrac{x_9}{x_9 + C_9}; \theta \epsilon [0.1,1[\text{ (Mixed)} \\ A'' \dfrac{x_1}{x_1 + C_1} + B'' \dfrac{x_2}{x_2 + C_2} + C'' \dfrac{x_3}{x_3 + C_3} + D'' \dfrac{x_4}{x_4 + C_4} + E'' \dfrac{x_5}{x_5 + C_5} + \cdots \\ \cdots + F'' \dfrac{x_6}{x_6 + C_6} + G'' \dfrac{x_7}{x_7 + C_7} + H'' \dfrac{x_8}{x_8 + C_8}; \theta \epsilon [0,0.1[\text{ (Insoluble)}. \end{cases} \qquad \text{(Eq. C15)}$$

Here, the terms A'', B'', C'', D'', E'', F'', G'', H'' and I' are defined as:

$$A'' = \rho_1 \frac{\pi}{6} f_{1,9},$$

$$B'' = \rho_2 \frac{\pi}{6} f_{2,9},$$

1050

$$C'' = \rho_3 \frac{\pi}{6} f_{3,9},$$

$$D'' = \rho_4 \frac{\pi}{6} f_{4,9},$$

$$E'' = \rho_5 \frac{\pi}{6} f_{5,9},$$

$$F'' = \rho_6 \frac{\pi}{6} f_{6,9},$$

$$G'' = \rho_7 \frac{\pi}{6} f_{7,9},$$

1055

$$H'' = \rho_8 \frac{\pi}{6} f_{8,9},$$

$$I' = \rho_9 \frac{\pi}{6} \big[f'_{4,9} + f'_{5,9} + f'_{7,9} + f'_{8,9} \big].$$

1060 Aviation's contribution is given by:

$$\left.\frac{\partial x_9^{avi}}{\partial t}\right|_{coag} = \begin{cases} 0; \theta = 1 \text{ (Soluble)} \\ F_9(\mathbf{x}) \frac{x_9^{avi}}{x_9}; \theta \epsilon [0.1,1[\text{ (Mixed)} \\ F_9(\mathbf{x}) \frac{n}{d}; \theta \epsilon [0,0.1[\text{ (Insoluble)}. \end{cases} \qquad (\text{Eq. C16})$$

Here, n and d are abbreviations for the numerator and denominator:

$$n = A''C_1 \frac{x_1^{avi}}{(x_1 + C_1)^2} + B''C_2 \frac{x_2^{avi}}{(x_2 + C_2)^2} + C''C_3 \frac{x_3^{avi}}{(x_3 + C_3)^2} + D''C_4 \frac{x_4^{avi}}{(x_4 + C_4)^2} + E''C_5 \frac{x_5^{avi}}{(x_5 + C_5)^2} + \cdots$$

$$\cdots + F''C_6 \frac{x_6^{avi}}{(x_6 + C_6)^2} + G''C_7 \frac{x_7^{avi}}{(x_7 + C_7)^2} + H''C_8 \frac{x_8^{avi}}{(x_8 + C_8)^2}.$$

1065 $$d = A''C_1 \frac{x_1}{(x_1 + C_1)^2} + B''C_2 \frac{x_2}{(x_2 + C_2)^2} + C''C_3 \frac{x_3}{(x_3 + C_3)^2} + D''C_4 \frac{x_4}{(x_4 + C_4)^2} + E''C_5 \frac{x_5}{(x_5 + C_5)^2} + \cdots$$

$$\cdots + F''C_6 \frac{x_6}{(x_6 + C_6)^2} + G''C_7 \frac{x_7}{(x_7 + C_7)^2} + H''C_8 \frac{x_8}{(x_8 + C_8)^2}.$$

Appendix D – Location of liquid clouds according to satellite data

Figure D1 plots the liquid cloud fraction (LCF; proportion of a grid cell area that is covered by liquid clouds) and the cloud
1070 top pressure in hPa (CTP; pressure altitude of the uppermost region of a cloud) from the AVHRR-AMv3 satellite dataset for
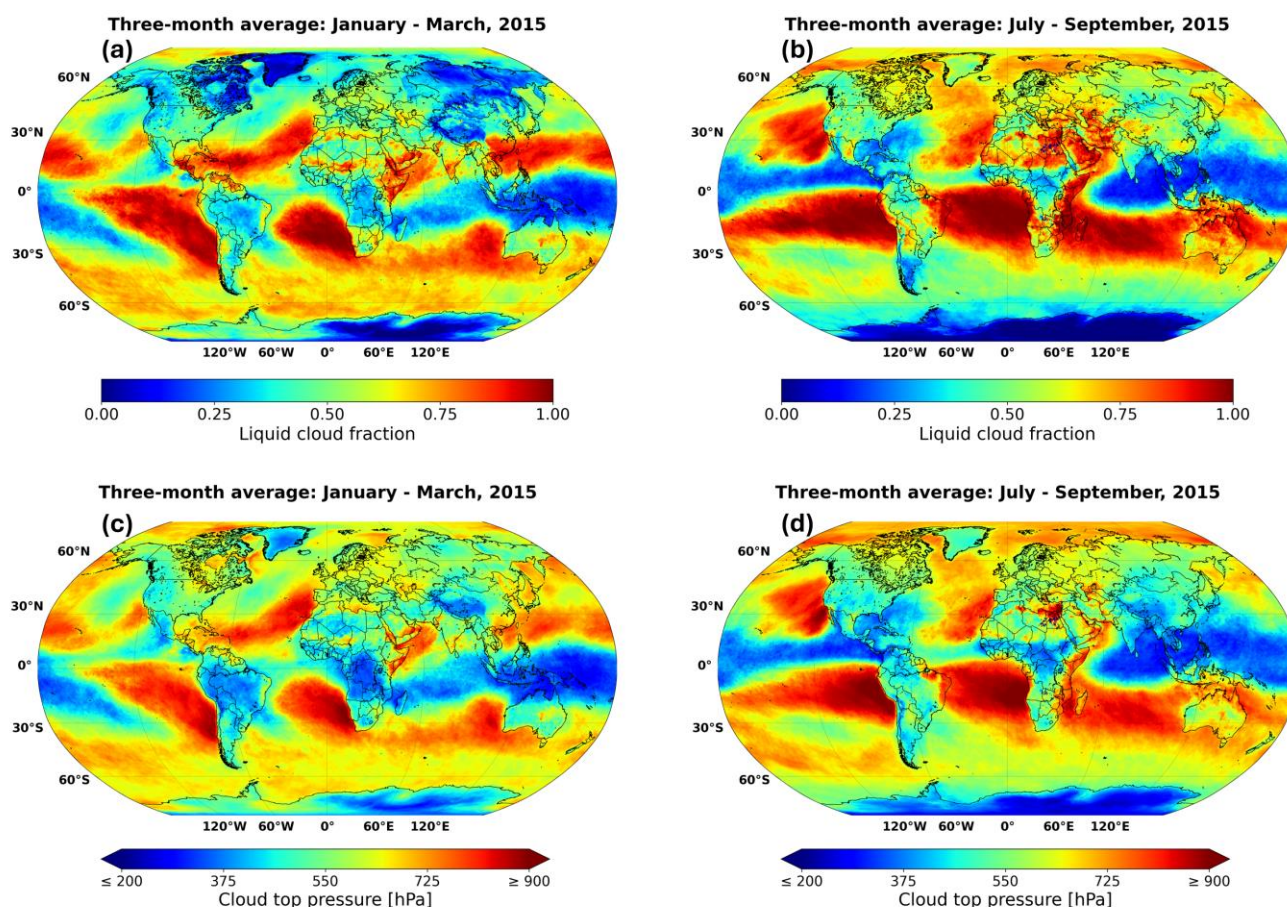both simulation periods: January – March, 2015 and July – September, 2015.

Figure D1 – Three-month means for the liquid cloud fractions (LCF) between (a) January – March of 2015 and (b) July –
September of 2015. Panels (c) and (d) represent the same time periods as (a) and (b) respectively, but for the three-month
means of the cloud top pressure (CTP) in hPa.

1075 **Acknowledgements**

Code and Data Availability

The Modular Earth Submodel System (MESSy) is continuously further developed and applied by a consortium of institutions. The usage of MESSy and access to the source code is licenced to all affiliates of institutions which are members of the MESSy Consortium. Institutions can become a member of the MESSy Consortium by signing the MESSy Memorandum of Understanding. More information can be found on the MESSy Consortium Website at http://www.messy-interface.org (MESSy Submodels, 2024). The code presented here has been based on MESSy version 2.55.2 and will be available in the next official release (version 2.56) at https://doi.org/10.5281/zenodo.8360186 (The MESSy Consortium, 2025a).

The specific code version for AIRTRAC v2.0 that was used to generate the data presented in this article may be accessed via the following repository: https://doi.org/10.5281/zenodo.15965933 (The MESSy Consortium, 2025b).

The EMAC simulation output data that was produced and analyzed in this paper will be made openly available via a 4TU Data Archive at https://doi.org/10.4121/8d2cdb5f-b652-41db-95a2-5345b4c1e77c (Maruhashi et al., 2025b). This link will be minted on acceptance. In the meantime, the same output dataset is freely accessible via the following link: https://data.4tu.nl/private_datasets/roLOC0VccLKAEsPosNgyhIFJrobb7JZqkZpUK8FWFQw (Maruhashi et al., 2025b).

Supplement

Supplementary figures and analyses regarding AIRTRAC v2.0 are also included in the same 4TU repository mentioned above.

Author Contributions

JM, MR, JH, VG and ID contributed to the conceptualization of the study. Coding of the new submodel was performed by JM, with support from MR, PJ, VG and ID. JM, MR, VG and ID performed the analysis of the simulation output. Input files and initial setup for running EMAC with the MADE3 submodel were provided by MR. Mass conservation of aerosol tendencies (budget analysis) was verified by MS. JM produced the manuscript with input from all authors.

Competing Interests

Volker Grewe and Patrick Jöckel are editors for GMD.

References

Ackermann, I. J., Hass, H., Memmesheimer, M., Ebel, A., Binkowski, F. S., and Shankar, U.: Modal aerosol dynamics model for Europe: development and first applications, Atmos. Environ., 32, 2981–2999, doi:10.1016/S1352-2310(98)00006-5, 1998.

Albrecht, B.: Aerosols, cloud microphysics, and fractional cloudiness, Science, 245, 1227–1230, DOI: 10.1126/science.245.4923.1227, 1989.

Aquila, V., Hendricks, J., Lauer, A., Riemer, N., Vogel, H., Baumgardner, D., Minikin, A., Petzold, A., Schwarz, J. P., Spackman, J. R., Weinzierl, B., Righi, M., and Dall'Amico, M.: MADE-in: a new aerosol microphysics submodel for global simulation of insoluble particles and their mixing state, Geosci. Model Dev., 4, 325–355, https://doi.org/10.5194/gmd-4-325-2011, 2011.

Barrie, L. A., Yi, Y., Leaitch, W. R., Lohmann, U., Kasibhatla, P., Roelofs, G. J., Wilson, J., McGovern, F., Benkovitz, C., Melieres, M. A., Law, K., Prospero, J., Kritz, M., Bergmann, D., Bridgeman, C., Chin, M., Christensen, J., Easter, R., Feichter, J., Land, C., Jeuken, A., Kjellstrom, E., Koch, D., and Rasch, P.: A comparison of large-scale atmospheric sulphate aerosol models (COSAM): overview and highlights, Tellus B, 53, 615–645, https://doi.org/10.1034/j.1600-0889.2001.530507.x, 2001.

Beer, C. G., Hendricks, J., Righi, M., Heinold, B., Tegen, I., Groß, S., Sauer, D., Walser, A., and Weinzierl, B.: Modelling mineral dust emissions and atmospheric dispersion with MADE3 in EMAC v2.54, Geosci. Model Dev., 13, 4287–4303, https://doi.org/10.5194/gmd-13-4287-2020, 2020.

Beirle, S., Hörmann, C., Penning de Vries, M., Dörner, S., Kern, C., and Wagner, T.: Estimating the volcanic emission rate and atmospheric lifetime of SO2 from space: a case study for Kīlauea volcano, Hawai`i, Atmos. Chem. Phys., 14, 8309–8322, https://doi.org/10.5194/acp-14-8309-2014, 2014.

Binkowski, F. S. and Roselle, S. J.: Models-3 community multiscale air quality (CMAQ) model aerosol component – 1. Model description, J. Geophys. Res.-Atmos., 108, 4183, doi:10.1029/2001JD001409, 2003.

Blanchard, C. L.: Methods for attributing ambient air pollutants to emission sources, Annu. Rev. Ener. Env., 24, 329–365, https://www.annualreviews.org/doi/10.1146/annurev.energy.24.1.329, 1999.

Boucher, O.: Atmospheric Aerosols Properties and Climate Impacts, Springer, https://doi.org/10.1007/978-94-017-9649-1, 2015.

Brasseur, G.P. and Jacob, D.J.: Chemical Processes in the Atmosphere. In: Modeling of Atmospheric Chemistry. Cambridge University Press; 54-83, https://doi.org/10.1017/9781316544754.004, 2017.

Brinkop, S. and Jöckel, P.: ATTILA 4.0: Lagrangian advective and convective transport of passive tracers within the ECHAM5/MESSy (2.53.0) chemistry–climate model, Geosci. Model Dev., 12, 1991–2008, https://doi.org/10.5194/gmd-12-1991-2019, 2019.

Brodowsky, C., Sukhodolov, T., Feinberg, A., Höpfner, M., Peter, T., Stenke, A., and Rozanov, E.: Modeling the Sulfate Aerosol Evolution After Recent Moderate Volcanic Activity, 2008–2012, J. Geophys. Res.-Atmos., 126, e2021JD035472, https://doi.org/10.1029/2021JD035472, 2021.

1140 Clappier, A., Belis, C. A., Pernigotti, D., and Thunis, P.: Source apportionment and sensitivity analysis: two methodologies with two different purposes, Geosci. Model Dev., 10, 4245–4256, https://doi.org/10.5194/gmd-10-4245-2017, 2017.

Collins, W.J., Stevenson, D.S., Johnson, C.E. and Derwent, R.G.: Tropospheric Ozone in a Global-Scale Three-Dimensional Lagrangian Model and Its Response to NOx Emission Controls, Journal of Atmospheric Chemistry, 26, 223–274, https://doi/10.1023/A:1005836531979, 1997.

1145 Dee, D. P., Uppala, S. M., Simmons, A. J., Berrisford, P., Poli, P., Kobayashi, S., Andrae, U., Balmaseda, M. A., Balsamo, G., Bauer, P., Bechtold, P., Beljaars, A. C. M., van de Berg, L., Bidlot, J., Bormann, N., Delsol, C., Dragani, R., Fuentes, M., Geer, A. J., Haimberger, L., Healy, S. B., Hersbach, H., Hólm, E. V., Isaksen, L., Kållberg, P., Köhler, M., Matricardi, M., McNally, A. P., Monge-Sanz, B. M., Morcrette, J.-J., Park, B.-K., Peubey, C., de Rosnay, P., Tavolato, C., Thépaut, J.-N., and Vitart, F.: The ERA-Interim reanalysis: configuration and performance of the data assimilation
1150 system, Q. J. Roy. Meteorol. Soc., 137, 553–597, https://doi.org/10.1002/qj.828, 2011.

Dietmüller, S., Jöckel, P., Tost, H., Kunze, M., Gellhorn, C., Brinkop, S., Frömming, C., Ponater, M., Steil, B., Lauer, A., and Hendricks, J.: A new radiation infrastructure for the Modular Earth Submodel System (MESSy, based on version 2.51), Geosci. Model Dev., 9, 2209–2222, https://doi.org/10.5194/gmd-9-2209-2016, 2016.

Emmerichs, T., Kerkweg, A., Ouwersloot, H., Fares, S., Mammarella, I., and Taraborrelli, D.: A revised dry deposition scheme
1155 for land–atmosphere exchange of trace gases in ECHAM/MESSy v2.54, Geosci. Model Dev., 14, 495–519, https://doi.org/10.5194/gmd-14-495-2021, 2021.

Farmer, D. K., Boedicker, E. K., and DeBolt, H. M.: Dry Deposition of Atmospheric Aerosols: Approaches, Observations, and Mechanisms, Ann. Rev. Phys. Chem., 72, 16.1–16.23, https://doi.org/10.1146/annurev-physchem-090519-034936, 2021.

1160 Feng, L., Smith, S. J., Braun, C., Crippa, M., Gidden, M. J., Hoesly, R., Klimont, Z., van Marle, M., van den Berg, M., and van der Werf, G. R.: The generation of gridded emissions data for CMIP6, Geosci. Model Dev., 13, 461–482, https://doi.org/10.5194/gmd-13-461-2020, 2020.

Fricko, O., Havlik, P., Rogelj, J., Klimont, Z., Gusti, M., Johnson, N., Kolp, P., Strubegger, M., Valin, H., Amann, M., Ermolieva, T., Forsell, N., Herrero, M., Heyes, C., Kindermann, G., Krey, V., McCollum, D. L., Obersteiner, M.,
1165 Pachauri, S., Rao, S., Schmid, E., Schoepp, W., and Riahi, K.: The marker quantification of the Shared Socioeconomic Pathway 2: A middle-of-the-road scenario for the 21st century, Global Environ. Chang., 42, 251–267, https://doi.org/10.1016/j.gloenvcha.2016.06.004, 2017.

Frömming, C., Ponater, M., Dahlmann, K., Grewe, V., Lee, D. S. and Sausen, R.: Aviation-induced radiative forcing and surface temperature change in dependency of the emission altitude, J. Geophys. Res., 117, D19104,
1170 https://doi.org/10.1029/2012JD018204, 2012.

Frömming, C., Grewe, V., Brinkop, S., Jöckel, P., Haslerud, A. S., Rosanka, S., van Manen, J. and Matthes, S.: Influence of weather situation on non-CO2 aviation climate effects: the REACT4C climate change functions, Atmos. Chem. Phys., 21, 9151–9172, https://doi.org/10.5194/acp-21-9151-2021, 2021.

Fuglestvedt, J., Berntsen, T., Eyring, V., Isaksen, I., Lee, D. S., and Sausen, R.: Shipping Emissions: From Cooling to Warming of Climate-and Reducing Impacts on Health, Environ. Sci. Technol., 43, 9057–9062, https://doi.org/10.1021/es901944r, 2009.

Gettelman, A. and Chen, C.: The Climate Impact of Aviation Aerosols, Geophys. Res. Lett., 40, 2785–2789, https://doi.org/10.1002/grl.50520, 2013.

Grewe, V., Tsati, E., and Hoor, P.: On the attribution of contributions of atmospheric trace gases to emissions in atmospheric model applications, Geosci. Model Dev., 3, 487–499, doi:10.5194/gmd3-487-2010, 2010.

Grewe, V., Dahlmann, K., Matthes, S., and Steinbrecht, W.: Attributing ozone to NOx emissions: Implications for climate mitigation measures, Atmos. Environ., 59, 102–107, https://doi.org/10.1016/j.atmosenv.2012.05.002, 2012.

Grewe, V.: A generalized tagging method, Geosci. Model Dev., 6, 247–253, https://doi.org/10.5194/gmd-6-247-2013, 2013.

Grewe, V., Frömming, C., Matthes, S., Brinkop, S., Ponater, M., Dietmüller, S., Jöckel, P., Garny, H., Tsati, E., Dahlmann, K., Søvde, O. A., Fuglestvedt, J., Berntsen, T. K., Shine, K. P., Irvine, E. A., Champougny, T., and Hullah, P.: Aircraft routing with minimal climate impact: the REACT4C climate cost function modelling approach (V1.0), Geosci. Model Dev., 7, 175–201, https://doi.org/10.5194/gmd-7-175-2014, 2014a.

Grewe, V., Brinkop, S., Jöckel, P., Shin, S., Reich, S., Yserentant, H., On the theory of mass conserving transformations for Lagrangian methods in 3D atmosphere-chemistry models, DOI: 10.1127/0941-2948/2014/0552, Met. Z. 23, 441-447, 2014b.

Haywood, J. M. and Shine, K. P.: The effect of anthropogenic sulfate and soot aerosol on the clear sky planetary radiation budget, Geophys. Res. Lett., 22(5), 603–606, https://doi.org/10.1029/95GL00075, 1995.

Haywood, J. and Boucher, O.: Estimates of the direct and indirect radiative forcing due to tropospheric aerosols: A review, Rev. Geophys., 38(4), 513–543, https://doi.org/10.1029/1999RG000078, 2000.

Hoor, P., Borken-Kleefeld, J., Caro, D., Dessens, O., Endresen, O., Gauss, M., Grewe, V., Hauglustaine, D., Isaksen, I. S. A., Jöckel, P., Lelieveld, J., Myhre, G., Meijer, E., Olivie, D., Prather, M., Schnadt Poberaj, C., Shine, K. P., Staehelin, J., Tang, Q., van Aardenne, J., van Velthoven, P., and Sausen, R.: The impact of traffic emissions on atmospheric ozone and OH: results from QUANTIFY, Atmos. Chem. Phys., 9, 3113–3136, https://doi.org/10.5194/acp-9-3113-2009, 2009.

Itahashi, S., Hayami, H., Yumimoto, K. and Uno, I.: Chinese province-scale source apportionments for sulfate aerosol in 2005 evaluated by the tagged tracer method, Environmental Pollution, 220, pp. 1366 – 1375, https://doi.org/10.1016/j.envpol.2016.10.098, 2017.

Jöckel, P., Kerkweg, A., Pozzer, A., Sander, R., Tost, H., Riede, H., Baumgaertner, A., Gromov, S., and Kern, B.: Development cycle 2 of the Modular Earth Submodel System (MESSy2), Geosci. Model Dev., 3, 717–752, https://doi.org/10.5194/gmd-3-717-2010, 2010.

Jurkat, T., Voigt, C., Arnold, F., Schlager, H., Kleffmann, J., Aufmhoff, H., Schäuble, D., Schaefer, M., and Schumann, U.: Measurements of HONO, NO, NO_y and SO_2 in aircraft exhaust plumes at cruise, Geophys. Res. Lett., 38, L10807, https://doi.org/10.1029/2011GL046884, 2011.

Kaiser, J. C., Hendricks, J., Righi, M., Riemer, N., Zaveri, R. A., Metzger, S., and Aquila, V.: The MESSy aerosol submodel MADE3 (v2.0b): description and a box model test, Geosci. Model Dev., 7, 1137–1157, https://doi.org/10.5194/gmd-7-1137-2014, 2014.

Kaiser, J. C., Hendricks, J., Righi, M., Jöckel, P., Tost, H., Kandler, K., Weinzierl, B., Sauer, D., Heimerl, K., Schwarz, J. P., Perring, A. E., and Popp, T.: Global aerosol modeling with MADE3 (v3.0) in EMAC (based on v2.53): model description and evaluation, Geosci. Model Dev., 12, 541–579, https://doi.org/10.5194/gmd-12-541-2019, 2019.

Kapadia, Z. Z., Spracklen, D. V., Arnold, S. R., Borman, D. J., Mann, G. W., Pringle, K. J., Monks, S. A., Reddington, C. L., Benduhn, F., Rap, A., Scott, C. E., Butt, E. W., and Yoshioka, M.: Impacts of aviation fuel sulfur content on climate and human health, Atmos. Chem. Phys., 16, 10521–10541, https://doi.org/10.5194/acp-16-10521-2016, 2016.

Kärcher, B., Möhler, O., DeMott, P. J., Pechtl, S., and Yu, F.: Insights into the role of soot aerosols in cirrus cloud formation, Atmos. Chem. Phys., 7, 4203–4227, https://doi.org/10.5194/acp-7-4203-2007, 2007.

Kelly, K. and Šavrič, B.: Area and volume computation of longitude–latitude grids and three-dimensional meshes, Transactions in GIS, 25, 6-24, https://doi.org/10.1111/tgis.12636, 2021.

Kerkweg, A., Buchholz, J., Ganzeveld, L., Pozzer, A., Tost, H., and Jöckel, P.: Technical Note: An implementation of the dry removal processes DRY DEPosition and SEDImentation in the Modular Earth Submodel System (MESSy), Atmos. Chem. Phys., 6, 4617–4632, https://doi.org/10.5194/acp-6-4617-2006, 2006a.

Kerkweg, A., Sander, R., Tost, H., and Jöckel, P.: Technical note: Implementation of prescribed (OFFLEM), calculated (ONLEM), and pseudo-emissions (TNUDGE) of chemical species in the Modular Earth Submodel System (MESSy), Atmos. Chem. Phys., 6, 3603–3609, https://doi.org/10.5194/acp-6-3603-2006, 2006b.

Khalizov, A.F., Zhang, R., Zhang, D., Xue, H., Pagels, J. and McMurry, P.H.: Formation of highly hygroscopic soot aerosols upon internal mixing with sulfuric acid vapor, Journal of Geophysical Research, 114, D05208, https://doi.org/10.1029/2008JD010595, 2009.

Khoder, M. I.: Atmospheric conversion of sulfur dioxide to particulate sulfate and nitrogen dioxide to particulate nitrate and gaseous nitric acid in an urban area, Chemosphere, 49, 675–684, https://doi.org/10.1016/S0045-6535(02)00391-0, 2002.

Kirkevåg, A., Iversen, T., and Dahlback, A.: On radiative effects of black carbon and sulphate aerosols, Atmos. Environ., 33, 2621–2635, ,1999.

Klöwer, M., Allen, M. R., Lee, D. S., Proud, S. R., Gallagher, L., and Skowron, A.: Quantifying aviation's contribution to global warming, Environ. Res. Lett., 16, 104027, https://doi.org/10.1088/1748-9326/ac286e, 2021.

Kristjánsson, J. E.: Studies of the aerosol indirect effect from sulfate and black carbon aerosols, J. Geophys. Res., 107, doi:10.1029/2001JD000 887, 2002.

1240 Kuebbeler, M., Lohmann, U., Hendricks, J., and Kärcher, B.: Dust ice nuclei effects on cirrus clouds, Atmos. Chem. Phys., 14, 3027–3046, https://doi.org/10.5194/acp-14-3027-2014, 2014.

Laaksonen, A., Pirjola, L., Kulmala, M., Wohlfrom, K.-H., Arnold, F., and Raes, F.: Upper tropospheric SO_2 conversion into sulphuric acid aerosols and cloud condensation nuclei, J. Geophys. Res., 105, 1459–1468, https://doi.org/10.1029/1999JD900933, 2000.

1245 Lamarque, J.-F., Bond, T. C., Eyring, V., Granier, C., Heil, A., Klimont, Z., Lee, D., Liousse, C., Mieville, A., Owen, B., Schultz, M. G., Shindell, D., Smith, S. J., Stehfest, E., Van Aardenne, J., Cooper, O. R., Kainuma, M., Mahowald, N., McConnell, J. R., Naik, V., Riahi, K., and van Vuuren, D. P.: Historical (1850–2000) gridded anthropogenic and biomass burning emissions of reactive gases and aerosols: methodology and application, Atmos. Chem. Phys., 10, 7017–7039, https://doi.org/10.5194/acp-10-7017-2010, 2010.

1250 Lauer, A., Hendricks, J., Ackermann, I., Schell, B., Hass, H., and Metzger, S.: Simulating aerosol microphysics with the ECHAM/MADE GCM – Part I: Model description and comparison with observations, Atmos. Chem. Phys., 5, 3251–3276, https://doi.org/10.5194/acp-5-3251-2005, 2005.

Lauer, A., Eyring, V., Hendricks, J., Jöckel, P., and Lohmann, U.: Global model simulations of the impact of ocean-going ships on aerosols, clouds, and the radiation budget, Atmos. Chem. Phys., 7, 5061–5079, https://doi.org/10.5194/acp-7-5061-2007, 2007.

1255 Lee, D.S., Pitari, G., Grewe, V., Gierens, K., Penner, J.E., Petzold, A., Prather, M.J., Schumann, U., Bais, A., Berntsen, T. and Iachetti, D.: Transport impacts on atmosphere and climate: aviation, Atmos. Env., 44, 37, pp. 4678 – 4734, https://doi.org/10.1016/j.atmosenv.2009.06.005, 2010.

Lee, D.S., Fahey, D.W., Skowron, A., Allen, M.R., Burkhardt, U., Chen, Q., Doherty, S.J., Freeman, S., Forster, P.M.,
1260 Fuglestvedt, J., Gettelman, A., De León, R.R., Lim, L.L., Lund, M.T., Millar, R.J., Owen, B., Penner, J.E., Pitari, G., Prather, M.J., Sausen, R. and Wilcox, L.J.: The contribution of global aviation to anthropogenic climate forcing for 2000 to 2018, Atmospheric Environment, Volume 244, 117834, ISSN 1352-2310, https://doi.org/10.1016/j.atmosenv.2020.117834, 2021.

Lohmann, U. and Feichter, J.: Impact of sulfate aerosols on albedo and lifetime of clouds: A sensitivity study with the ECHAM
1265 GCM, J. Geophys. Res., 102, 13 685–13 700, https://doi.org/10.1029/97JD00631, 1997.

Lohmann, U. and Feichter, J.: Global indirect aerosol effects: a review, Atmos. Chem. Phys., 5, 715–737, https://doi.org/10.5194/acp-5-715-2005, 2005.

Mann, H.B. and Whitney, D.R.: On a test of whether one of two random variables is stochastically larger than the other, The Annals of Mathematical Statistics, 18, pp. 50 – 60, https://www.jstor.org/stable/2236101, 1947.

1270   Martin, L.R. and Damschen, D.E.: Aqueous oxidation of sulfur dioxide by hydrogen peroxide at low pH, Atmos. Env. (1967), 15.9, pp. 1615 – 1621, https://doi.org/ 10.1016/0004-6981(81)90146-3, 1981.

Maruhashi, J., Grewe, V., Frömming, C., Jöckel, P., and Dedoussi, I. C.: Transport patterns of global aviation NO_x and their short-term O_3 radiative forcing – a machine learning approach, Atmos. Chem. Phys., 22, 14253–14282, https://doi.org/10.5194/acp-22-14253-2022, 2022.

1275   Maruhashi, J., Mertens, M., Grewe, V., and Dedoussi, I.C.: A multi-method assessment of the regional sensitivities between flight altitude and short-term O_3 climate warming from aircraft NO_x emissions, Environ. Res. Lett., 19(5), 054007, https://doi.org/10.1088/1748-9326/ad376a, 2024.

Maruhashi, J., Grewe, V. and Dedoussi, I.C.: Supporting dataset and code for the PhD dissertation "Characterizing the transport patterns and climate effects of aviation emissions using a novel Lagrangian tagging method". 4TU.ResearchData.
1280   dataset. https://doi.org/10.4121/79bcd360-04fc-4efc-a908-09874b9703c5, 2025a.

Maruhashi, J., Righi, M., Sharma, M., Hendricks, J., Jöckel, P., Grewe, V. and Dedoussi, I.C.: Supplementary Dataset and Figures of "AIRTRAC v2.0: a Lagrangian aerosol tagging submodel for the analysis of aviation SO_4 transport patterns". 4TU.ResearchData. dataset. https://doi.org/10.4121/8d2cdb5f-b652-41db-95a2-5345b4c1e77c, 2025b.

Matthes, S., Lim, L., Burkhardt, U., Dahlmann, K., Dietmüller, S., Grewe, V., Haslerud, A., Hendricks, J., Owen, B., Pitari,
1285   G., Righi, M., and Skowron, A.: Mitigation of Non-CO2 Aviation's Climate Impact by Changing Cruise Altitudes, Aerospace, 36, 1–20, https://doi.org/10.3390/aerospace8020036, 2021.

Mertens, M., Grewe, V., Rieger, V. S., and Jöckel, P.: Revisiting the contribution of land transport and shipping emissions to tropospheric ozone, Atmos. Chem. Phys., 18, 5567–5588, https://doi.org/10.5194/acp-18-5567-2018, 2018.

MESSy Submodels. The MESSy Submodels and Submodel licenses. https://messy-interface.org/messy/submodels/, 2024, last
1290   accessed: June 2024.

Mikkonen, S., Romakkaniemi, S., Smith, J. N., Korhonen, H., Petäjä, T., Plass-Duelmer, C., Boy, M., McMurry, P. H., Lehtinen, K. E. J., Joutsensaari, J., Hamed, A., Mauldin III, R. L., Birmili, W., Spindler, G., Arnold, F., Kulmala, M., and Laaksonen, A.: A statistical proxy for sulphuric acid concentration, Atmos. Chem. Phys., 11, 11319–11334, https://doi.org/10.5194/acp-11-11319-2011, 2011.

1295   Modini, R. L., Ristovski, Z. D., Johnson, G. R., He, C., Surawski, N., Morawska, L., Suni, T., and Kulmala, M.: New particle formation and growth at a remote, sub-tropical coastal location, Atmos. Chem. Phys., 9, 7607–7621, https://doi.org/10.5194/acp-9-7607-2009, 2009.

Myhre, G., Shindell, D., Bréon, F.-M., Collins, W., Fuglestvedt, J., Huang, J., Koch, D., Lamarque, J.-F., Lee, D., Mendoza, B., Nakajima, T., Robock, A., Stephens, G., Takemura, T., and Zhang, H.: Anthropogenic and natural radiative
1300   forcing, in: Climate Change 2013: The Physical Science Basis. Contribution of Working Group I to the Fifth Assessment Report of the Intergovernmental Panel on Climate Change, edited by: Stocker, T. F., Qin, D., Plattner, G.-K., Tignor, M., Allen, S. K., Boschung, J., Nauels, A., Xia, Y., Bex, V., and Midgley, P. M., Cambridge University

Press, Cambridge, United Kingdom and New York, NY, USA, 658–740, https://doi.org/10.1017/CBO9781107415324.018, 2013.

1305   Oppenheimer, C., Francis, P. and Stix, J.: Depletion rates of sulfur dioxide in tropospheric volcanic plumes, Geophys. Res. Lett., 25, 2671 – 2674, https://doi.org/10.1029/98GL01988, 1998.

Owen, B., Anet, J.G., Bertier, N., Christie, S., Cremaschi, M., Dellaert, S., Edebeli, J., Janicke, U., Kuenen, J., Lim, L. and Terrenoire, E.: Review: Particulate Matter Emissions from Aircraft, Atmosphere, 13, 1230, https://doi.org/10.3390/atmos13081230, 2022.

1310   Penner, J. E., Andreae, M., Annegarn, H., Barrie, L., Feichter, J., Hegg, D., Jayaraman, A., Leaitch, R., Murphy, D., Nganga, J., Pitari, G., et al.: Aerosols, their Direct and Indirect Effects, in: Climate Change 2001: The Scientific Basis, Contribution of Working Group I to the Third Assessment Report of the Intergovernmental Panel on Climate Change (IPCC), Chapter 5, edited by: Houghton, J. T., Ding, Y., Griggs, D. J., Noguer, M., Linden, P. J. v. d., and Xiaosu, D., Cambridge University Press, Cambridge, 289–348, 2001.

1315   Petzold, A., Gysel, M., Vancassel, X., Hitzenberger, R., Puxbaum, H., Vrochticky, S., Weingartner, E., Baltensperger, U., and Mirabel, P.: On the effects of organic matter and sulphur-containing compounds on the CCN activation of combustion particles, Atmos. Chem. Phys., 5, 3187–3203, https://doi.org/10.5194/acp-5-3187-2005, 2005.

Petzold, A. and Kärcher, B.: Aerosols in the Atmosphere. In: Schumann, U. (eds) Atmospheric Physics. Research Topics in Aerospace. Springer, Berlin, Heidelberg. https://doi.org/10.1007/978-3-642-30183-4_3, 2012.

1320   Pozzer, A., Jöckel, P., Sander, R., Williams, J., Ganzeveld, L., and Lelieveld, J.: Technical Note: The MESSy-submodel AIRSEA calculating the air-sea exchange of chemical species, Atmos. Chem. Phys., 6, 5435–5444, https://doi.org/10.5194/acp-6-5435-2006, 2006.

Quadros, F.D.A, Snellen, M., Sun, J. and Dedoussi, I.C.: Global Civil Aviation Emissions Estimates for 2017-2020 Using ADS-B Data, Journal of Aircraft, 59, pp. 1394 – 1405, https://doi.org/ 10.2514/1.C036763, 2022.

1325   Reithmeier, C. and Sausen, R.: ATTILA: Atmospheric Tracer Transport in a Lagrangian Model, Tellus B, 54, 278–299, 2002.

Riedel, K. and Lassey, K.: Detergent of the atmosphere, Water and Atmosphere, 16.2, https://niwa.co.nz/sites/default/files/import/attachments/detergent.pdf , 2008.

Riccio, A., Chianese, E., Agrillo, G., Esposito, C. and Tirimberio, G.: Source apportion of atmospheric particulate matter: a joint Eulerian/Lagrangian approach, Environmental Science and Pollution Research, 21, pp. 13160 – 13168,
1330   https://doi.org/ 10.1007/s11356-013-2367-5, 2014.

Righi, M., Hendricks, J., and Sausen, R.: The global impact of the transport sectors on atmospheric aerosol: simulations for year 2000 emissions, Atmos. Chem. Phys., 13, 9939–9970, https://doi.org/10.5194/acp-13-9939-2013, 2013.

Righi, M., Hendricks, J., and Brinkop, S.: The global impact of the transport sectors on the atmospheric aerosol and the resulting climate effects under the Shared Socioeconomic Pathways (SSPs), Earth Syst. Dynam., 14, 835–859,
1335   https://doi.org/10.5194/esd-14-835-2023, 2023.

Roeckner, E., Bäuml, G., Bonaventura, L., Brokopf, R., Esch, M., Giorgetta, M., Hagemann, S., Kirchner, I., Kornblueh, L., Manzini, E., Schlese, U., and Schulzweida, U.: The atmospheric general circulation model ECHAM 5. PART I: Model description, Report, Max-Planck-Institut für Meteorologie, 349, https://hdl.handle.net/21.11116/0000-0005-A14B-1, 2003.

1340 Roeckner, E., Brokopf, R., Esch, M., Giorgetta, M., Hagemann, S., Kornblueh, L., Manzini, E., Schlese, U., and Schulzweida, U.: Sensitivity of Simulated Climate to Horizontal and Vertical Resolution in the ECHAM5 Atmosphere Model, J. Climate, 19, 3771–3791, https://doi.org/10.1175/jcli3824.1, 2006.

Rosanka, S., Frömming, C., and Grewe, V.: The impact of weather patterns and related transport processes on aviation's contribution to ozone and methane concentrations from NOx emissions, Atmos. Chem. Phys., 20, 12347–12361,
1345 https://doi.org/10.5194/acp-20-12347-2020, 2020.

Sander, R., Kerkweg, A., Jockel, P., and Lelieveld, J.: Technical ¨Note: The new comprehensive atmospheric chemistry module MECCA, Atmos. Chem. Phys., 5, 445–450, https://doi.org/10.5194/acp-5-445-2005, 2005.

Sander, R., Jöckel, P., Kirner, O., Kunert, A. T., Landgraf, J., and Pozzer, A.: The photolysis module JVAL-14, compatible with the MESSy standard, and the JVal PreProcessor (JVPP), Geosci. Model Dev., 7, 2653–2662,
1350 https://doi.org/10.5194/gmd-7-2653-2014, 2014.

Sander, R., Baumgaertner, A., Cabrera-Perez, D., Frank, F., Gromov, S., Grooß, J.-U., Harder, H., Huijnen, V., Jöckel, P., Karydis, V. A., Niemeyer, K. E., Pozzer, A., Riede, H., Schultz, M. G., Taraborrelli, D., and Tauer, S.: The community atmospheric chemistry box model CAABA/MECCA-4.0, Geosci. Model Dev., 12, 1365–1385, https://doi.org/10.5194/gmd-12-1365-2019, 2019.

1355 Sausen, R., Nodorp, D., and Land, C.: Towards an optimal flight routing with respect to minimal environmental impact, in: Impact of Emissions from Aircraft and Spacecraft upon the Atmosphere, edited by: Schumann, U. and Wurzel, D., Procedings of an International Science Colloquium, Köln (Cologne), Germany, 18–20 April, ISSN 0939-298X, 473–478, 1994.

Sausen, R., Gierens, K., Eyring, V., Hendricks, J. and Righi, M.: Climate Impact of Transport. In: Schumann, U. (eds)
1360 Atmospheric Physics. Research Topics in Aerospace. Springer, Berlin, Heidelberg. https://doi.org/10.1007/978-3-642-30183-4_43, 2012.

Sellitto, P., Siddans, R., Belhadji, R., Carboni, E., Legras, B., Podglajen, A., Duchamp, C. and Kerridge, B.: Observing the SO2 and Sulfate Aerosol Plumes From the 2022 Hunga Eruption With the Infrared Atmospheric Sounding Interferometer (IASI), Geophys. Res. Lett., 51, e2023GL105565, https://doi.org/10.1029/2023GL105565, 2024.

1365 Sharma, M., Righi, M., Hendricks, J., Schmidt, A., Sauer, D., and Grewe, V.: A double-box model for aircraft exhaust plumes based on the MADE3 aerosol microphysics (MADE3 v4.0), EGUsphere [preprint], https://doi.org/10.5194/egusphere-2025-1137, 2025.

Sheng, F., Jingjing, L., Yu., C., Fu-Ming, T., Xuemei, D., and Jing-yao, L.: Theoretical study of the oxidation reactions of sulfurous acid/sulfite with ozone to produce sulfuric acid/sulfate with atmospheric implications, RSC Advances, 8, 7988–7996, https://doi.org/10.1039/C8RA00411K, 2018.

1370

Shostak, S., Kim, K., Horbatenko, Y., and Choi, C. H.: Sulfuric Acid Formation via H2SO3 Oxidation by H2O2 in the Atmosphere, J. Phys. Chem. A, 123, 8385–8390, https://doi.org/10.1021/acs.jpca.9b05444, 2019.

Søvde, O.A., Matthes, S., Skowron, A., Iachetti, D., Lim, L.L., Owen, B., Hodnebrog, Ø., Di Genova, G., Pitari, G. and Lee, D.S.: Aircraft emission mitigation by changing route altitude: a multi-model estimate of aircraft NOx emission impact on O3 photochemistry, Atmos. Env., 95, pp. 468 – 479, https://doi.org/10.1016/j.atmosenv.2014.06.049, 2014.

1375

Stengel, M., Sus, O., Stapelberg, S., Finkensieper, S., Würzler, B., Philipp, D., Hollmann, R. and Poulsen, C.: ESA Cloud Climate Change Initiative (ESA Cloud_cci) data: Cloud_cci AVHRR-AM L3C/L3U CLD_PRODUCTS v3.0, https://doi.org/10.5676/DWD/ESA_Cloud_cci/AVHRR-AM/V003, 2019.

Stengel, M., Stapelberg, S., Sus, O., Finkensieper, S., Würzler, B., Philipp, D., Hollmann, R., Poulsen, C., Christensen, M., and McGarragh, G.: Cloud_cci Advanced Very High Resolution Radiometer post meridiem (AVHRR-PM) dataset version 3: 35-year climatology of global cloud and radiation properties, Earth Syst. Sci. Data, 12, 41–60, https://doi.org/10.5194/essd-12-41-2020, 2020.

1380

Stevenson, D. S., Doherty, R. M., Sanderson, M. G., Collins, W. J., Johnson, C. E., and Derwent, R. G.: Radiative forcing from aircraft NOx emissions: Mechanisms and seasonal dependence, J. Geophys. Res., 109, D17307, https://doi.org/10.1029/2004JD004759, 2004.

1385

Sun, H., Bourguet, S., Eastham, S., and Keith, D.: Optimizing Injection Locations Relaxes Altitude-Lifetime Trade-Off for Stratospheric Aerosol Injection, Geophys. Res. Lett., 50, e2023GL105371, https://doi.org/10.1029/2023GL105371, 2023.

Sun, H., Bourguet, S., Luan, L., and Keith, D.: Stratospheric transport and tropospheric sink of solar geoengineering aerosol: a Lagrangian analysis, npj Clim. Atmos. Sci., 71, 1–9, https://doi.org/10.1038/s41612-024-00664-8, 2024.

1390

Teoh, R., Engberg, Z., Schumann, U., Voigt, C., Shapiro, M., Rohs, S., and Stettler, M. E. J.: Global aviation contrail climate effects from 2019 to 2021, Atmos. Chem. Phys., 24, 6071–6093, https://doi.org/10.5194/acp-24-6071-2024, 2024.

Terrenoire, E., Hauglustaine, D. A., Cohen, Y., Cozic, A., Valorso, R., Lefèvre, F., and Matthes, S.: Impact of present and future aircraft NOx and aerosol emissions on atmospheric composition and associated direct radiative forcing of climate, Atmos. Chem. Phys., 22, 11987–12023, https://doi.org/10.5194/acp-22-11987-2022, 2022.

1395

Textor, C., Schulz, M., Guibert, S., Kinne, S., Balkanski, Y., Bauer, S., Berntsen, T., Berglen, T., Boucher, O., Chin, M., Dentener, F., Diehl, T., Easter, R., Feichter, H., Fillmore, D., Ghan, S., Ginoux, P., Gong, S., Grini, A., Hendricks, J., Horowitz, L., Huang, P., Isaksen, I., Iversen, I., Kloster, S., Koch, D., Kirkevåg, A., Kristjansson, J. E., Krol, M., Lauer, A., Lamarque, J. F., Liu, X., Montanaro, V., Myhre, G., Penner, J., Pitari, G., Reddy, S., Seland, Ø., Stier, P.,

1400

Takemura, T., and Tie, X.: Analysis and quantification of the diversities of aerosol life cycles within AeroCom, Atmos. Chem. Phys., 6, 1777–1813, https://doi.org/10.5194/acp-6-1777-2006, 2006.

The MESSy Consortium. The Modular Earth Submodel System. Zenodo. https://doi.org/10.5281/zenodo.8360186, 2025a, last access: September 2025.

The MESSy Consortium. The Modular Earth Submodel System (2.55.2_no-branch_7639642e_airtrac-SO4). Zenodo. https://doi.org/10.5281/zenodo.15965933, 2025b, last access: September 2025.

Thor, R. N., Mertens, M., Matthes, S., Righi, M., Hendricks, J., Brinkop, S., Graf, P., Grewe, V., Jöckel, P., and Smith, S.: An inconsistency in aviation emissions between CMIP5 and CMIP6 and the implications for short-lived species and their radiative forcing, Geosci. Model Dev., 16, 1459–1466, https://doi.org/10.5194/gmd-16-1459-2023, 2023.

Tiwari, S., Pekris, M.J. and Doherty, J.J.: A review of liquid hydrogen aircraft and propulsion technologies, International Journal of Hydrogen Energy, 57, pp. 1174 – 1196, https://doi.org/10.1016/j.ijhydene.2023.12.263, 2024.

Toohey, M., Jia, Y., Khanal, S., and Tegtmeier, S.: Stratospheric residence time and the lifetime of volcanic stratospheric aerosols, Atmos. Chem. Phys., 25, 3821–3839, https://doi.org/10.5194/acp-25-3821-2025, 2025.

Tost, H., Jöckel, P., Kerkweg, A., Sander, R., and Lelieveld, J.: Technical note: A new comprehensive SCAVenging submodel for global atmospheric chemistry modelling, Atmos. Chem. Phys., 6, 565–574, https://doi.org/10.5194/acp-6-565-2006, 2006.

Tost, H., Jöckel, P., and Lelieveld, J.: Lightning and convection parameterisations – uncertainties in global modelling, Atmos. Chem. Phys., 7, 4553–4568, https://doi.org/10.5194/acp-7-4553-2007, 2007.

Tost, H.: CVTRANS, Johannes Gutenberg University of Mainz, Germany, available at: https://envmodel.ipa.uni-mainz.de/submodels-cvtrans (last access on 21 June 2024), 2019.

Twomey, S.: The influence of pollution on the shortwave albedo of clouds, J. Atmos. Sci., 34, 1149–1152, https://doi.org/10.1175/1520-0469(1977)034<1149:TIOPOT>2.0.CO;2, 1977.

Ueda, S., Miura, K., Kawata, R., Furutani, H., Uematsu, M., Omori, Y. and Tanimoto, H.: Number-size distribution of aerosol particles and new particle formation events in tropical and subtropical Pacific Oceans, Atmospheric Environment, 142, pp. 324 – 339, https://doi.org/10.1016/j.atmosenv.2016.07.055, 2016.

Vehkamäki, H., Kulmala, M., Napari, I., Lehtinen, K. E. J., Timmreck, C., Noppel, M., and Laaksonen, A.: An improved parameterization for sulfuric acid-water nucleation rates for tropospheric and stratospheric conditions, J. Geophys. Res., 107, 4622–4631, doi:10.1029/2002JD002184, 2002.

Von Glasow, R., Bobrowski, N. and Kern, C.: The effects of volcanic eruptions on atmospheric chemistry, Chem. Geol., 263, 131 – 142, https://doi.org/10.1016/j.chemgeo.2008.08.020, 2009.

Wagstrom, K.M., Pandis, S.N., Yarwood, G., Wilson, G. M. and Morris, R. E.: Development and application of a computationally efficient paticulate matter apportionment algorithm in a three-dimensional chemical transport model, Atmos. Environ., 42, 22, pp. 5650 – 5659, https://doi.org/10.1016/j.atmosenv.2008.03.012, 2008.

Wang, Z. S., Chien, C.-J., and Tonnesen, G. S.: Development of a tagged species source apportionment algorithm to characterize three-dimensional transport and transformation of precursors and secondary pollutants, J. Geophys. Res., 114, D21206, https://doi.org/10.1029/2008JD010846, 2009.

Weingartner, E., Burtscher, H. and Baltensperger, H.: Hygroscopic properties of carbon and diesel soot particles, Atmos. Env., 31, pp. 2311 – 2327, https://doi.org/10.1016/S1352-2310(97)00023-X, 1997.

Weinzierl, B., Ansmann, A., Prospero, J., Althausen, D., Benker, N., Chouza, F., Dollner, M., Farrell, D., Fomba, W., Freudenthaler, V., Gasteiger, J., Groß, S., Haarig, M., Heinold, B., Kandler, K., Kristensen, T., Mayol-Bracero, O., Müller, T., Reitebuch, O., Sauer, D., Schäfler, A., Schepanski, K., Spanu, A., Tegen, I., Toledano, C., and Walser, A.: The Saharan Aerosol Long-range Transport and Aerosol-Cloud Interaction Experiment (SALTRACE): overview and selected highlights, B. Am. Meteorol. Soc., 98, 1427–1451, https://doi.org/10.1175/BAMS-D-15-00142.1, 2017.

Whitby, E. R., McMurray, P., Shankar, U., and Binkowski, F.: Modal Aerosol Dynamics Modeling, Tech. Rep. 600/3-91/020, Atmospheric Research and Exposure Assess. Lab., US Environmental Protection Agency, Research Triangle Park, available as NTIS PB91-161729/AS, 1991.

Whitby, E. R. and McMurry, P.: Modal aerosol dynamics modeling, Aerosol Sci. Technol., 27, 673–688, https://doi.org/10.1080/02786829708965504, 1997.

Wu, J.B., Wang, Z., Wang, Q., Li, J., Xu, J., Chen, H., Ge, B., Zhou, G. and Chang, L.: Development of an on-line source-tagged model for sulfate, nitrate and ammonium: a modelling study for highly polluted periods in Shanghai, China, Environmental Pollution, 221, pp. 168 – 179, https://doi.org/10.1016/j.envpol.2016.11.061, 2017.

Yang, Y., Wang, H., Smith, S. J., Easter, R., Ma, P.-L., Qian, Y., Yu, H., Li, C., and Rasch, P. J.: Global source attribution of sulfate concentration and direct and indirect radiative forcing, Atmos. Chem. Phys., 17, 8903–8922, https://doi.org/10.5194/acp-17-8903-2017, 2017.

Zhu, Y., Bardeen, C. G., Tilmes, S., Mills, M. J., Wang, X., Harvey, V. L., Taha, G., Kinnison, D., Portmann, R. W., Yu, P., Rosenlof, K. H., Avery, M., Kloss, C., Li, C., Glanville, A. S., Millán, L., Deshler, T., Krotkov, N., and Toon, O. B.: Perturbations in stratospheric aerosol evolution due to the water-rich plume of the 2022 Hunga-Tonga eruption, Commun. Earth Environ., 3, 248, https://doi.org/10.1038/s43247-022-00580-w, 2022.

1440

1445

1450

1455